Dissertations, Theses, and Masters Projects   Theses, Dissertations, & Master Projects

2019

Interfacial Forces of 2D Materials at the Oil–Water Interface

William Winsor Dickinson

William & Mary - Arts & Sciences, william.dickinson@gmail.com

Follow this and additional works at: https://scholarworks.wm.edu/etd

Part of the Physics Commons

Interfacial Forces of 2D Materials at the Oil–Water Interface

William Winsor Dickinson

Fredericksburg, Virginia

Master of Science, College of William & Mary, 2012
Bachelor of Science, University of Mary Washington, 2008

A Dissertation presented to the Graduate Faculty of
The College of William & Mary in Candidacy for the Degree of
Doctor of Philosophy

Department of Physics

College of William & Mary
May 2019

APPROVAL PAGE

This Dissertation is submitted in partial fulfillment of
the requirements for the degree of

Doctor of Philosophy

_____
William Winsor Dickinson

Approved by the Committee April 2019

_____
Committee Chair
Associate Professor Hannes Schniepp, Applied Science
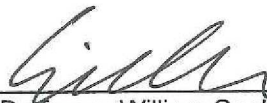College of William & Mary

_____
Committee Co-Chair
Associate Professor Mumtaz Qazilbash, Physics
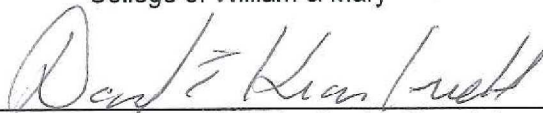College of William & Mary

_____
Professor Irina Novikova, Physics
College of William & Mary

_____
Professor William Cooke, Physics
College of William & Mary

_____
Professor Emeritus David Kranbuehl, Chemistry
College of William & Mary

ABSTRACT

Two-dimensional (2D) materials, including graphene and graphene oxide (GO), are a subject of interest for many researchers due to their exceptional properties (strength, conductivity, etc.). These materials, comprised of atomically-thin sheets, may naturally occur stacked together like sheets of paper, but their most interesting properties emerge when separated into individual layers. However, scaling up the processes used to isolate single sheets of some of these materials, particularly graphene, has proven problematic. They can be fiercely resistant to exfoliation, difficult to disperse, and have a worrying propensity to restack. All these problems contribute to the great difficulty these fascinating materials have encountered leaving the lab and entering commercial use. Existing production methods either produce minute quantities, require huge amounts of energy, or involve chemical treatments that transform their properties, typically for the worse. Here, we investigate a method that instead harnesses these difficulties. We force the material to exfoliate itself at the interface between two immiscible solvents, stabilizing the interface and acting as a surfactant with a two-dimensional morphology.

In this work we investigate this method and its results in two ways. First, we describe a method we developed using optical microscopy and free software (ImageJ and Gwyddion) that rapidly and inexpensively provides full, simultaneous characterization of thousands of sheets of these materials, yielding both flake area and thickness. We then use this technique to examine the changes induced in 2D material that was exfoliated at the oil–water interface, improving our understanding of the process at the population/production level. Second, we characterize this interaction using force spectroscopy with graphene-functionalized colloidal probes at the surface of pinned droplets of heptane in water. This provides valuable insight into the not-well-understood mechanisms underlying the exfoliation process at the interfacial level. By combining the results seen across these two length scales, our results significantly enhance the understanding of this novel exfoliation process.

Additionally, we examine the interactions between another 2D material, mica, and an oil-coated probe in a salt brine using force spectroscopy at high temperature (100 °C) and high pressure (100 atm). These tests are the first demonstration of force spectroscopy in this parameter space and reveal the significant impact of both temperature and pressure on interfacial forces between oil and mineral in this regime.

Taken together, our results impact a wide variety of systems including the large-scale production of nanomaterials, nanocomposites, solar cells, sensors, flexible electronics, oil recovery, and catalysis.

TABLE OF CONTENTS

ACKNOWLEDGEMENTS

This work could not have occurred without significant support and assistance from my fellow members of the Nanomaterials & Imaging lab: Laura Dickinson, Sean Koebley, John Gardner, Scot Peeke, Qijue Wang, Mahmoud Amin, Samantha Applin, Avishi Abeywickrama, and Dinidu Perera. Furthermore, I would like to thank Paula Perry, Ellie Wilkinson, Carol Hankins, Lydia Whitaker, and Lianne Ashburne for their extensive support.

On a more personal note, I would also like to salute the members of CASK for their camaraderie and good cheer, which was often sorely needed during this process. Charlie Fancher has also been an invaluable source of support, both in the gym and outside it.

Finally, I would like to reiterate my thanks to Laura Dickinson, my wife and collaborator, without whom none of this would have been possible.

For my wife, my son, and my parents.

LIST OF TABLES

LIST OF FIGURES

Chapter 1

Introduction and Theory

1.1. Introduction and Structure

The class of 2D materials includes the strongest material ever tested (graphene) and materials with a variety of unusual optical, electrical, and magnetic properties.[1-3] These properties result from their unusual form factor; they are comprised solely of a single to few layer sheet of atoms, with no additional "bulk" material. The limitation of their shapes to two dimensions constrains the movement of phonons and electrons transmitted through them to only two dimensions, rather than the usual three, constricting the dissipation of energy. However, while these properties (and their myriad potential uses) are certainly appealing, the materials themselves are not well utilized in industry or commercial applications. This is due to the extreme difficulty in maintaining the form factor the properties originate from, i.e. single, atomically thin sheets. The materials typically originate as large stacks of sheets held together by van der Waals forces. Therefore, before the material can be utilized, the sheets must be separated into individual or few layer stacks. This can be difficult, as some of the most

interesting members of this class of materials, including graphene, do not suspend well in any solvents and the layers are difficult to separate (or "exfoliate") from the stacked natural material without restacking. The most common methods for separating these layers have involved forcibly breaking the materials apart through techniques such as sonication, which uses high-energy sound waves. Sometimes the resulting suspension is stabilized with the introduction of a surfactant, which coats the sheets and keeps them from re-aggregating. Both of these methods are costly and detrimental to the properties of the material as the final result is either coated with another lesser material that then must be removed (surfactants) or has been broken into smaller pieces which have diminished properties[4–9] at high energy cost (sonication). However, a recently developed technique for separating the layers instead makes use of these materials' difficulties in exfoliation and suspension. This method first combines two immiscible solvents, neither of which the 2D material will readily suspend in. Next, it introduces the bulk form of the material to this combination. Here, surprisingly, the material will exfoliate itself to best cover the most energetically-efficient location available – the interface between the liquids. This creates an emulsion of the two solvents stabilized by the 2D material.[10]

In this work, we describe two techniques we developed to investigate the underlying mechanisms of this method. First, we detail a new, rapid method for optical characterization of nanosheet materials. Our technique relies only on optical microscopy and free, open-source software, but is still powerful enough to simultaneously determine the thickness and lateral dimensions of thousands of individual nanosheets in images on the scale of one square millimeter. We then examine the macroscopic results of the emulsion-based exfoliation process, revealing new insights into the behavior of entire populations of nanosheets at the oil–water

interface. Second, we directly probe the interfacial forces of the 2D material at the interface between these two liquids using atomic force spectroscopy. This entails measuring the interactions between a colloidal atomic force microscope (AFM) probe that has been functionalized with a 2D material and the surface of a bubble of heptane pinned to a substrate in a water bath. By examining the long-range attraction and adhesion seen between these two objects we can begin to expand our understanding of the exfoliation process as it occurs at the interface.

Furthermore, we broaden our investigations of the interactions between 2D materials and oil–water interfaces into more extreme environments. Here, we demonstrate, for the first time, force spectroscopy measurements taken at high temperature (100 °C) and high pressure (100 atm), simulating those conditions found at depth in an oil reservoir. Using a 2D mica substrate and a crude-oil functionalized colloidal AFM probe, we measure the adhesion between the two as a function of temperature and pressure while immersed in a salt brine. This expands the reach of atomic force spectroscopy into a new regime and reveals the impact of these variables on surface interactions.

This dissertation is broken into six chapters. The first chapter gives an introduction and the general motivation for the work. It then provides an overview of three major topics that pertain to all aspects of this research: surface energy and interfaces, 2D materials and their structure, and the basic mechanisms underlying force spectroscopy. The second chapter describes the experimental methods utilized. The third chapter focuses on the optical analysis technique we developed, providing the underlying theory, its development, and the results when applied to the emulsion-based exfoliation process. The fourth chapter focuses on the interaction of a probe functionalized with 2D material and a liquid–liquid interface. It includes an overview of the theory of particle–interface

interactions and the complications inherent in performing force spectroscopy on a non-rigid surface. The fifth chapter examines the interactions between a crude oil functionalized probe and an atomically flat mineral substrate at high temperatures and pressures. This chapter includes a brief discussion of the formation and development of petroleum reservoirs and the methods used to predict the efficacy of various extraction methods. The sixth chapter provides a conclusion and avenues for future work.

1.2. Surface Energy and Interfaces

Surface energy arises from the differences between the possible arrangements of atoms at the surface of a material and those arrangements possible in the bulk portion of the material. Atoms at a surface have an inherent inefficiency in their arrangement, as they are not able to fully bond with other atoms in the material due to their exposed face. As it is necessary for any object to have some sort of surface, and there is always some amount of energetic cost associated with a unit of surface area, systems attempt to configure themselves in such a way as to minimize this energy. This is what drives liquids to form into spherical droplets, as this is the shape with the lowest surface–volume ratio and thus the lowest amount of energetically inefficient surface atoms. While this idea is most familiar when associated with liquids, where it is commonly called surface tension, the same concept still applies to the structure and properties at any boundary between two substances, regardless of phase. We also note that the cost associated with the surface is not only dependent on environmental factors, such as temperature and pressure, but also intrinsically dependent on the substance on the other side of the interface, as the interactions between the two materials will determine the possible atomic/molecular arrangements. It is therefore not a singular property for any given material, but instead varies across each possible combination of material

and circumstance. For this reason, surface energy is also called interfacial energy and is important for wetting and other interfacial processes as it also determines any movement of material on or about the surface.

We can also think of this energy as the work required to deform a surface and thereby create additional surface area. More explicitly, we can define the interfacial energy in terms of the work required to split a surface by breaking the bonds in the bulk portion of the material. For the interface between two materials A and B, the interfacial energy γ_{AB} is defined by convention as being half the work required to split a unit area of that material. That is,

$$\gamma_{AB} = \frac{1}{2} \Delta W_{AB} \qquad (1.1)$$

where the factor of two comes from the fact that two unit areas of the interface are being created from this splitting.

A multitude of models exist for describing the surface energy of a system. They vary in the number of components the quantity is broken into, typically one to three. The best-known single component model was described by Zisman in 1964.[11] This model relies on the measurement of contact angles (see Figure 1.1) between a surface and droplets of various liquids with known surface tensions. The surface energy of the solid surface is deemed to be equal to the surface tension of the highest surface tension liquid that would perfectly wet the surface, as determined by plotting the contact angles of the various liquids against their surface tensions and finding the intercept. This method works well for non-polar polymer surfaces, such as polyethylene, but begins to show weakness when used to describe surfaces that are, even in part, polar, i.e. have a net dipole moment. This is due to its reliance on a single parameter of the

liquids—the surface tension—which cannot describe the entirety of their interactions with all kinds of surfaces.

Another group of models were developed, this time with two components. These components are typically broken into dispersive (or non-polar) and polar. While the dispersive forces are typically stronger, the polar interactions still play a significant, and sometimes dominant, role. Several models exist that incorporate these two components, including those developed by Owens and Wendt,[12] Fowkes,[13] Wu,[14] and Schultz.[15] Experimentally, each of these methods still rely on contact angle measurements as seen in the Zisman theory. The first three differ chiefly in the liquids used and the use of the geometric mean, harmonic mean, or both for combining the results of these different liquids. The last (Schultz) uses a two-liquid system where contact angles of a droplet submerged in another liquid are used to examine particularly high-energy surfaces that otherwise are completely wet by most liquids.

Several theories also exist which describe surface energy with three (or more) components, including an extended version of the above Fowkes theory and the van Oss theory.[16,17] By using n different liquids with the Fowkes method, rather than two, it is possible to determine the contribution of n components of the surface energy, including dispersion and polar interactions, but also hydrogen bonding, Debye (induction) forces, etc. The description developed by van Oss and co-workers splits the polar component into contributions from acids and bases. Despite the varied nature of these theories, ultimately each must be measured by one of the following methods.
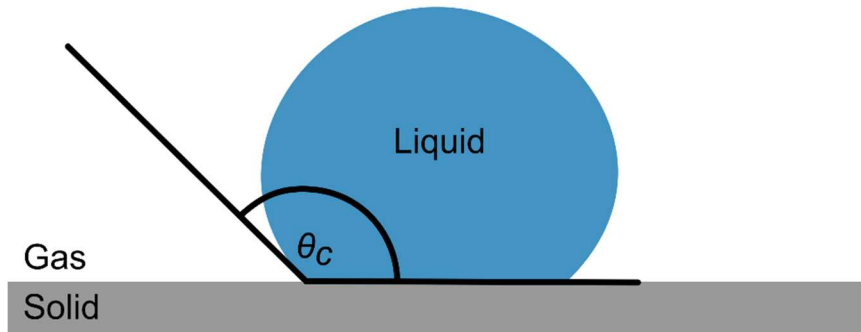
Figure 1.1: Diagram of the essential relations in contact angle measurements. The contact angle θ_c is defined as the angle between the surface of the solid (gray) and the tangent line of the edge of the liquid droplet (blue) where it contacts the solid surface. The contact angle shown here is approximately 135°.

There are several common methods for measuring surface energy. Contact angle measurements are among the most common This type of measurement formed the initial basis for all the above theories of surface energy, though they can be now measured using other techniques as well. This type of measurement involves placing a droplet of a liquid onto a flat surface of a given material and measuring the angle that the liquid forms at the edge of the droplet (Figure 1.1). This can be done using a goniometer, protractor, or, more commonly in this age, a camera and computer software. This angle can be related to the surface energies of the three components of the system by the Young equation:

$$\gamma_{SG} = \gamma_{SL} + \gamma_{LG} cos(\theta_c), \qquad\qquad (1.2)$$

Where γ_{SG} is the energy of the solid–gas interface, γ_{SL} that of the solid–liquid interface, γ_{LG} that of the liquid–gas interface, and θ_c the angle formed at the intersection of the three components. This relationship would also hold if the gas component was instead another, immiscible liquid. These angles are used to generally place various liquid/solid/gas systems along a continuum based on the degree of "wetting," or

covering, of the solid surface by the liquid (Table 1.1). Visual representations of each of these categories can be found in Figure 1.2.

	Contact Angle	Degree of wetting
A	$\Theta = 180°$	Perfectly non-wetting
B	$90° < \Theta < 180°$	Low wetting
C	$0° < \Theta \leq 90°$	High wetting
D	$\Theta = 0°$	Perfectly wetting

Table 1.1: Contact angle values and descriptions for different ideal cases and ranges of wetting behavior. Each case (A through D) is represented graphically in Figure 1.2.
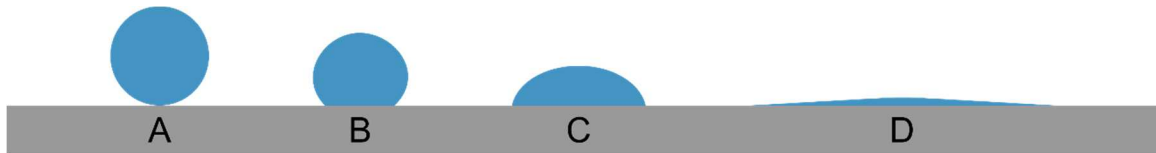
Figure 1.2: Various shapes assumed by liquid droplets with differing degrees of surface wetting: perfectly non-wetting (A), low wetting (B), high wetting (C), perfectly wetting (D).

While this angle is relatively straightforward to measure and categorize, it is easily affected by surface contaminants or structural issues with the material as the relationships above assume a completely flat and rigid surface, which is usually not possible. The best available case is a single, perfectly clean, single species, atomically flat layer that is large enough on which to place a visible droplet, such as an exceptionally well-cleaved piece of highly oriented pyrolytic graphite (HOPG). These restrictions clearly limit the possible substrates and, therefore, combinations of materials available, if one does not wish to compromise their measurements with such factors.

(A)
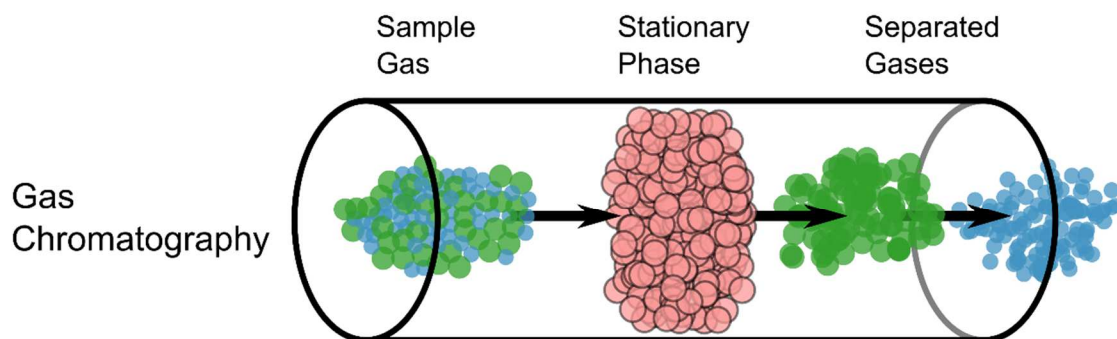
(B)
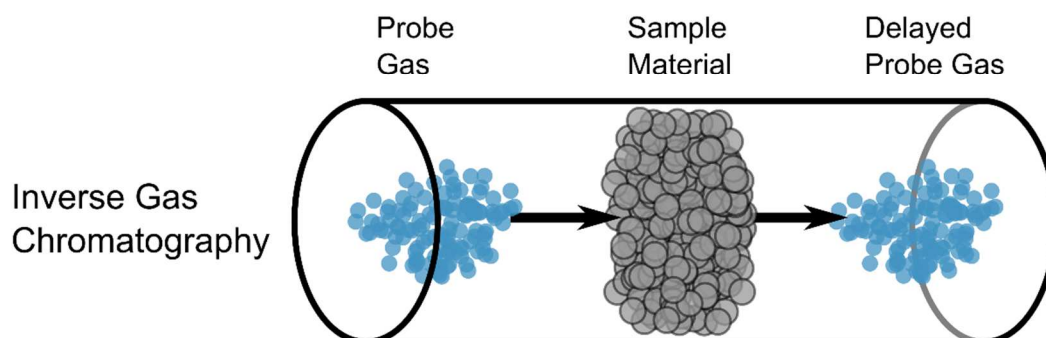
Figure 1.3: Diagram of gas chromatography (A) and inverse gas chromatography (B). Gas chromatography can separate components of a sample gas by flowing it through a tube which is packed with a known material, referred to as the stationary phase, to which the components of the sample gas adsorb and then elate at timings individual to each component. Inverse gas chromatography instead measures the surface energy of a material by monitoring the lag and flow rate of a probe gas as it travels through a column in which the sample material has been placed. Varying the probe molecule or other, environmental variables allow for information about the sample to be determined based on these lag and flow times.

Another method for measuring surface energy is inverse gas chromatography (IGC).[18–21] Typically gas chromatography is used to separate components of a liquid or gas sample by flowing it through a column containing a known material referred to as the stationary phase. The different components of the sample adsorb onto the surface of the stationary phase and then, after some characteristic retention time, each

component elutes from the surface, separating them. Inverse gas chromatography reverses this by instead using the sample material as the stationary phase and flowing only a single known probe molecule through the column. By examining the elution time and flow rate as a function of different variables such as the choice of probe molecule, temperature, pressure, or sample packing it is possible to determine many characteristics of the sample/probe molecule interaction. While powerful, the technique is also very sensitive to the amount of material used and its packing in the column, especially for low-energy or low surface area materials, and can require extensive computational support to account for these variables.[22]
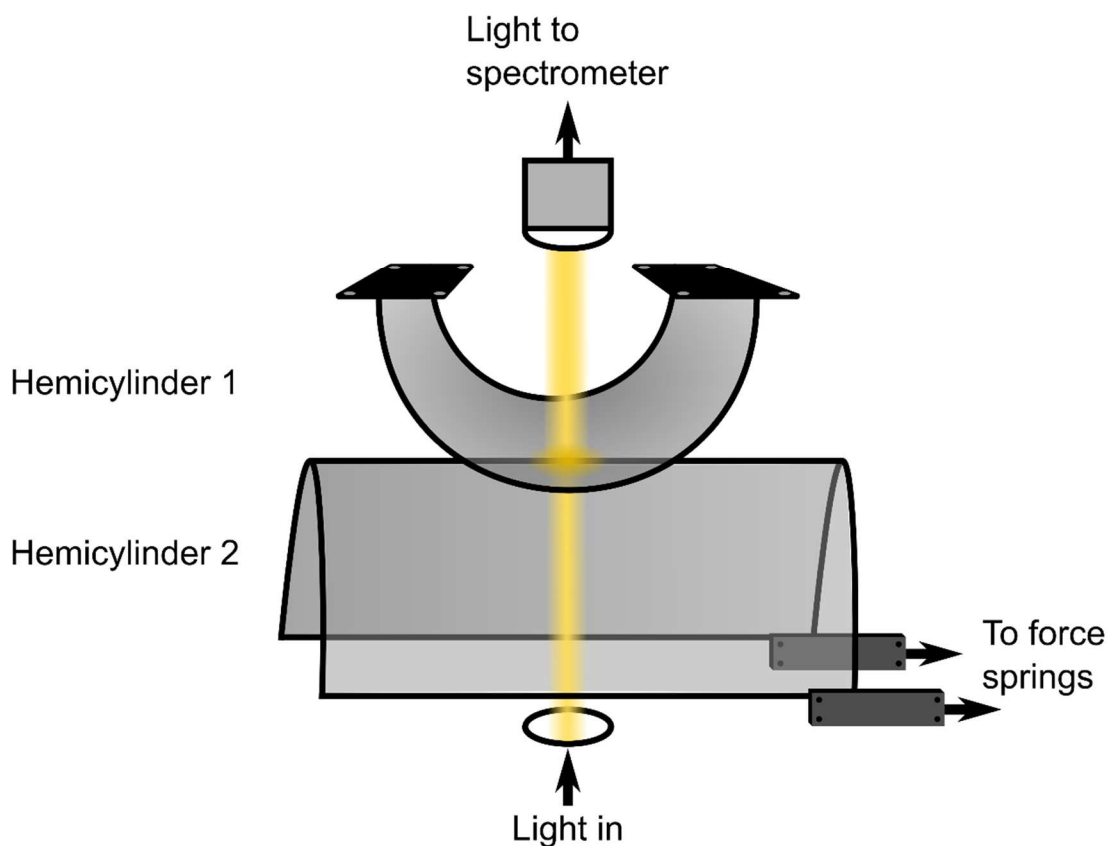
Figure 1.4: The surface force apparatus (SFA) measures interaction forces between two optically transparent hemicylindrical structures through the use of a spring-loaded cantilever with separation distance determined through multiple beam interferometry.

The surface force apparatus (SFA) is another instrument capable of measuring surface forces and energy. It is capable of measuring forces between two surfaces in either gas or liquid environments and is capable of measuring forces as small as a few nN with distance resolution on the angstrom scale. The development of the apparatus has been primarily driven by the work of Israelachvili and coworkers, with the Mark I version first described in 1976[23] and the most recent iteration, the SFA 2000, described in 2010.[24] The initial Mark I built on an earlier version of a similar apparatus by Tabor and Winterton, which was limited to working in air.[25] The general structure consists of two hemicylinder surfaces, one mounted stably, and the other attached to a spring-loaded cantilever (Figure 1.4). The hemicylinders are either coated with or comprised of the material to be characterized. Mica is often used as the primary component of the hemicylinder, as it is molecularly flat, optically transparent (a requirement for the device), and easy to work with. It is usually backed with a thin layer of silver to enhance reflectivity. The surfaces of the hemicylinders are initially oriented with their cylindrical axes at right angles to each other and are slowly brought into contact using a multi-stage approach setup. The separation between the surfaces is measured via multiple beam interferometry and the force applied to the lower hemicylinder is measured via a series of springs. This technique is limited to materials or thin coatings that are optically transparent due to the use of interferometry and is oriented towards the use of flat surfaces rather than other objects, though extensions and variations are available. As a consequence of the two-hemicylinder geometry it has a minimal contact area of 5 μm^2.[26] Additionally, as it relies on a mechanical screw system to move the surfaces and identification of interference patterns to determine separation distance, it has a time resolution of approximately 1 second.[27] The SFA is only available commercially from SurForce LLC, which was founded by Israelachvili in 2002.[28]
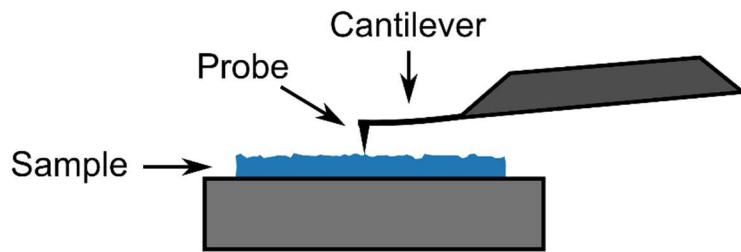
Figure 1.5: Atomic force microscopy (AFM) utilizes a probe (nanometer to micron tip radius) to obtain topography images of a sample surface by rastering back and forth. The probe is attached to a flexible cantilever (hundreds of microns in length) which deflects as a function of topography and/or surface interactions. This provides a mechanism to visualize surface features too small to be resolved with traditional optical microscopy methods or even those that do not have a "visible" component in any sense (surface forces).

Atomic force microscopy (AFM) can also be used to measure surface energy. It uses a micro or nanoscale probe attached to a microscopic cantilever that is brought into contact with the surface of a sample (Figure 1.5). The force between the probe and sample is measured by recording the bending of the cantilever attached to the probe. It has sub-nanometer distance resolution and piconewton force resolution. The interaction forces measured can include mechanical contact, electrostatic, or magnetic forces, among many others. This information can be used to generate images of sample surfaces or maps of interactions as a function of z-spacing between probe and sample. This technique was the primary one used in this work and the use of this instrument to measure surfaces forces and interactions as a function of separation distance, called force spectroscopy, will be discussed in-depth in section 4 of this chapter and is the main focus of chapters 2, 4, and 5.

1.3. 2D Materials

1.3.1. Structure of 2D Materials

Two dimensional materials are defined by their shape rather than by a particular chemical composition. They are composed of a sheet only a single or few atoms thick. This unusual structure constrains the motion of waves and particles in the material to only this plane rather than the three-dimensional (3D) structure of other materials. By reducing the possible directions for movement, a variety of interesting properties emerge in these materials. While at least 826 candidates for stable 2D materials have been identified,[29] attention has largely focused on a small subset of these, described below. Our work focused on the first two, graphene and graphene oxide, but the techniques we developed can be applied to the others as well.
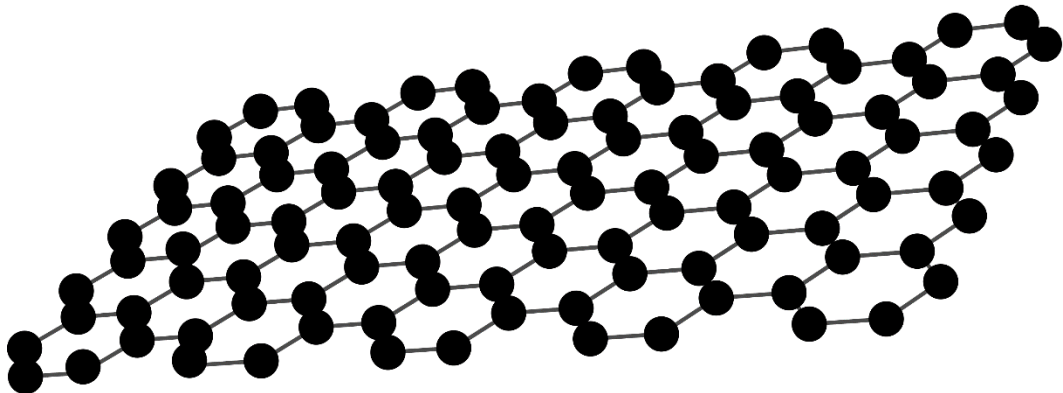
Figure 1.6: Graphene exhibits an unusual atomic structure; the hexagonal latttice of carbon atoms (black circles) makes individual, atomically-thin sheets of material. These sheets stack together like sheets of paper to form the more common graphite.

The first free-standing atomically-thin material of this type, graphene, was isolated in 2004 by Geim and Novoselov.[30] They received the Nobel Prize in Physics in 2010 for this groundbreaking discovery. Graphene is the most well known and most well studied

2D material. It is composed solely of a hexagonal lattice of carbon atoms (Figure 1.6).

Graphene is the strongest material ever tested[31] and has a bevy of other interesting

mechanical properties.[32] It is also an excellent conductor of heat[33,34], and has a zero

bandgap with extremely high electron mobility.[35] The optical properties are also

promising; despite being only one atom thick it is visible to the naked eye, absorbing

2.3% of visible light.[36]
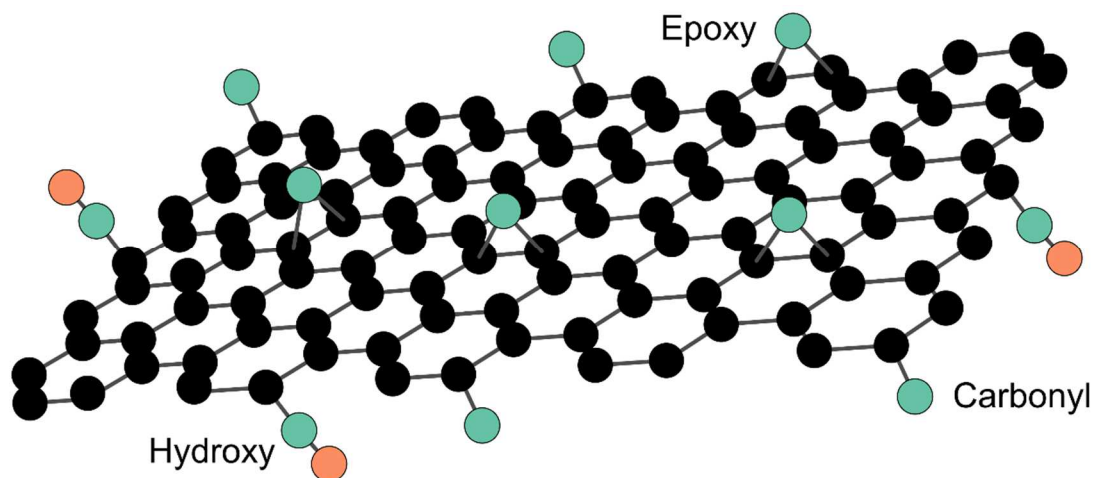
Figure 1.7: Graphene oxide is composed of a hexagonal lattice of carbon atoms (black) functionalized with oxygen (blue) and hydrogen (orange) atoms in various groups. Shown are: epoxy groups, oxygen atoms that bridge two carbons; carbonyl groups, oxygen atoms double-bonded to a single carbon atom; and hydroxy groups, an oxygen and hydrogen group bound to a single carbon. Other, more complex functional groups are also possible.

Graphene oxide (GO) is composed of a single sheet of carbon atoms laid out in a

hexagonal lattice, like graphene, but is additionally functionalized on the surface and

edges with oxide groups (epoxy, carbonyl, hydroxy, phenol).[37,38] It was first reported

in 1859 by Brodie,[39] but the most common method for bulk synthesis at this time is

based on the 1958 work of Hummers.[40] GO disperses well in water (in stark contrast

to graphene) and is easier to work with as a result. One application for the material is

to eliminate the functional groups from its surface to recover graphene. Other

promising applications for GO include water filtration,[41] impermeable coatings,[42] and flat lenses.[43]
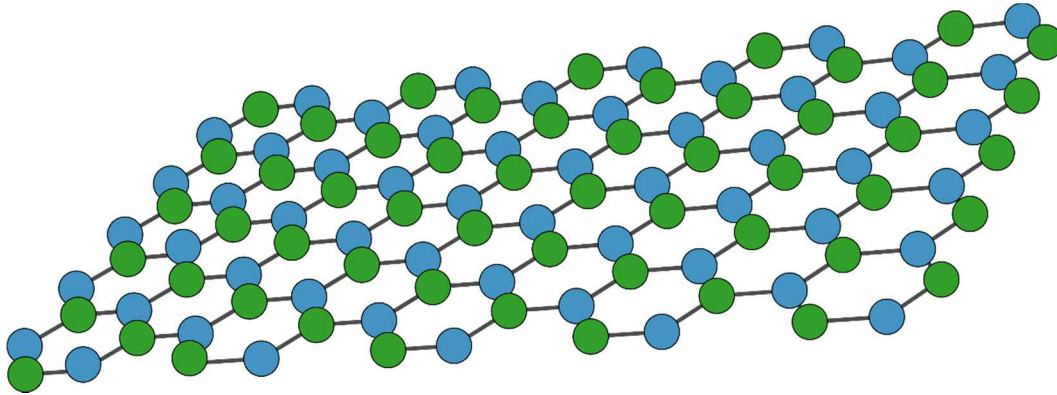
Figure 1.8: Hexagonal boron nitride (hBN) is composed of boron (blue) and nitrogen (green) atoms arranged in a hexagonal structure. Just like graphene, this hexagonal lattice structure forms individual sheets of material that can be stacked in layers.

Hexagonal boron nitride (hBN) shares its hexagonal lattice shape with graphene but replaces the carbon atoms with alternating boron and nitrogen (Figure 1.8). It is far more thermally stable than graphene, being capable of withstanding sustained exposure to 850 °C temperatures, an excellent conductor of heat,[44] and is an insulator with a 5.955 eV bandgap.[45] Due to these properties, applications for its use include roles in 2D electronics, especially when combined with other 2D materials,[46,47] ultraviolet lasing,[48] and as nanofillers in polymers.[49]
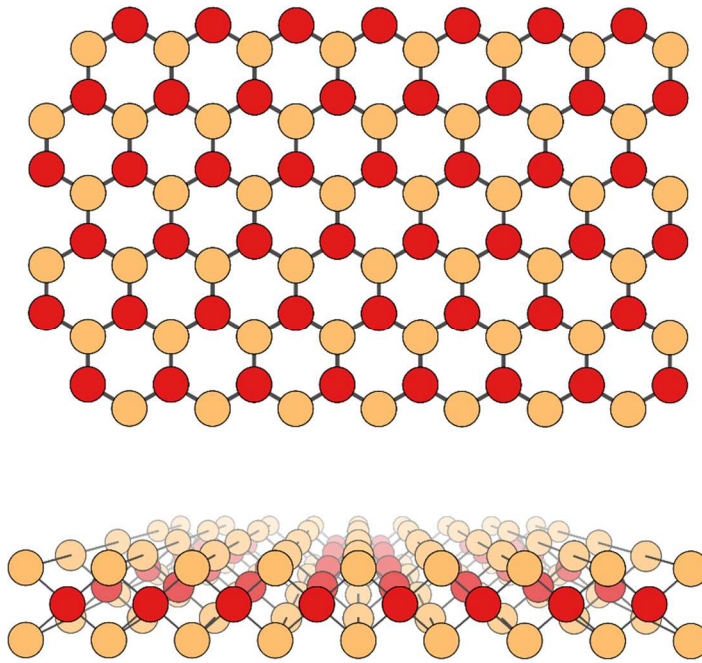
Figure 1.9: Transition metal dichalcogenides (TMDs) also exhibit a hexagonal lattice arrangement when viewed from above (like graphene and hexagonal boron nitride). However, viewing a cross section of this material illustrates that the structure is composed of a layer of transition metal atoms (red) between layers of chalcogen (yellow). Therefore, in contrast to graphene and hexagonal boron nitride, a single layer of TMDs is a triple atomic layer of atoms. Some variation occurs in the spacing and alignment occurs, depending on the atomic species involved. This is the trigonal prismatic (2H) orientation, seen in MoS_2, among others.

Transition metal dichalcogenides (TMDs) are composed of a single atomic layer of a transition metal sandwiched between two atomic layers of a chalcogen (Figure 1.9). Some variation occurs in the spacing and alignment occurs depending on the atomic species involved, options include: trigonal prismatic (2H) (as seen in Figure 1.9), distorted octahedral (1T), and dimerized (1T′). They were first described structurally by Dickinson and Pauling in 1923,[50] who determined the crystal structure of MoS_2. TMDs are semiconductors, which distinguishes them from both graphene (zero bandgap) and hBN (high bandgap). An emerging field of interest, TMDs have

demonstrated a variety of intriguing magnetic, electronic, and optical properties, including superconductivity in some cases. [51,52]

Due to their unusual structure, determining and examining the surface energy of 2D materials can present some experimental challenges. For example, many of the properties of the material rely on it being a single layer. Therefore, it is necessary to isolate individual atomic layers for testing. Additionally, it can be difficult to obtain samples with significant lateral size to successfully perform many standard measurement techniques. The same techniques that are typically used for measuring surface energy can also be used with 2D materials. However, some require modification while others become more useful. Contact angle measurements are highly sensitive to surface features in such materials and require significant effort be expended in ensuring the material is present in only a single continuous sheet.[53–55] Any atomic steps which form when multiple layers are present can create pinning effects. Additionally, it can be difficult to create samples with sufficient lateral size as the droplets used in this technique are usually macroscopic to allow for optical determination of the angle. IGC,[53] which relies on packing the material into a column, can also encounter significant difficulties as the orientation of these materials is of extreme importance relative to the flow of the probe molecule despite being difficult to manage and the technique can have difficulties with low surface area samples.[22] The amount of material required for this technique can also be substantial, further complicating this process. The SFA can work well with 2D materials,[56] as their thin nature allows for high degree of optical transparency. However, locating samples of sufficient size and preventing the attachment mechanism used to bind the material to the hemicylinder from contaminating the measurements can be difficult. AFM is well suited to dealing with samples of this size due to the extremely small nature of the

probes used, though the experimental setup can be complicated and may require specialized probes or apparatus.[57,58]

1.3.2. Production of 2D Materials

Despite the bevy of intriguing properties displayed by these materials, their level of use in commercial and industrial applications is relatively low. This is mainly due to the difficulty inherent in producing material at large enough scale at a reasonable cost. As the material needs to be in, ideally, single layer form, any production methods must select for this form factor over any stacked variation, while generating large volumes at low cost. Further, larger scale sheets have improved qualities when compared to smaller ones,[4–9] providing another constraint on production.

There are a number of production methods that have been used for production of 2D materials. We will cover the most common of these here, focusing on the production of graphene. The first paper by Geim and Novosolev demonstrating free standing graphene used exfoliation via adhesive tape to produce the material.[30] This process involves attaching a piece of self-adhering tape to a graphite surface and removing it, bringing with it a thin layer of graphite. By repeating this process with the removed graphite, it is possible to obtain ever thinner layer, eventually resulting in some single layer material. While an excellent proof of concept, the technique is labor intensive and not suitable for producing consistent single layer material, especially not in large quantities, though recent developments can be more consistent, at the expense of additional processing time.[59] Another process involves immersing graphite in a solvent and applying high energy sound waves to break apart the sheets.[60,61] This can produce single layer material, but thickness can be variable and always produces very small pieces (laterally), which have diminished properties compared to larger sheets. The pieces also have a worrying tendency to restack. It is also possible to introduce a

surfactant which will enable the graphene sheets to readily exfoliate in water by bonding with the surface.[62–65] However, this greatly changes the surface properties of the material and necessitates removing the surfactant which is often not trivial. Sheets can also be grown in single layers through vapor deposition[66] or epitaxial growth.[67] As these processes work exclusively with a single layer at a time, it is not possible to generate large volumes of material which would be required for most industrial applications. Reduction of graphene oxide, i.e. removal of the functional groups, is also possible,[68,69] but carries with it many of the same issues as those found in surfactant-aided exfoliation as well as structural damage to the sheets.

As all of these existing techniques still are not sufficient to produce large quantities of single layer material, it is imperative that other production techniques continue to be researched. One example is an emulsion-based technique first described in 2013[10] by our collaborators at the University of Connecticut. This method makes use of the general reticence of graphene sheets to suspend in a solvent by instead providing them with two different immiscible solvents. As the sheets do not readily suspend in either solvent, it is instead energetically favorable for them to go to the interface between the two liquids. As this interface is inherently 2D, the stacked graphite naturally exfoliates itself in order to more fully cover the available surface area. The material will even stabilize emulsions of these two liquids which is why it has been described as a 2D surfactant. While the evidence for the process is easily visible at the macroscopic level as it can be used to produce single layered material, bubbles, foams, and coatings on surfaces,[70–74] the precise mechanism underlying the process is not entirely understood.

Figure 1.10: Optical image of graphene coated bubbles of water in heptane. Since the heptane and water are immiscible liquids, they remain separated when combined in a single vessel. The interface between the two liquids is the most energetically favorable location for the graphene sheets, which do not readily suspend in either solvent. When graphite is combined with heptane and water in a sealed vial and the vial is shaken, the graphite exfoliates to better cover the interface and graphene coated bubbles result. Bubbles are visible to the eye and are in the millimeter range.

Molecular dynamic simulations have been able to provide some insight into the process, providing computationally-derived potential wells and other information.[10] However, many assumptions are imbedded into these models and they are limited in the number of particles which can be simulated. As such, the importance of direct measurements of the interactions between this material and the liquid–liquid interface cannot be understated. The goal of this work is to provide the beginnings of acquiring

this information, using a functionalized AFM probe to perform force spectroscopy measurements at a liquid–liquid interface.

1.4. Force spectroscopy

While AFM is often considered to be an imaging technique, it is also capable of performing extremely precise measurements of forces and interactions between the probe and a sample. The technique and theory are provided here, while a more detailed exploration of the implementation, data acquisition, and analysis is given in Chapter 2. Due to the small size of the probe in the nanometer to micrometer range, it is possible to precisely locate specific areas of interest on a sample often with nanometer precision. This makes it well adapted for work with extremely small samples, such as 2D materials which are very sensitive to changes in surface topography. In addition, the technique is highly sensitive, able to measure forces in the piconewton range. The probes used also exist in a variety of form factors and can be functionalized with many different materials. One can use either the sharp probes usually used for imaging or larger colloidal probes. The sharp probes can be as small as a few nanometers across and are ideal for taking measurements in highly precise locations or with single molecules. The larger colloidal probes can be many microns across and provide a more well-defined surface geometry. Colloidal probes can also avoid the issues the sharper probes can experience with breaking or chipping/cracking during use. Such effects can significantly affect the interactions between probe and sample, but in a way that may not be readily apparent visually and can carry significant error risk as a result.

The atomic force microscope has a variety of different implementations, but all use a nano- or micro-scale probe attached to a flexible cantilever (typically between 50 to

400 µm in length) to measure surface interactions. This cantilever typically extends from a millimeter-sized chip for ease of use. Both the probe and sample are mounted in the instrument and then brought into near contact via a coarse adjustment mechanism and brought into complete contact using a piezoelectric-based device ("piezo"). This device can be attached to either the probe or the sample depending on the instrument. Both varieties were used in this work. Different methods of detecting cantilever deflection exist,[75,76] however the most typical examples, including the ones used in this work, use a laser beam focused onto the back of the cantilever which often has a reflective coating. The reflected beam is captured on a four-segment photodetector which transmits and magnifies any deflection or torsion of the cantilever. The piezo is used to move the probe toward and away from the sample and the deflection of the cantilever can be correlated with this distance to provide a map of the net attractive and repulsive forces near the surface as well as any interactions while they are in contact.

The primary interactions between the probe and sample in force spectroscopy are either driven by surface charge or by dipole interactions (van der Waals forces). Both are impacted by a variety of factors, including the geometries of the two surfaces involved, the material compositions, and the intervening medium. We will discuss each of them here, providing a general overview of the mechanisms underlying this technique. The system studied in Chapter 5 (oil functionalized probe) of this work utilized a spherical probe and a rigid planar sample, which has been described by multiple sources,[77–79] and will provide a basis for the following overview. The more complicated spherical probe and bubble system studied in Chapter 4 will be discussed in the first section of that chapter.

Surface charge interactions are generally described by classical electromagnetism in this regime. The speeds involved in force spectroscopy are low enough that the electrostatic approximation is sufficient, and the magnetic force can be disregarded. We can then start from Coulomb's Law, which describes the force $\boldsymbol{F}$ exerted on a point charge q_1 by another point charge q_2 in a vacuum:

$$\vec{F}(r) = \frac{1}{4\pi\varepsilon_0}\left(\frac{q_1 q_2}{r_{21}^2}\right)\hat{r}_{21},$$

(1.3)

where ε_0 is the permittivity of free space, q_1 and q_2 are the charges of the two points and $\boldsymbol{r_{21}}$ is the vector between them. The electric field $\boldsymbol{E}$ generated by a set of N such points can then be described by the summation:

$$\vec{E} = \frac{1}{4\pi\varepsilon_0}\sum_{i=1}^{N}\left(\frac{q_i}{r_i^2}\hat{r}_i\right),$$

(1.4)

where q_i is the charge of the ith point and $\boldsymbol{r_i}$ is the distance between the single point and the ith point. For a system with continuous charge, rather than discrete points, we can instead integrate over the entire volume:

$$\vec{E}(r) = \frac{1}{4\pi\varepsilon_0}\int \frac{\rho(r')}{|r-r'|^3}(r-r')\, dV,$$

(1.5)

where ρ is the charge density at a given point in the volume V. There are a number of methods to proceed from this point towards the sphere–plane system seen in force spectroscopy. One example is to assume a pair of perfectly smooth surfaces with evenly distributed charges and model them as a capacitor.[78]
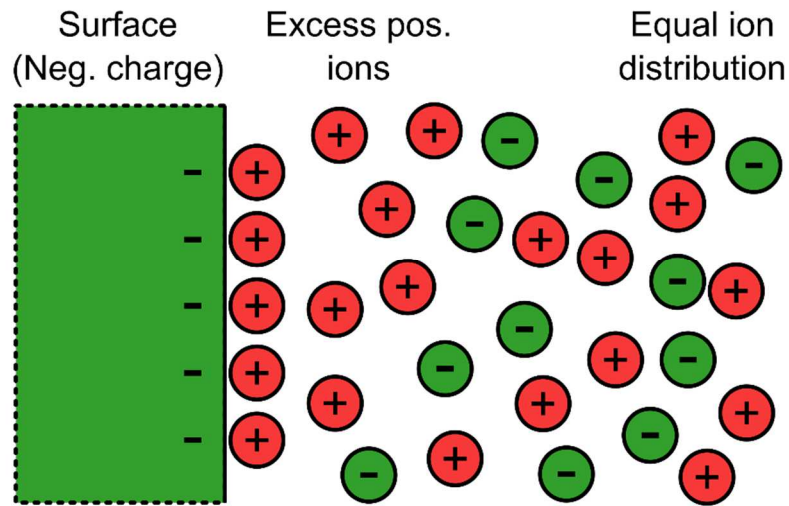
Figure 1.11: Illustration of the double layer formed by ions in solution near a charge surface. The negatively charged surface (green, left) has an adsorbed layer of positively charged ions (red, center) with an excessive concentration of these same positively charged ions nearby which then gradually return to an equal ion distribution at greater separation (right).

However, while the above is sufficient for describing interactions taking place in vacuum or air, the measurements in this work took place in liquid and therefore a description of the effects of this intervening medium is required. As the surfaces described here have some degree of surface charge, typically from a chemical reaction with the liquid medium, dissociation of surface groups into the medium, or adsorption of other molecules from the medium, other molecules in the liquid that exhibit an opposite charge will be attracted to these surfaces. These attracted molecules form a continuously-shifting layer driven by thermal motion. This layer has a gradient concentration, where the highest density lies closest to the charged surface (Figure 1.11). This diffuse, oppositely charged layer provides an effective screening mechanism for the surface charge, leading to an exponential decrease in effective surface charge with distance. This effect is described by electric double layer theory and must be accounted for in these systems. While the impact of this effect will vary

based on the geometry and general makeup of the system, it is invariably exponentially decaying in nature and therefore has a corresponding decay constant, or characteristic length, known as the Debye length. For our sphere–plane system, following the work of Israelachvili,[79] the double layer force can be described as:

$$F = \kappa R Z e^{-\kappa D},$$ (1.6)

where κ^{1} is the Debye length, R is the radius of the sphere, D is the separation distance, and Z is the interaction constant:

$$Z = 64\pi\varepsilon_0\varepsilon \left(\frac{k_B T}{e}\right)^2 \tanh^2\left(\frac{ze\psi_0}{4k_B T}\right),$$ (1.7)

where ε_0 is the permittivity of free space, ε is the dielectric constant, k_B is the Boltzmann constant, T is the temperature, e is the charge of the electron, z is the valency of the ions in solution, and ψ_0 is the surface potential. The Debye length is then defined as:

$$\kappa^{-1} = \left(\sqrt{\sum_i \frac{\rho_{\infty i} e^2 z_i^2}{\varepsilon\varepsilon_0 k_B T}}\right)^{-1},$$ (1.8)

where $\rho_{\infty i}$ is the ionic concentration of ion i in the bulk (at $x = \infty$). From this, we see that the Debye length decreases with both a larger proportion of multivalent to monovalent ions, as well as with increased ion concentration more generally. Taking the solution temperature, probe radius, ion distribution, and ion concentration as constants allows the force to be stated as a basic exponential:

$$F = A e^{-\kappa D},$$ (1.9)

where A is the amplitude. This can then be fitted to experimental data to determine the Debye length of a given system, which can then be compared to calculated values. By

identifying any discrepancies, we can isolate the impact of other effects beyond those implemented in this model.

Dipole interactions, the impacts of which are often referred to as van der Waals forces, dominate the interaction between surfaces at extremely short range. They revolve around the interactions between three types of dipoles: permanent, induced, and instantaneous. Permanent dipoles are those that are preexisting within a material. Induced are those that are generated in a material by exposure to a dipole. Instantaneous are those that arise due to electromagnetic vacuum fluctuations and are present in any material.

These interactions can themselves be broken down into three types: permanent–permanent (orientation or Keesom), permanent–induced (induction or Debye), and spontaneous–induced (dispersion or London). All are proportional to $1/r^6$ and we will address each in turn, following the work of Cappella and Dietler.[78]

The Keesom force is the interaction that occurs between two permanent dipoles and its potential has the form:

$$W_K(r) = -\frac{\mu_1^2 \mu_2^2}{3(4\pi\varepsilon_0\varepsilon)^2 k_B T r^6},$$
(1.10)

where μ_1 and μ_2 are the dipole moments of the two atoms or molecules.

The Debye force is the interaction between a permanent dipole and an induced dipole it creates and its potential has the form:

$$W_D(r) = -\frac{\mu_1^2 \alpha_{02} + \mu_2^2 \alpha_{01}}{(4\pi\varepsilon_0\varepsilon)^2 r^6},$$
(1.11)

where α_{01} and α_{02} are the electronic polarizabilities of the molecules

The dispersion (or London) force is the strongest contribution for all except the most polarized of materials and describes the interaction between a spontaneous dipole and its induced dipole.[i] Its potential was described by London in 1937 and has the form:

$$W_L(r) = -\frac{3}{2}\frac{\alpha_{01}\alpha_{02}}{(4\pi\varepsilon_0)^2 r^6}\frac{(h\nu_1)(h\nu_2)}{h\nu_1 + h\nu_2},\tag{1.12}$$

where $h\nu_1$ and $h\nu_2$ are the first ionization potentials of the molecules and h is the Planck constant. This force creates interactions even between two materials that do not have permanent dipoles. It is also the only one of the three that can suffer from retardation effects. As it is due to fluctuations that are short-lived, it is possible for the configuration of the first molecule to have changed by the time the reflected field returns from the second molecule. This is especially likely in interactions that are taking place in a liquid medium, where the speed of light is significantly reduced. The dispersion force in these cases will decay as $1/r^7$ when at an intermediate distance.[80]

From this we can identify that surface charge and dipole effects operate at effectively different length scales due to the differing impact of distance. Surface charge interactions dominate at longer ranges out to several microns whereas dipole interactions take over within a few tens of nanometers of separation. Both effects are strongly impacted by surface geometries and are sensitive to deformation. In the system studied here, deformation of probe or surface will lead to increased contact area providing space for additional interaction as well as complicating the process of determining the initial point of contact. This deformation can be made more likely with increased temperature depending on the material used, such as the oil used for the

---

[i] Despite this being the most common explanation in texts on the subject and providing an excellent sense of symmetry with the prior two forces, it is not, strictly speaking, correct. The effect is more properly described using quantum mechanical perturbation theory and is explained as such in the 1937 work by London.

experiments in Chapter 5. Given the variety of potential variables and impacts thereof

it is important to be mindful of the effects both during experimental design and analysis.

Chapter 2

Experimental Methods

2.1. Equipment

2.1.1. Atomic Force Microscopes

In the course of characterizing our samples, we utilized two AFMs. One was a commercial unit produced by NT-MDT and the other was a custom high pressure high temperature (HPHT) system built by Dr. Steven Higgins of Wright State University, Ohio. Each of these will be described in turn.

NT-MDT Ntegra

The Ntegra is an exceptionally versatile model of AFM produced by NT-MDT and is able to be used in a variety of configurations (Figure 2.). Our experiments utilized both the sample scanning and the tip scanning modes of the microscope, as well as taking data both at ambient conditions and in a liquid environment.
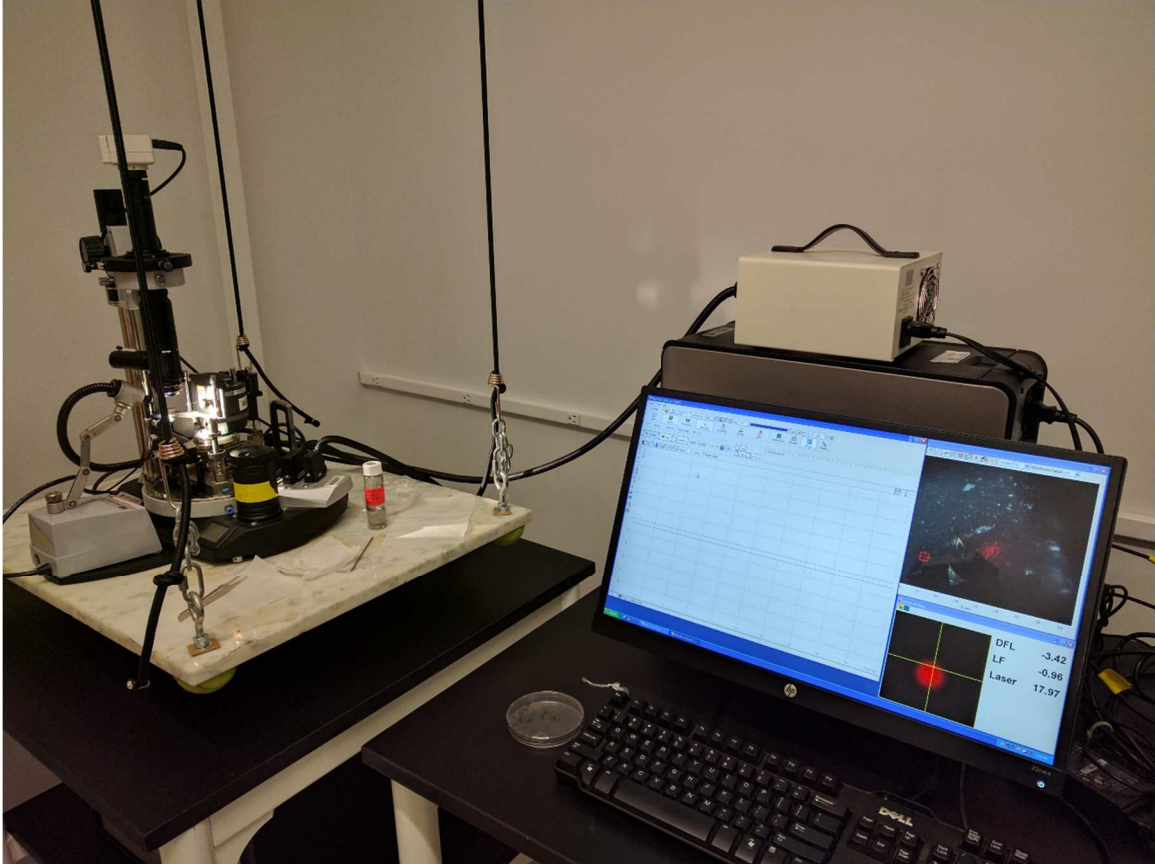
Figure 2.1: Photograph of the NT-MDT Ntegra AFM performing an experiment. The AFM is placed on a suspended marble table (left) which functions as a vibration reduction stage. Multiple light sources (boxes at far left center and right top) provide illumination via fiber optic cables. The AFM is connected to a desktop computer (bottom right) to display the visual output from an optical microscope mounted on the AFM, the cantilever deflection values, approach and retract behavior of the coarse adjustment mechanism, and real-time visualization of the scanning and force curve data.

The sample scanning mode of the microscope is the most conventional and involves placing the sample on top of a piezo electric stack and underneath an AFM probe in a static holder, referred to as the Universal Head (Figure 2.2A). After the probe and sample are aligned vertically the sample is gradually raised until it comes into contact with the probe. After contact is made, current is applied to the piezo electric stack to expand and contract the stack. This movement can be used either for rastering the

sample back and forth under the probe to create topographical images or raising and lowering it vertically to take force curve data.
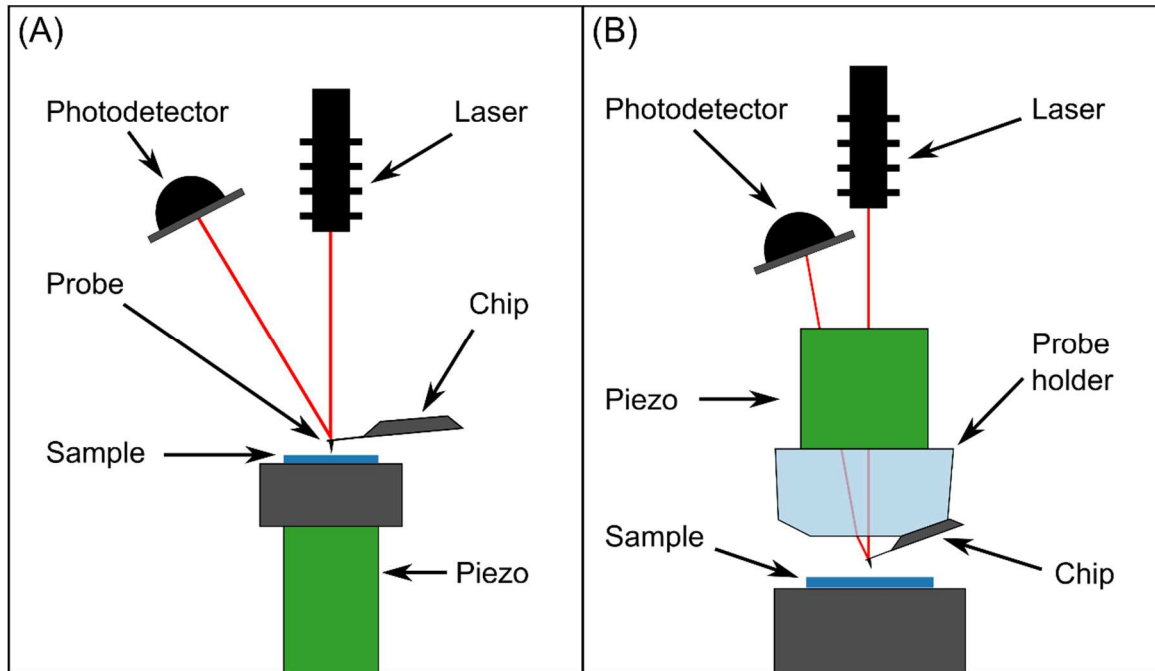
Figure 2.2: Schematic of the AFM sample scanning mode using the NT-MDT Universal Head (A) and tip scanning mode using the NT-MDT SMENA Head (B). For the sample scanning mode (A) a laser beam is directed onto the end of an AFM probe attached to a chip. The laser beam reflects off the probe into a photodetector so that vertical deflections and torsions of the cantilever can be measured as vertical and horizontal displacements of the reflected laser beam, respectively. In this arrangement, the sample is placed on top of a piezo. As the piezo moves, the sample is rastered back and forth under the stationary probe. In the tip scanning mode (B), the laser is also aligned on the top of the AFM probe. However, since the probe holder is attached directly to the piezo a series of mirrors are required to direct the laser beam around the piezo and through the transparent probe holder onto the probe. These mirrors are obscured by the piezo in the schematic. After reflecting off the probe, the laser light is directed into a photodetector and monitored in the same way as the sample scanning mode. Since the probe is connected directly to the piezo, as the piezo moves, the probe is scanned back and forth across a stationary sample.

The other primary operating mode of the microscope uses the tip scanning SMENA Head (Figure 2.2B). This is useful when the sample or the containment vessel for the sample is heavier than can be supported or moved by the piezo directly, as it has a

31

weight capacity of only a few grams. In this mode the probe is attached to the piezo, which is itself moved instead of the sample, in the reverse of the previous mode.

While most measurements with an AFM are taken in ambient conditions, it is also possible to take data in a liquid environment. With the Ntegra SMENA Head, this requires a specialized liquid cell (model: MP3LCNTF). The cell consists of a sapphire substrate and a surrounding 70 mm diameter Teflon® ring separated by a silicone rubber gasket. These are held together with a stainless-steel clamp and yield a cell with a 4 ml volume. All the force curve data taken in this work with this microscope used this cell.

HPHT AFM

In contrast to the commercially available Ntegra, this AFM was designed solely for experiments in extreme liquid environments and is less flexible in its design as a result. It is only capable of running as a sample scanner, rather than a tip scanner (Figure 2.3). While it may be less flexible than the Ntegra, it offers access to testing conditions not possible with any other AFM.

The HPHT AFM used in this work is a custom design that is divided into two main chambers (Figure 2.3A). The upper chamber is small and liquid-filled holding the probe and sample. Captured laser light is recorded by a photodetector (Figure 2.3B-1) after being emitted by a laser source (Figure 2.3B-2), reflecting off the AFM probe (Figure 2.3B-3), and passing through a transparent viewing panel (Figure 2.3B-4). The probe is positioned above the sample (Figure 2.3B-5) in the upper chamber, while a heating element (Figure 2.3B-6) encircles the upper chamber to regulate the temperature of the aqueous solution (Figure 2.3B-7) in which the measurements are taken. The lower, larger chamber contains the piezo and coarse approach mechanisms (Figure 2.3B-10) and is pressurized with gas (Figure 2.3B-9). The two chambers are separated by a

32

flexible Viton membrane (Figure 2.3B-8) which transfers pressure between them but keeps the sensitive electronics isolated from the liquid. A more complete description of the workings of this AFM via that of its predecessors can be found in the works of Higgins, et al..[81–83]
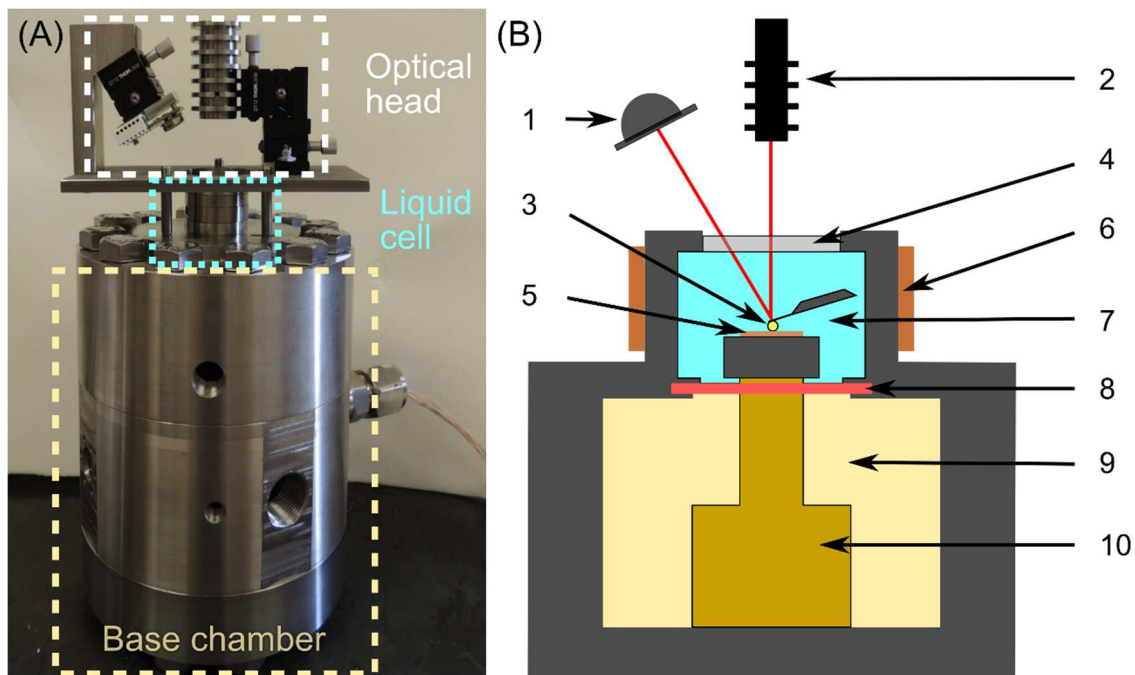
Figure 2.3: The HPHT AFM custom-built by Dr. Steven Higgins at Wright State University (A). Two main chambers include the liquid cell and the base chamber. Additionally, an optical head on top of the device provides the capability for aligning both the laser on the probe and the probe on the sample surface. The AFM can be broken down further into components shown in the diagram (B) including: 1 – a photodetector, 2 – laser source, 3 – AFM probe, 4 – transparent viewing panel, 5 – sample, 6 – heating element, 7 – aqueous solution, 8 – Viton membrane, 9 – pressurized gas, 10 – piezo and coarse approach mechanisms.

2.1.2. Optical Microscope

Optical images were taken with a CCD camera attached to an Olympus inverted microscope model IX71. Objectives used included: MPLFLN-BD 5× (0.15 NA), MPLFLN-BD 20× (0.45 NA), MPLFLN-BD 100× (0.9 NA), and LUCPLFLN 40× (0.6 NA). The primary imaging mode was standard reflective microscopy or bright field.

Although some samples required the use of dark field microscopy which captures only scattered light. Any samples manipulated on the stage of the microscope used a Newport Corporation XYZ translation stage, model 460-XYZ. This translation stage was also instrumental in the creation of the functionalized probes, both attaching the spheres to the tipless cantilevers and functionalizing the probe surfaces.

2.1.3. Other Equipment

Other sample characterization equipment used in this work included a scanning electron microscope (SEM) by Hitachi (S-4700) to examine the surface of colloidal probes and a Renishaw inVia Raman Spectrometer to test for the presence of GO on probe surfaces. For sample preparation, a Novascan UV/Ozone cleaner (PSDP-UV$_4$TUV) was used for sample cleaning and GO reduction, a Laurell WS-400Bz-6NPP-Lite Spin Processor was used for deposition of thin films, and a Thermo Scientific Lindberg Blue M V0914A vacuum oven was used for drying samples. All water used was filtered by a Synergy UV picopure system from Millipore.

2.2. Sample Preparation

2.2.1. Solids

Cleaning

The first step in almost any experiment involved cleaning all surfaces. The most basic step was sonication in water with surfactant using a Fisher bath sonicator. Surfaces were cleaned for 30 minutes at 60 °C. Especially sensitive samples received an additional 30 minutes at 60 °C using only water to ensure that all traces of surfactant were removed. The most sensitive samples received 30 minutes under high intensity UV light followed by 30 minutes of exposure to ozone in a UV ozone cleaner. This removes any trace organic contaminants from the surface. The exception to this

treatment was for mica, which was freshly cleaved immediately before undertaking the experiments, leaving a clean, atomically flat surface.

GO optical characterization samples

The graphene oxide samples examined in Chapter 3 were removed from the emulsion via pipette and then dried under vacuum at room temperature for more than two weeks. They were then suspended in water by one hour stirring with a magnetic spin bar followed by two minutes of mild sonication by bath sonication, then an additional several hours of stirring. The samples were spin-coated for 3 minutes at 3000 rpm onto silicon substrates with a 300 nm SiO_2 layer (Graphene Supermarket). The concentration of the suspensions was limited such that only approximately 1% of the surface area of the silicon was covered to limit the risk of overlapping flakes.

Surface treatments

After cleaning, some surfaces required some form of coating. Samples that required a positive surface charge were coated in an amine by suspending them in a liquid solution for 30 minutes. For AFM probes coated in this way, great care was taken to ensure that only the end of the probe was in the liquid as coating the cantilever would ruin it (Figure 2.4). This requires lowering the probe to keep pace with the evaporation of the solution during this time period. Surfaces that needed a hydrophobic coating had a thin layer of silane applied by vapor deposition, in which a droplet of the silane was placed in a sealed desiccator with the surface. The volatile droplet of silane evaporated and applied a molecularly thin coat of the molecule to the surface. As this process requires that the surface be exposed to the airborne silane, placing another object on top of the surface would prevent it from occurring and used to generate occlusions or patterns on the surface in the coating. A specific example of this process is detailed more fully in Chapter 4.
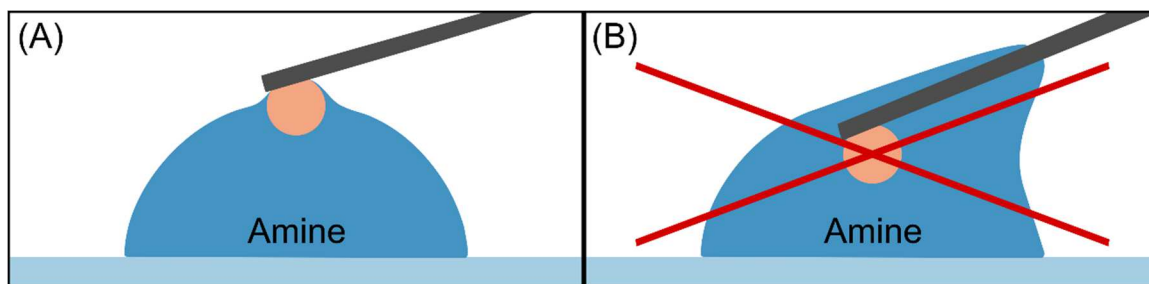
Figure 2.4: During the process of coating the AFM probes in amine it was vital to only submerge the spherical portion of the probe in the amine droplet (A). To accomplish this, the probe needed to be continuously lowered into the droplet as the droplet shrank due to evaporation. We avoided pushing the probe too far into the droplet (B) because applying a coating of amine to the cantilever lead to a thin film coating the reflective side of the cantilever. This reduced the reflectivity of probe (to laser light). In some cases, a thin film even formed between the sphere and the cantilever, changing the spring constant of the probe.

2.2.2. Liquids and Emulsions

Brines

The measurements for the high pressure high temperature experiments were taken in 1500 ppm salt brine (propriety composition Shell Oil). The brine solutions were prepared immediately before use by combining picopure water (Millipore) with NaCl, $MgCl_2 \cdot 6H_2O$ and $CaCl_2 \cdot 2H_2O$ (Fisher Scientific, certified ACS grade).

Bubbles

For force curves taken at a liquid–liquid interface, it was necessary to create bubbles of one liquid submerged in a different liquid. The most effective method to do this required the development of a silicon surface patterned with a hexagonal grid of hydrophobic patches on a hydrophilic background (detailed in Chapter 4). Once the substrate had been created, the liquid cell for the Ntegra microscope was filled with 3 ml of picopure water. Then, using tweezers, one end of the substrate was immersed into the water, 30 microliters of heptane were then applied to the portion of the substrate not in the water and while the heptane still wetted the surface it was quickly

pushed under water. This created the best way for the heptane to remain attached to the hydrophobic patches while the substrate was under the water. Other variations of the procedure, such as attempting to apply the heptane to the surface of the substrate under the water or creating a water/heptane emulsion in a syringe and injecting the bubbles into the liquid cell were not as effective and could take several hours of attempts before producing viable bubbles.

2.3. Imaging

2.3.1. Optical

Image acquisition

When acquiring images for detailed statistical analysis it is not sufficient merely to take a single image as would be otherwise typical. This is because the standard image has only a range of zero to 255 for the brightness of each pixel and this is an insufficient level of granularity to consistently detect shifts between layers as they occur. Instead taking a series of images and then averaging across them allows for some level of noise reduction and gives a more accurate brightness value for each pixel. This is most easily accomplished by using the time lapse feature of the image software (ScopePhoto). For the images analyzed in this work, a series of 100 images was captured for each location on the sample and then averaged together giving a final image with the mean value.

Processing

After acquiring these images, we execute several processing steps to improve the images to the stage where it is possible to analyze them quantitatively. We used ImageJ,[84] an open source image processing program, to carry out many of these steps. A diagram detailing the results of each step as applied to actual data is provided in

Chapter 3, Figure 3.2. To generate an averaged image, we combined the original set of images into a stack and used the "z-project" function set to "mean". It is important to change the image type to 32-bit before averaging, otherwise the final image will suffer the same problems as the originals. Typically, only one of the color channels is processed for a set of images, as the relationship between brightness and layer number will be different for each and one is usually clearly preferable, depending on material and substrate choice. To account for shifts in background lighting intensity during the course of the time lapse session, it was occasionally necessary to normalize the brightness values across the set. This was done by diving the brightness value of each pixel by the median brightness of the entire image, for that image. This is especially important when processing images of the empty substrate as these images will not undergo the later plane fitting and are instead averaged together with several locations from the empty substrate. This is best accomplished by taking sets of images at three to five locations on an empty substrate, normalizing and averaging them as above, and then taking the median values of the final images from each location by using the "z-project" function set to "median". This will eliminate any minor imperfections or bits of debris that may be present in one location but not in the others.

After the above steps have been completed for all sets of images, the correcting process can begin. We again used ImageJ for this by opening the averaged image of a location on a sample and the averaged image of the empty substrate and then using the "image calculator" function set to "divide" the sample image by that of the empty substrate. Sometimes after this process, there can be errors at the edge of the image, particularly if the edge is erroneously saved as zero brightness. Cropping a four pixel border from each image resolved the problem for our software, ScopePhoto.

The next step cannot be readily carried out in ImageJ so we had to export the divided image to Gwyddion,[85] an SPM image processing program. The image needs to be exported in ImageJ's "text image" format, as this is the only format that preserves the exact values in the image rather than relative ones. It generates an ASCII text document that gives a sequential list of the numerical values for each pixel. These can be opened by Gwyddion as "raw data" files when provided with the image size and scale, which must be consistent from image to image. Once the image is open in Gwyddion, the next step is to select the background portion of the image using the "mark with" tool. Adjust the minimum and maximum values to create a mask that contains most of the background portion, but it is preferable to exclude some portion of the background rather than include any flakes. Once the mask is created, use the "remove polynomial background" tool to create a plane that is fitted to the background. Use the lowest polynomial degree that will correct for background distortion (see Chapter 3) and be sure to check the "extract background" box as this background is what is actually needed. Save both the original image and the extracted background as "ASCII data matrices" to re-import them to ImageJ.

Next the original image and the extracted background are re-imported into Gwyddion, as "text images". It is important to use the version of the original image exported by Gwyddion to maintain the correct scale relative to the extracted background. Next, divide the image by the extracted background using the "image calculator" function. At this stage in the process, if contrast inversion is observed in the image, the "InvertMountain" macro (Appendix A) we developed can be applied. As an example, this will appear as light or dark patches within flakes that are otherwise dark or light, respectively. With the image open, run the macro setting the inflection point to the brightness value at which the contrast trend reverses. Adjust other parameters as

39

required according to the documentation and press "ok". Next, the image must be converted from brightness values to thickness values. Here a function can be acquired from the literature or generated using a co-located AFM image. This function is then applied to the image through the "math/macro" function. The built in ImageJ "analyze particles" function was then used to generate a list of flakes, their areas, and average thicknesses.

2.3.2. AFM

Acquisition

When acquiring an image using AFM multiple modes can be used, but in this work predominantly standard contact or dynamic modes were preferred. These differ chiefly which parameters are used in the feedback loop.

In contact, the simplest mode of AFM operation, the probe is brought into contact with the sample and rastered over the sample surface while attempting to maintain a constant value for the deflection of the cantilever. This is achieved by automatically adjusting the extension of the piezo as it moves across the sample through the use of a computer-controlled feedback loop. The image produced is then a map of the piezo extension at each pixel in the image. This is, in effect, a topographical map of the surface of the sample. Images taken using this mode featured in this work were taken with sharp gold-coated silicon nitride probes from BudgetSensors, model SiNi.

In dynamic mode, the cantilever of the probe is oscillated close to the resonant frequency of the cantilever and by adjusting the piezo extension to keep a constant magnitude of the oscillation a consistent the tip and sample can be achieved. This can be more complex than contact mode as the interaction between tip and sample is no longer strictly based on contact and force displacement of the cantilever but rather a

coupled interaction between the tip and sample, which can be modulated by changes in the material of the sample. This can be helpful, as looking at changes in the phase of the oscillation can reveal changes in material that are not obvious as strict changes in topography. However, this can also complicate height measurements as the tip-sample spacing at a given oscillation magnitude may not be constant across two different sample materials. The image produced in this mode is usually the same as contact mode, i.e. a map of piezo extension. Images taken using this mode featured in this work were taken with sharp silicon probes from Mikromasch, model HQ:NSC15/AL BS.

Processing

After data is initially acquired for an AFM image, substantial processing is usually required to render it into a useful state. While there are many steps that can be taken to process these images there are three main steps that are required for almost all cases: compensation for sample tilt, piezo motion, and thermal motion. These will be described in order of decreasing severity.

The largest artifact present in an AFM scan usually comes from tilt in the sample itself. The piezo typically has a vertical range of at most 10 μm and leveling the sample to substantially smaller degree is usually not possible. The first operation employed is to fit a first degree polynomial surface to the image and then subtract these values from the height image.

The next largest artifact is due to the nature of the piezo. The piezo in the microscopes used in this work are not capable of true x-y translation, but rather rely on bending the piezo by extending or contracting stacks on the four cardinal directions. This leads to a curved second degree polynomial surface being, effectively, added to all height values in an image. To remove this artifact, therefore, such a surface must be fitted to

the image, typically pixels that correspond to the substrate or other locations known to be of equal height, and then subtracted from the entire image.
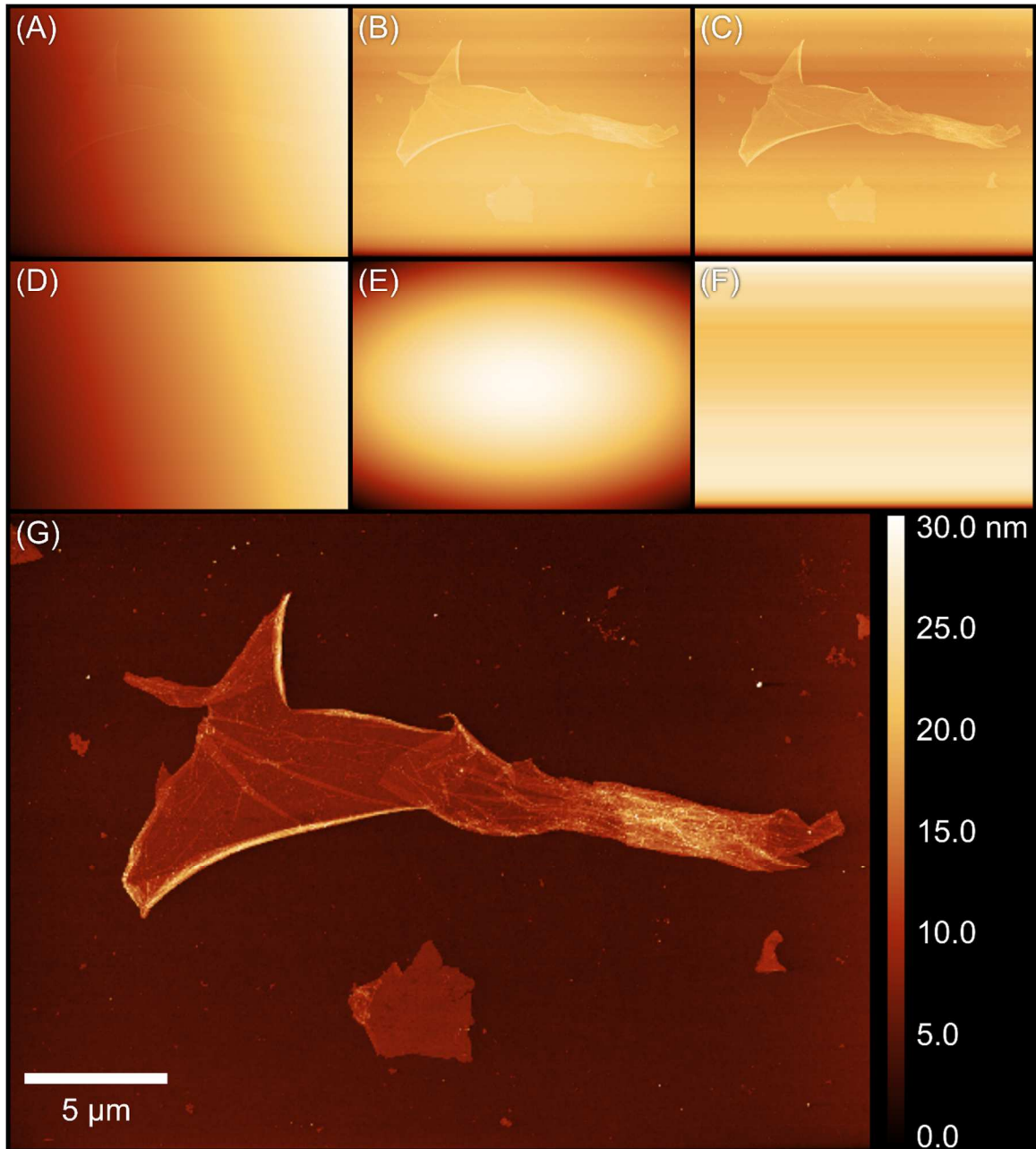
Figure 2.5: Steps undertaken during a typical AFM image processing procedure. The initial image (A) has a first degree polynomial surface fitted to it (D), and this surface is then subtracted from it, eliminating sample tilt (B). This image is then fitted with a second degree

polynomial plane (E), and this surface is, again, subtracted from it, eliminating the effects of piezo non-linearity (C). Finally, a linear fit is applied to each scan line (F) and subtracted, eliminating the influence of thermal expansion during scanning, leaving the final image (G), which may or may not require additional processing. Sample is GO flakes on silicon substrate.

The last common artifact comes from thermal expansion and contraction in the sample. As AFM scans can often take 30 to 60 minutes to acquire, small fluctuations in temperature can and will take place during this time period. As the scale of the features in these images is often in the nanometer range, even expansion or contraction by hundredths or thousandths of a percent can have a substantial impact. As the effects of this thermal motion are across time, each scan line in the image will show a different trend, since the beginning of successive lines may be separated by tens of seconds. To compensate for these changes which are often near-linear on the timescale of a single scan line, a simple linear fit can be made to regions of the line that are known to be flat and then subtracted from each line.

2.4. Probe Manufacturing

All of the probes used for force spectroscopy in these experiments were manufactured by hand in the lab. The process requires affixing a chip with a tipless cantilever to a layer of polydimethylsiloxane (PDMS) on glass that is attached to an armature which is connected to a translation stage on the inverted microscope. Next a coverslip that is covered with several thousand micron-scale silica spheres is placed onto the stage of the microscope along with a separate coverslip that has had several 500 µm diameter droplets of Ace Hardware Marine epoxy applied to it. The chip is lowered from above until both the coverslip and cantilever are simultaneously in focus using the 5× objective on the microscope. Next the cantilever is moved over an epoxy droplet (Figure 2.6A) and gradually pushed forward to the very edge of the droplet (Figure 2.6B). After some epoxy has been attached to the very end of the cantilever it is retracted

(Figure 2.6C) the cantilever is moved over an empty section of the coverslip and pushed gently into the glass to remove excess epoxy. The epoxy will wet the surface of the glass when it comes in contact, leaving only a thin film of epoxy on the end of the cantilever.
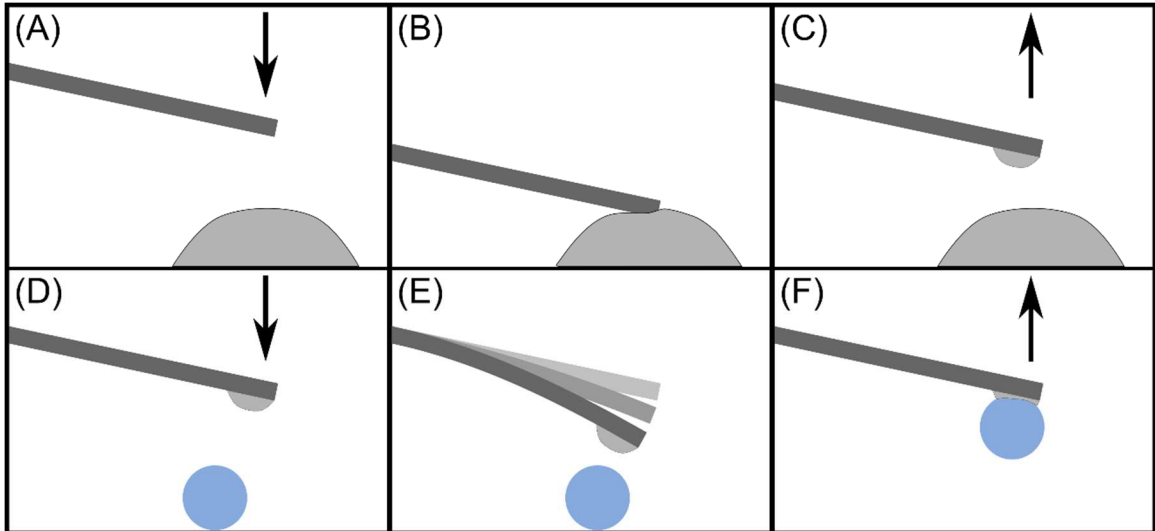
Figure 2.6: The process of making a colloidal AFM probe by hand first involves using a translation stage to lower a tipless cantilever toward a droplet of epoxy (A). The epoxy droplet is situated on a glass coverslip on the stage of the Olympus inverted microscope and the translation stage is attached to the microscope. Due to the small size of the cantilever and epoxy droplet, both must be simultaneously in focus so that the very end of the cantilever can be brought into contact with the apex of the epoxy droplet (B). Afterwards, the cantilever is retracted (C). In some cases, if too much epoxy has been added to the cantilever, it may be necessary to gently bring the cantilever into contact with the surrounding glass coverslip so that some of the excess epoxy can be wicked away from the surface, leaving behind a thin layer. The cantilever is next positioned above a silica sphere on another glass coverslip (D). If the cantilever is approached close enough to the silica sphere, a slight bump of the table on which the microscope resides is enough to send a vibration through the cantilever so that it touches and picks up the silica sphere (E). Then the probe is retracted (F) and left alone so the epoxy can cure.

Next the cantilever is moved to the coverslip with the spheres and a sphere that is isolated from the others by at least 30 μm is located. Here, switch to the 20× objective and verify that the sphere is perfectly spherical and is not malformed in any way. This

level of magnification is also necessary for precise centering of the sphere on the cantilever. The cantilever is then approached to within 10 µm of the surface of the coverslip and then moved slowly over the chosen sphere (Figure 2.6D). It is important to approach the sphere such that the cantilever points the opposite direction of movement to avoid scooping the sphere onto the back of the cantilever, which will ruin it. Once the tip of the cantilever has been centered over the sphere, a light tap on the countertop will transmit a vibration through the cantilever bending it momentarily downwards and picking up the sphere (Figure 2.6E). Using the lowest amount of force is recommended as otherwise it is possible to pick up excess spheres, again ruining the cantilever. After the sphere has been acquired, retract the tip away from the surface (Figure 2.6F), remove the new probe, and allow it 24 hours so that the epoxy may cure.

The probes manufactured for these experiments used a variety of cantilevers including Bruker model MLCT-O10 (aluminum coated silicon nitride), NanoWorld PNP-TR-TL-Au (Double gold coated silicon nitride), and NanoAndMore model All-In-One Al-TL (aluminum coated silicon nitride). The spheres used were from Bangs Laboratories, non-functionalized silica spheres (mean diameter 7.27 µm). All spheres were attached with Ace Hardware Marine epoxy.

A two-step process was used for the spherical probes coated in graphene oxide. First, the sphere portion of each probe was coated with an amine (Gelest (3-trimethoxysilylpropyl) diethylenetriamine)). To apply the coating, we combined 1.98 g of picopure water with 20 ml of the amine in a plastic Petri dish. After stirring thoroughly to combine, we applied 10 ml of this solution to a coverslip on the stage of the inverted microscope. The chip and probe were then attached to the translation stage and armature as above and lowered until the sphere came into contact with the droplet. It is important that only the sphere and the very tip of the cantilever comes into contact

with the amine to avoid coating the rest of the cantilever, affecting its performance (Figure 2.4). Therefore, a careful eye must be kept on the probe to keep it in the solution for the entire 30 minutes as the solution will evaporate, lowering the liquid level below the sphere. After 30 minutes, remove the probe to a 110 °C oven for 15 minutes to cure. After the probe has cured, it is next dipped into a dispersion of GO in water. This is an identical setup as the amine coating and again, great care must be taken to ensure that only the sphere comes into contact with the droplet of GO dispersion (Figure 2.4) over the course of the 30 minutes, with similar attention paid to the lowering liquid level. Once this process is complete, the tip is placed in a vacuum desiccator for at least one hour to remove residual water and can then be stored in a traditional tip box until it is needed.

To functionalize the probes with oil for the high pressure high temperature testing, a two-step process is again employed. First the probe is rendered hydrophobic with a coating of silane (Gelest (Tridecafluoro-1,2,2-Tetrahydrooctyl) Trichlorosilane). The probe is sealed in a glass desiccator with 3 ml of the liquid silanizing agent and left for 2 hours. After the coating is applied the probe is then briefly dipped in a droplet of crude oil that has been placed on the stage of the inverted microscope using the previously described apparatus. Only a momentary immersion of the probe is required and again, only this sphere and the very tip of the cantilever should come into contact with the oil. The probes were then dried under 30 inHg vacuum at 150 °C for 11 hours followed by 11 hours of cooling while still under vacuum.

2.5. Force Spectroscopy

2.5.1. Structure

The basic piece of information that is obtained when performing force spectroscopy is called a force curve. This is a plot of the deflection of the cantilever as a function of piezo extension as it moved toward the sample, into contact with the sample's surface, and then retracted away from the surface (Figure 2.7, top). It can be broken into several basic parts. First, the probe is approached toward the surface (Figure 2.7A). This is also referred to as the "no-deflection" region, as the probe is far enough away from the surface that it is not yet interacting with it, and thus does not deflect. Next, when the probe approaches closely enough to the sample it may "snap-on" to the surface, experiencing a negative (attractive) force (Figure 2.7B). The piezo continues to extend, pushing the probe into full contact and deflecting the cantilever upwards (Figure 2.7C). After reaching a pre-determined distance the piezo begins to retract (Figure 2.7C). If there is any adhesion between the probe and sample, it will hold the probe to the surface, demonstrating an attractive (negative) force (Figure 2.7D). Finally, the piezo will retract far enough such that the cantilever exerts enough force to remove the probe from the surface, referred to as a "pull-off" (Figure 2.7E).
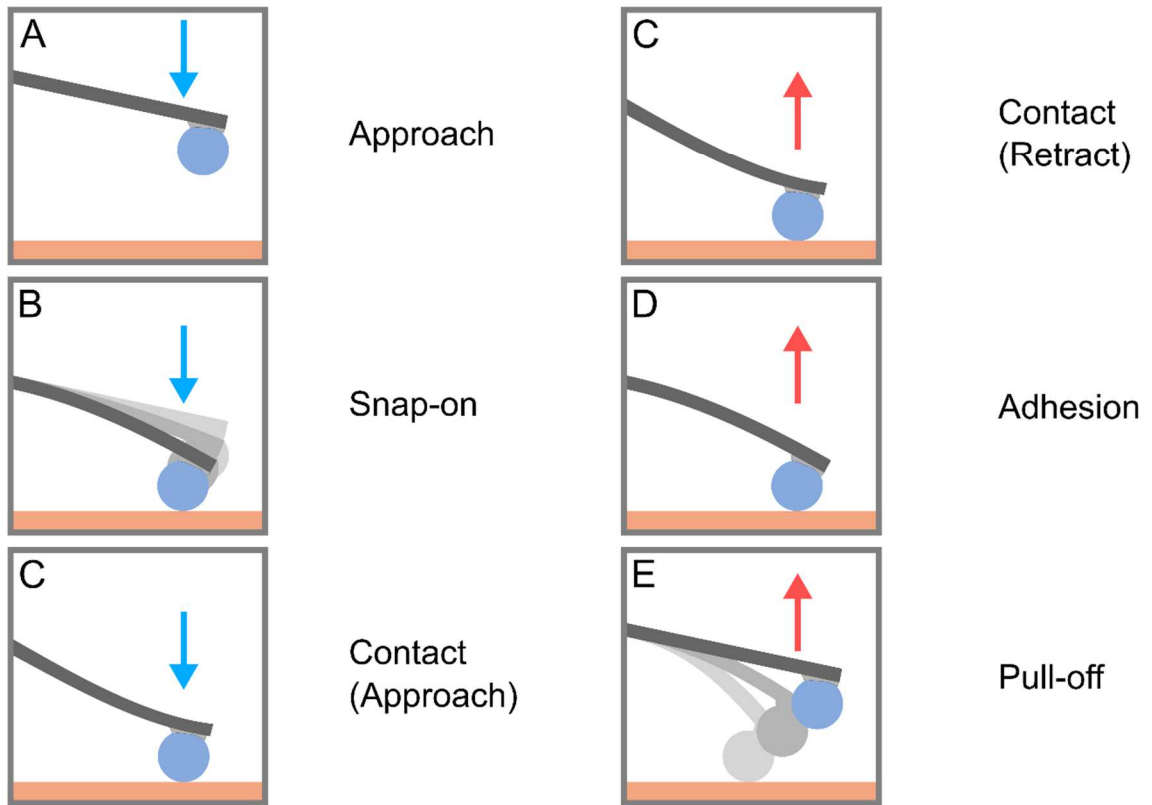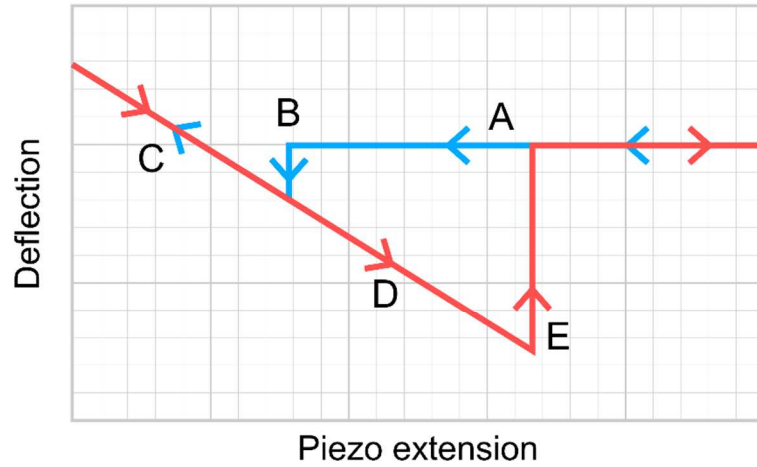
Figure 2.7: Diagram of a force curve, containing both the approach (blue) and retract (red) portions of the process (top). At bottom are shown the corresponding stages in a force curve: approach (A), snap-on (B), contact (C), adhesion (D), and pull-off (E).

2.5.2. Execution

NT-MDT

In this work, we utilized the NT-MDT SMENA head and liquid cell to take force spectroscopy measurements (see Section 1.4) at a liquid-liquid interface. These measurements were taken on bubbles of one immiscible liquid suspended in another. This necessitated that the bubbles be pinned to the substrate, so that we could identify them, position an AFM probe over the center of a single bubble, land on the bubble, and perform the measurements. For these experiments, we used both a bare silica sphere colloidal probe and a GO coated probe (detailed in Chapter 5) both before and after reduction via UV exposure. Multiple curves were taken on the same location on each bubble, with typically only one bubble being explored per experiment. Curves were taken at a speed of 1 μm/s and 2000 data points were recorded. For each curve, the piezo started at full retraction, was extended through contact with the bubble until it reached a preset upper limit to avoid rupturing the bubble and then fully retracted.

HPHT

For the measurements taken in the HPHT experiments, all curves were taken with a single oil functionalized probe on V1 grade mica in a grid pattern with one micron spacing and five curves taken at each point in the grid. As the substrate is featureless at the visible scale, this prevents inadvertently using a single contaminated location for data acquisition. Curves were taken at a speed of 0.389 μm/s and recorded 1672 points/μm. For each curve, the piezo started at full retraction, was extended through contact with the surface until it reached a preset upper limit intended to prevent damage to the probe and then fully retracted.

2.5.3. Processing

Optical lever sensitivity adjustment

For each experiment we had to determine a new conversion between the response of the photodetector to shifting of the reflected laser spot and the distance moved by the cantilever. We accomplished this by taking a measurement on a sample which experienced minimal deformation under the applied force of the probe. This could be included in the normal sample data if the surface of interest was rigid or required additional measurements on a different sample if it exhibited substantial deformation. In either case, when attempting to force the probe into the rigid surface by extending the piezo the cantilever is forced upwards by an amount equal to the distance extended. This shows as a linear region in the measured curve and is referred to as the "constant compliance" region (Figure 2.8 top, left gray box). By taking the slope of this region, the optical lever sensitivity, and multiplying all deflection measurements by the inverse of this value, this slope becomes negative one and the deflection converted to units of distance equivalent to that used to measure the extension of the piezo.

Alignment

Next, a baseline value for the deflection reading is determined, typically from the initial region before the probe comes into the interaction range of the sample, usually referred to as the "no-deflection" region (Figure 2.8 top, right gray box). An average value is taken for this region to provide this neutral deflection position. This is then subtracted from all measured deflection values, causing the no-deflection region to read as zero.
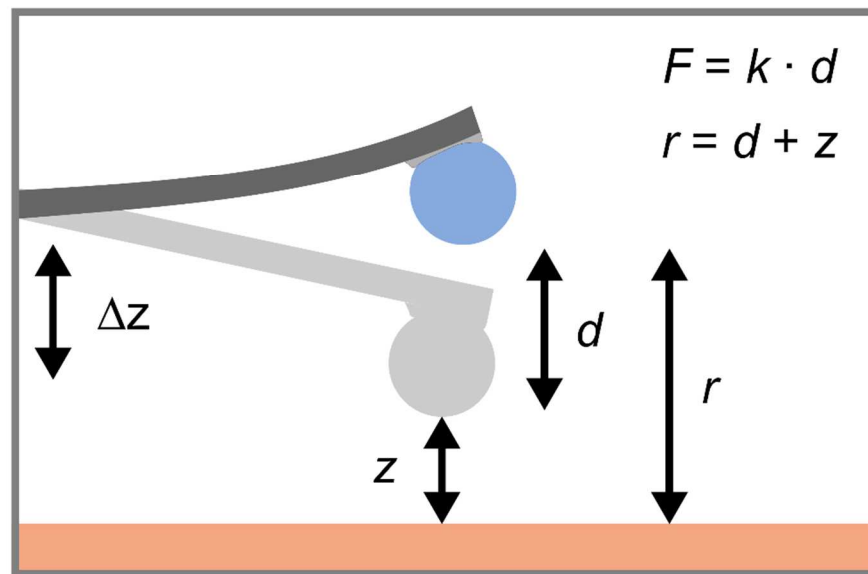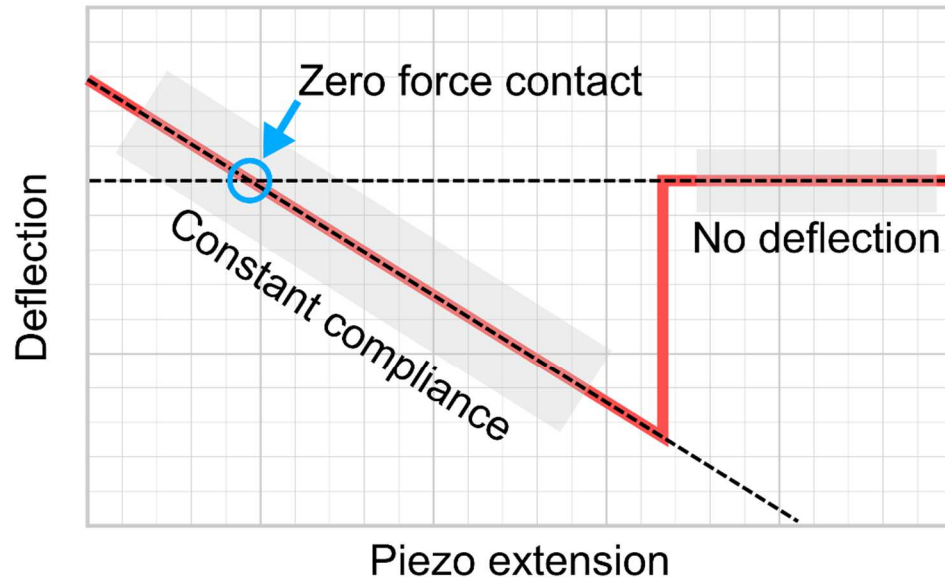
Figure 2.8: Important regions in a force curve (top) and important relations between the components of the apparatus (bottom).

Now the location of initial contact between probe and sample is determined. Typically done by finding the point of intersection between the linear fits of the constant compliance region and the no-deflection region (Figure 2.8 top, dashed lines), if the

sample can be safely considered not to deform under the pressure applied by the probe. This point would be the location where the probe is in contact with the sample, but also does not experience any deflection, i.e. the point of contact where force is zero (Figure 2.8 top, blue circle). A constant is then added to all measured piezo extension values such that the extension at this point is zero.

Conversion to force/distance

For some experiments, only the force experienced by the probe at a given point or event during the curve is of importance and processing may proceed to the next step. For some, however, knowledge of the force at a specific distance from the sample is required and the curve must be converted from force as a function of piezo extension to force as a function of tip-to-sample distance. To do this, the extension value for each point on the curve is replaced by r, the sum of the extension value z and the cantilever deflection d (Figure 2.8 bottom). This process essentially takes the position of the probe relative to the sample as given by the extension of the piezo and then modifies it by the deflection of the cantilever, which shows any additional displacement along this axis, giving the true tip-to-sample distance.

To convert the distance the cantilever is deflected to the force experienced by the probe Hooke's Law is employed and the deflection is multiplied by the spring constant of the cantilever, k (Figure 2.8 bottom). However, the nominal value of the spring constant for the cantilever supplied by the manufacturer can be, at best, considered a suggestion and will often vary by an order of magnitude from this value, even within the same batch of cantilevers. This is due to the unavoidable variance in the few-micron thickness of the cantilever from manufacturing, since differences of only a few percent in this value can have enormous impact on the response of the lever. The spring constant may instead be determined independently in the lab through a variety

of methods, such as that provided by Sader, et al.,[86] if an absolute measurement of the applied force is required. Comparative measurements with the same probe across different samples or experimental trials will not require this additional step and was the preferred method in this work.

2.5.4. Approach

For curves taken with the GO functionalized probes no measurable electrostatic forces were observed during the approach of the probe to the bubble, either attractive or repulsive. A sudden, premature contact due to attractive force between sample and probe is referred to as "snap-down" (Figure 2.7B). When long-distance snap-down due to attractive forces was observed the displacement between the neutral position of the cantilever and the lowest point of the snap-down region was taken and multiplied by the nominal spring constant of the cantilever to give a force value. For short-range snap-down was observed, due to van der Waals forces, the distance at which the snap-down occurred was measured, indicating the range at which this strong force became dominant. Any attractive or repulsive forces during the HPHT experiments were below the noise threshold and were therefore not measurable.

2.5.5. Retract

For the retract curves in both the HPHT and GO probe experiments, we measured the adhesion of the probe to the surface from the maximum deflection of the cantilever before it releases from the surface. We take the difference in this deflection from that of the neutral deflection and multiply by the nominal force constant of the cantilever to obtain the force value ($F = k \cdot d$). This was relatively straight-forward with the GO probe experiments, but the noise present in the HPHT experiments necessitated additional processing not normally required for data taken in less extreme environments. Here, we assumed that the noise from the fan was approximately normally distributed and

replaced each point with the average value of the 100 surrounding points. The adhesive force value was then taken as the difference between the lowest point on the curve and the neutral deflection point, taken as the average of all points with the no-deflection region, multiplied by the nominal spring constant of the cantilever.

Chapter 3

Optical Analysis of 2D Materials

3.1. Introduction and Theory

To explore the interactions of 2D materials with oil-water interfaces, we first needed to examine the effects of these processes in a population of nanosheets that had been exposed to them. Doing this required a way to rapidly characterize the morphology of large numbers of flakes which would not be feasible if we were required to examine each flake individually. Therefore, we developed a technique to overcome these challenges, which was published in *Nanoscale* in 2018 as "High-throughput optical thickness and size characterization of 2D materials."[87] This chapter is adapted from that article, with permission from The Royal Society of Chemistry. Our technique uses optical microscopy, which is both quick to acquire images, capable of covering thousands of sheets within each of these images, and capable of distinguishing both sheet size and thickness. Other techniques, such as atomic force microscopy (AFM), scanning electron microscopy (SEM), fluorescence microscopy, or Raman spectroscopy, are limited in at least one of these respects and would not have been

suitable for our purposes. In brief, AFM is exceptionally well-suited for providing precise height measurements at the scale required[88] but is limited in the size of the sample that can be examined to approximately 100 μm by 100 μm. It is also extremely time-consuming to examine even this small area, taking at least 1 hour to cover a sample of that size with any degree of accuracy. SEM can cover larger areas but does not provide quantitative height measurements and often requires coating the sample with a conductive layer, obscuring the atomic layer changes we are interested in. Fluorescence microscopy can provide excellent lateral size measurements for many images simultaneously but provides no information on height.[89,90] Finally, Raman spectroscopy is used to examine 2D materials, but has difficulty distinguishing between double- and few-layer material,[91] especially when functionalized,[92] nor does it provide lateral size measurements. Additionally, each of these systems are quite expensive, both in initial cost and upkeep. For all of these reasons, we based our work in optical microscopy, though it also is not without its challenges.

Although 2D materials are typically nearly optically transparent due to their extreme thinness, it is possible to use interference effects to make them visible with a standard optical microscope. By depositing the sheets on a silicon substrate that has an oxide layer of a consistent, well-defined thickness they become visible with lateral dimensions readily apparent and layer variation shown as changes in color (Figure 3.A). This is due to the nanosheet layers modulating the interference effect caused by differences in path length between light that has been reflected from the top of the oxide layer and light reflected from the bottom (Figure 3.B).[93] The effect is not constrained to a single oxide layer thickness, but works across a large range thereof, e.g. 90, 270 and 300 nm. This behavior has been demonstrated for a wide variety of 2D materials including graphene,[91,94] GO,[89,95] hBN,[96] and numerous TMDs[30,91,97,98] at

the scale of individual flakes. The interference effect is strongly dependent on choice of wavelength and oxide layer thickness, which varies the precise location of the reflection minima and maxima.[93] By selecting an appropriate value for the thickness of oxide layer and the color of light used when taking optical images, one can ensure that a high level of contrast will be present between the layer numbers of interest in a given sample, at the single flake level.
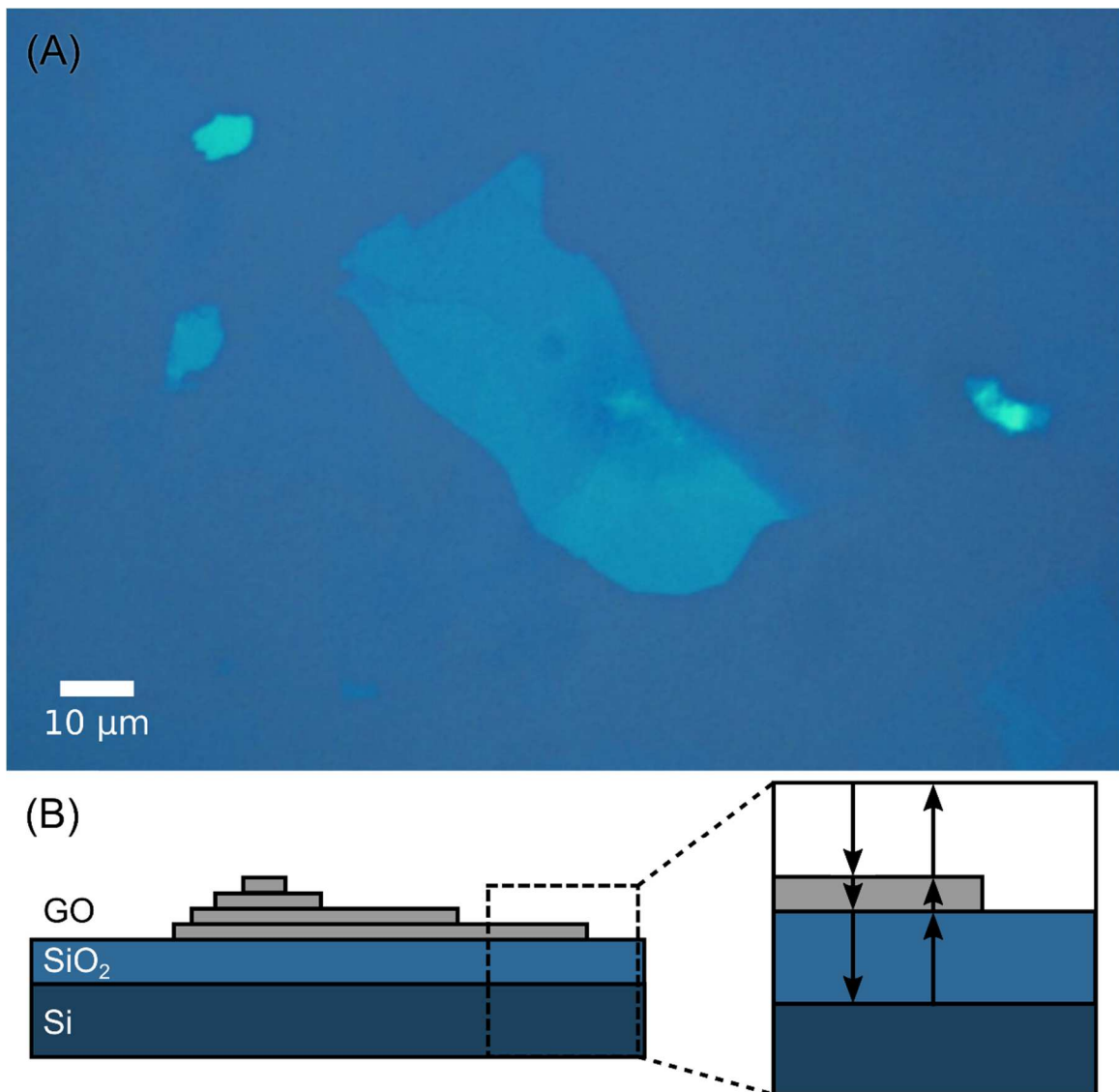
Figure 3.1: Optical image of graphene oxide flakes on a silicon wafer with a 300 nm silicon dioxide layer using white light (A). Central flake is multi-layer with single layer material on lower

right. Diagram of optical image from side (B). Gray boxes are GO sheets on top of the blue oxide layer and silicon. Right side shows path of light entering through the flakes and through the oxide layer. The light may reflect at any of the interfaces, giving rise to the interference effect.

3.2. Development and Method

The method we developed hinges on using computer processing techniques to vastly reduce the inhomogeneities present in optical images of these materials. This enables using low-magnification optical images (on the order of 1 mm^2) containing thousands of flakes, which would otherwise be obscured by the difference in brightness the inhomogeneities cause across the image. The brightest parts of the image can easily be twice as bright as the darkest, while the difference between successive layers of the 2D material may only be a few percent. These inhomogeneities are caused by uneven illumination from the light source and aberrations within the optical system itself. We remove them with a two-step process before beginning characterization.

The first step takes the image of the sample, acquired as detailed in Chapter 2: Experimental Methods (Figure 3.2A), and divides it by an image of an empty substrate acquired in the same way (not shown). The original image has a wide range of brightness values. The full extent of this variability is more clearly visible in the false-colored version of the image, Figure 3.2B, and in the brightness histogram in Figure 3.2C. The division process removes much of the characteristic distortion unique to the particular optical system used, which is unobscured in the empty substrate image, and provides an image with a more consistent background color (Figure 3.2D,E). However, the histogram for this image, Figure 3.2F, shows that the peaks associated with the individual layer numbers are still broadened and not yet completely identifiable.
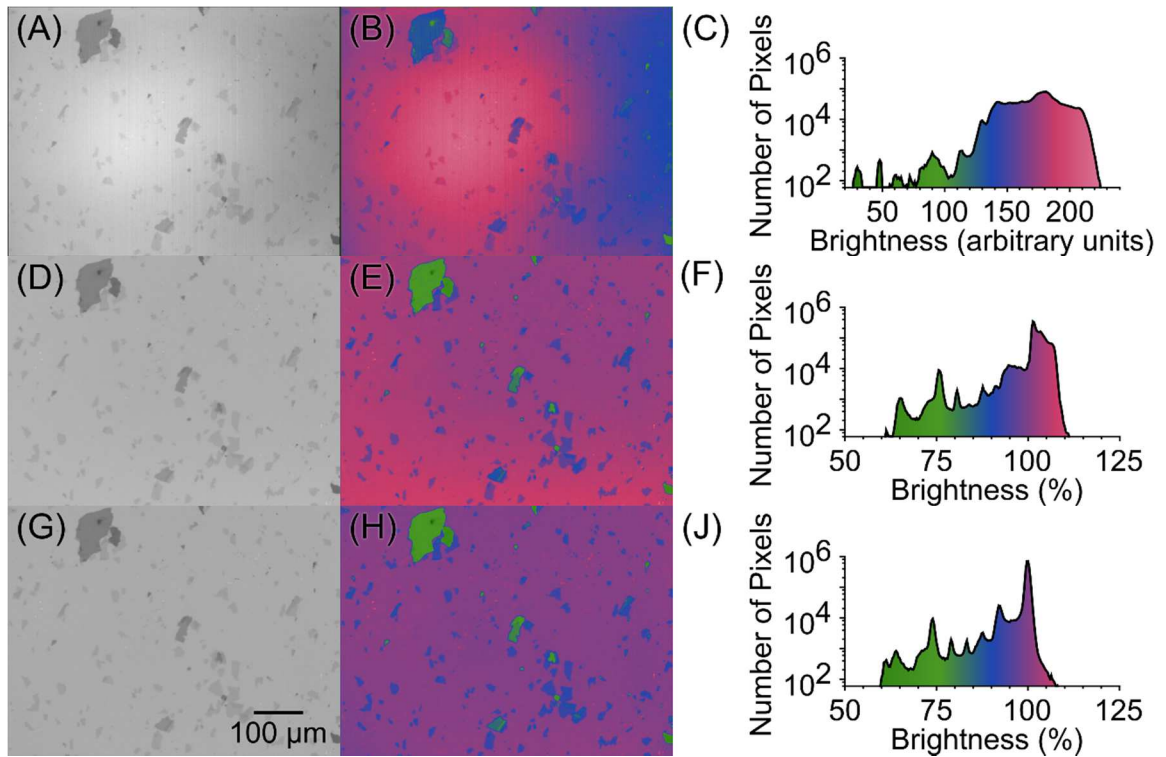
Figure 3.2: Steps in the optical characterization technique. (A) Averaged image of the sample composed of 100 images taken from the red channel. (B) False color version of (A) to highlight brightness variability. (C) Histogram of pixel brightness in (A,B). (D) Image in (A) after division by image of empty substrate (not shown), with false color version (E) and histogram (F). (G) Image in (D) after division by second order polynomial plane fitted to the brightness values of the substrate portion of the image in (D), with accompanying false color version (H) and histogram (J). *X*-axis units in (C) correspond to the brightness values from the original camera and those in (F) and (J) are percentage of the dividing image brightness.

The second step eliminates much of the remaining distortion by using the substrate as a reference point, creating a simplified plane based on the exposed portions thereof and dividing the image by this plane. This procedure "flattens" the image and is similar to a technique commonly used in scanning probe microscopy image processing. This yields an image with extremely consistent color throughout (Figure 3.2G,H) and well-defined peaks for each layer number in the brightness histogram (Figure 3.2J). In the work described here a second-order plane was used, although higher orders might be

required for some other systems. Caution should be observed to avoid using an unnecessarily high order polynomial plane which can cause "over-fitting" and create artifacts in the image that reduce accuracy in the final height values. Figure 3.3 shows a histogram with the effects of polynomial order choice for the dividing plane using the image in Figure 3.2D. Dividing by a constant (zeroth order polynomial plane, black line) does not shift the shape of the original plot, but dividing by first order (red) and second order (dark blue) planes sharpen the peaks substantially. Higher order planes (third through sixth) do not appreciably change the location or shapes of the peaks. The lowest order that provides a consistent histogram is the one that should be used, in this case second.
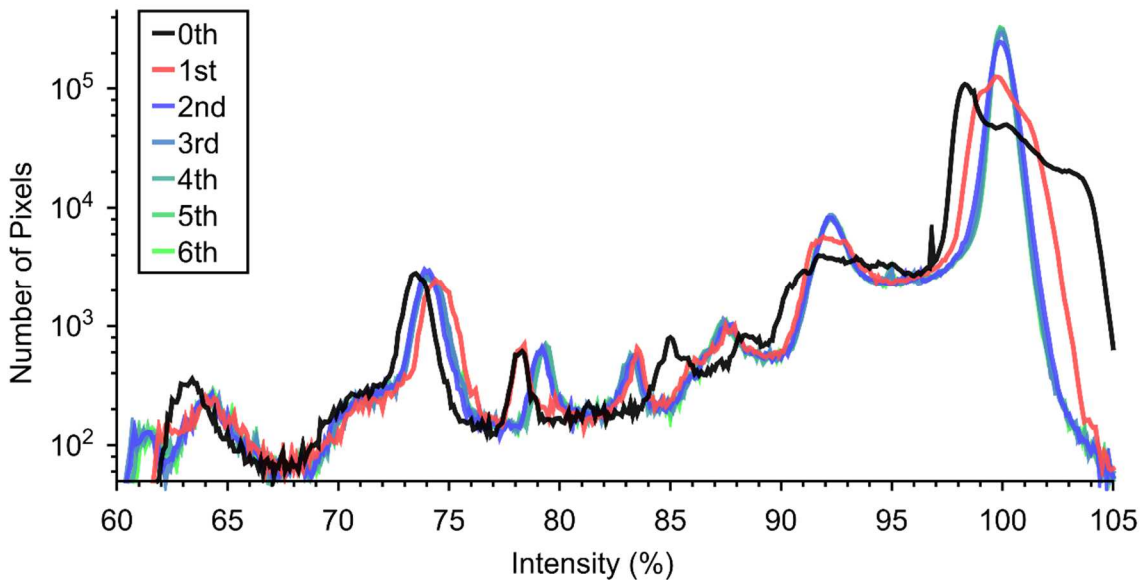
Figure 3.3: Histograms generated by dividing the image in Figure 3.2(D) by polynomial planes of varying orders that were fitted to the brightness values of the substrate portions of the image. While the shape of the normalized histogram (black) changes significantly from first (red) and second order (dark blue) planes, it does not change appreciably for higher order polynomial planes, indicating that second order is the appropriate choice for this combination of sample, substrate, wavelength of light, and optical system.
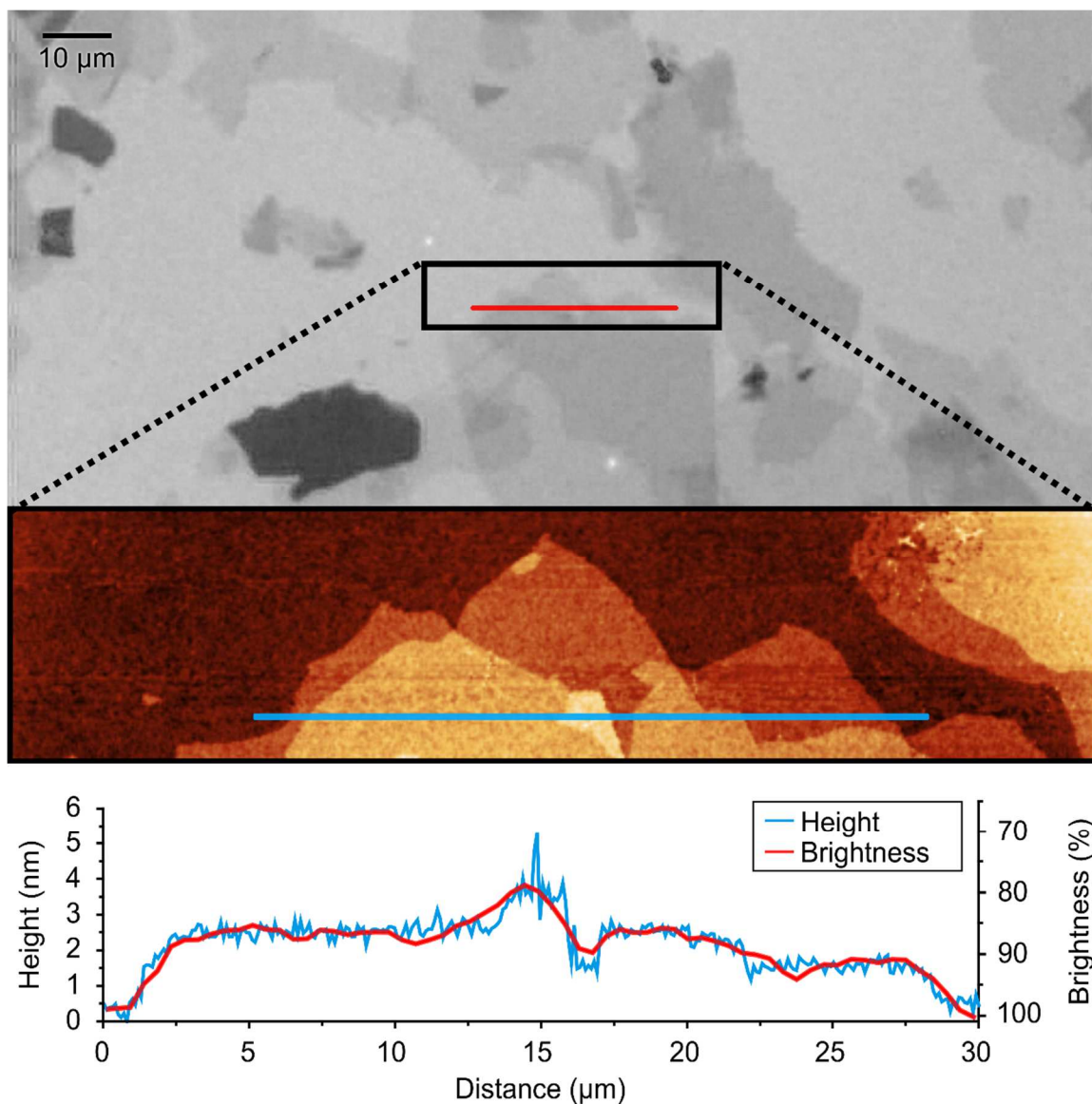
Figure 3.4: Co-located optical (top) and AFM (center) images of GO sheets on an SiO$_2$ substrate. Only the red channel of the optical image is shown. The bottom plot shows the optical brightness profile (red, right axis) and AFM height profile (blue, left axis) of the 30 μm line indicated in each image. The optical image shown used a higher concentration than those samples used for characterization. This allows for more visible surface features on the sample, which are used as references for the co-location on the AFM.
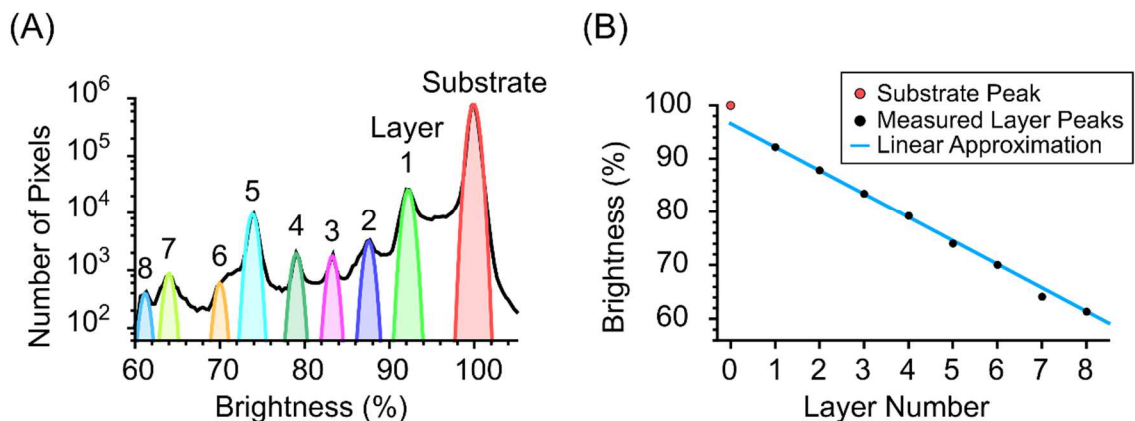
Figure 3.5: (A) The histogram from Figure 3.2J, with the peaks corresponding to the substrate and different layer number brightness values highlighted. (B) A plot of the brightness values from each peak (black circles) as a function of layer number, showing the linear relationship between them. Note that the substrate peak (red circle) does not follow this linear trend.

After the processing steps have been completed for a given image, it is converted from the brightness values captured by the camera to height values. For some materials, a function relating the two can be acquired from the literature (e.g. graphene[99]). If the material being examined does not have a function available, it can be obtained experimentally by acquiring co-located optical and AFM images (Figure 3.4). The brightness values that correlate to a given layer thickness can be determined from these and a function explicitly stating the correlation is generated (Figure 3.5). Depending on the combination of material makeup, thickness of the sheets being examined, substrate, and wavelength of light used, this function can be non-linear, and even non-monotonic, i.e. contrast inversion may be observed at some layer numbers, such that the both the layer immediately preceding and the one following such a layer are brighter (or darker) than it.[91,93] Often, choosing another combination of wavelength or substrate can keep the function predominantly linear. If such a choice is not available, we developed a macro for ImageJ,[84] the open source, NIH-developed image processing software used for the execution of much of the technique, which can

compensate for this issue. Not correcting for this issue could otherwise cause regions of a flake that are particularly thick to be incorrectly identified as thin, causing diminished accuracy (Figure 3.6). The macro identifies local maxima within a flake (Figure 3.6B), determines the region around each where the brightness continues to fall (Figure 3.6C), and then inverts the brightness values within this region about the value at which inversion occurs (Figure 3.6D). Once the macro is completed, the above-described brightness/layer correlation function can be determined for the corrected image.
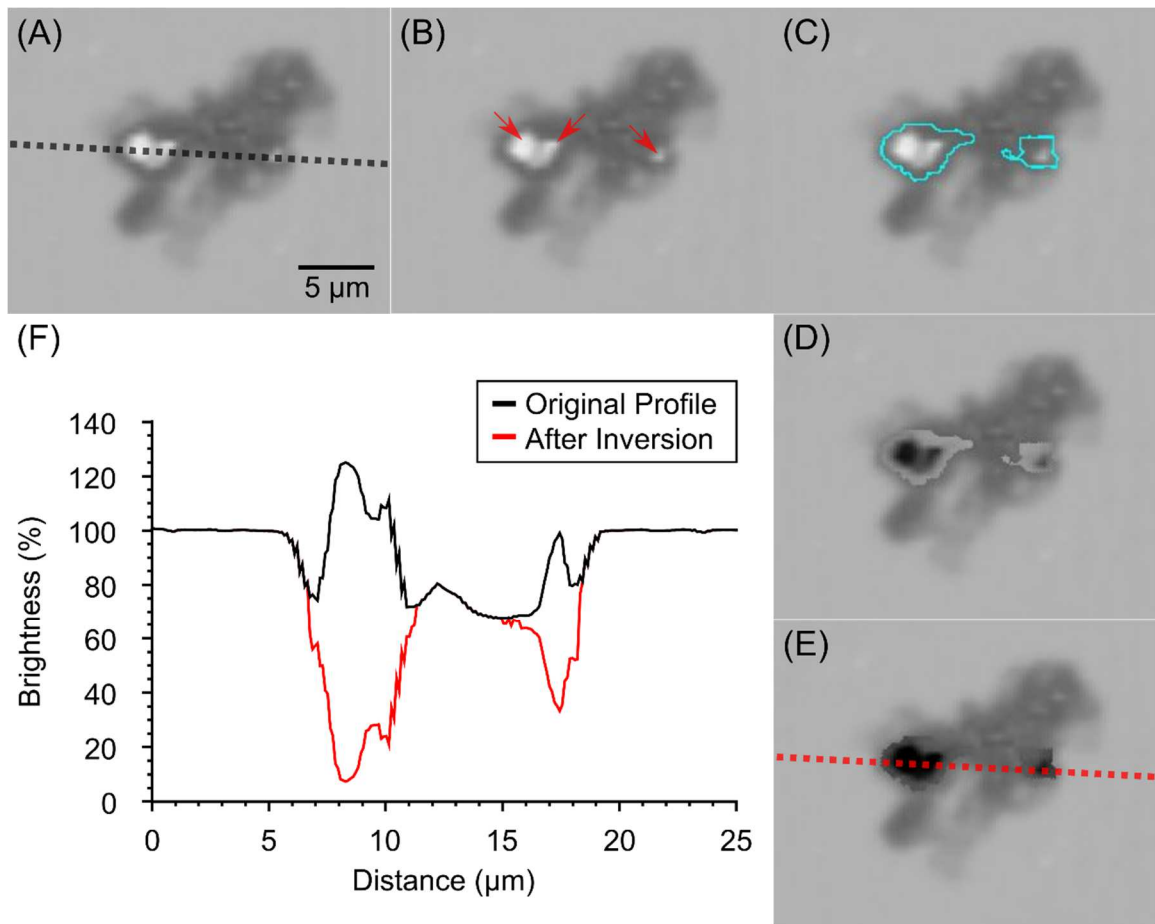
Figure 3.6: Steps of the inversion macro. (A) Original flake image, (B) local maxima (red arrows), (C) region to be inverted, (D) after initial inversion, (E) after regions have been realigned with surronding area. (F) Plot of optical profiles from (A) and (E) showing return to montonic behavior.

This function is then applied to the image, converting the brightness value for each pixel to the equivalent average layer number. Standard automated particle analysis routines can then be applied to the finalized image, giving quantitative values for both the lateral dimensions and thickness of each sheet. This data can then be analyzed for information on the distribution of these parameters within the population examined.

3.3. Emulsion Separation Results

We used this method to examine the effects of the emulsion process (described in Chapter 1e – Emulsions of 2D Materials) by characterizing the morphological composition of GO samples taken from both the water portion of the emulsion (GOw, Figure 3.7) and the chloroform portion of the emulsion (GOe, Figure 3.8), along with a sample of the original material before it underwent fractionation (GO, Figure 3.9). While differences between the samples are apparent visually, our method allowed us to directly track the changes in flake thickness and size. Previously information on oxidation extent and conductivity had been available, but not morphology.[70] The results of this analysis are shown in Figure 3.10 as histograms for both average layer number (A,B) and sheet area (C,D), each as a function of both cumulative percentage surface area (A,C) and the number of flakes (B,D).
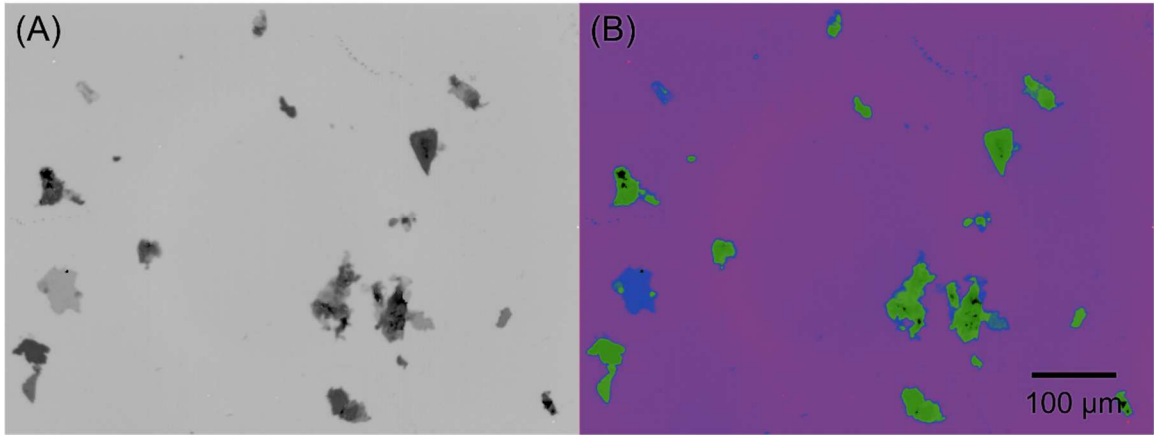
Figure 3.7: Sample optical image of the GOw sample in grayscale (A) and false color (B).
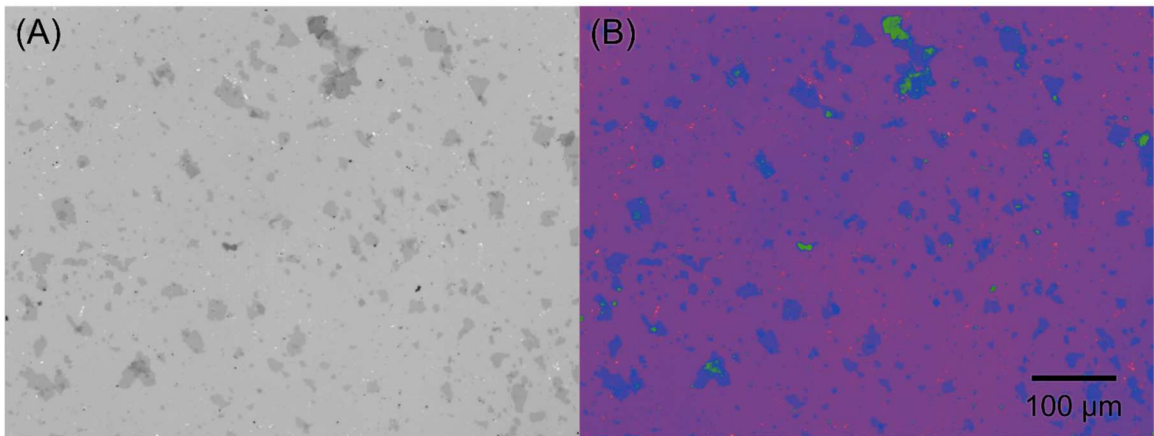
Figure 3.8: Sample optical image of the GOe sample in grayscale (A) and false color (B).
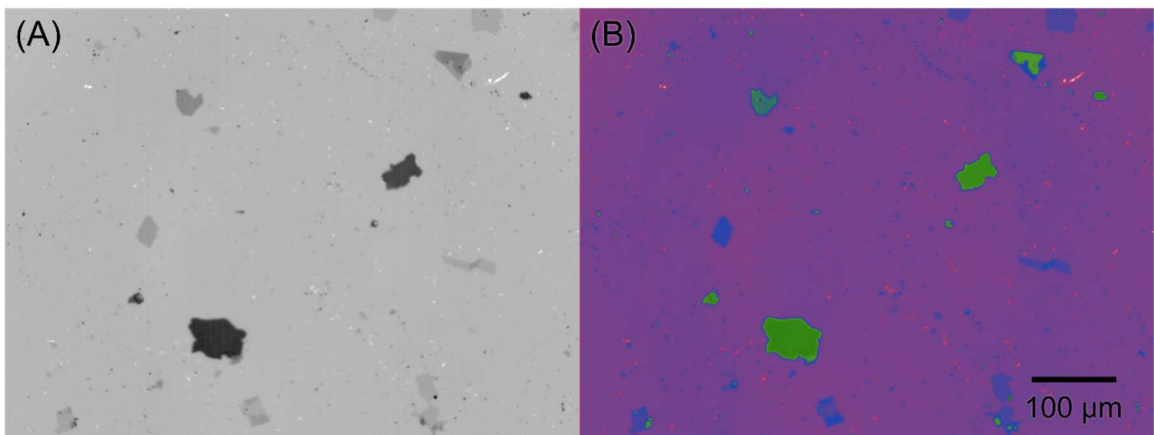
Figure 3.9: Sample optical image of the GO sample in grayscale (A) and false color (B).
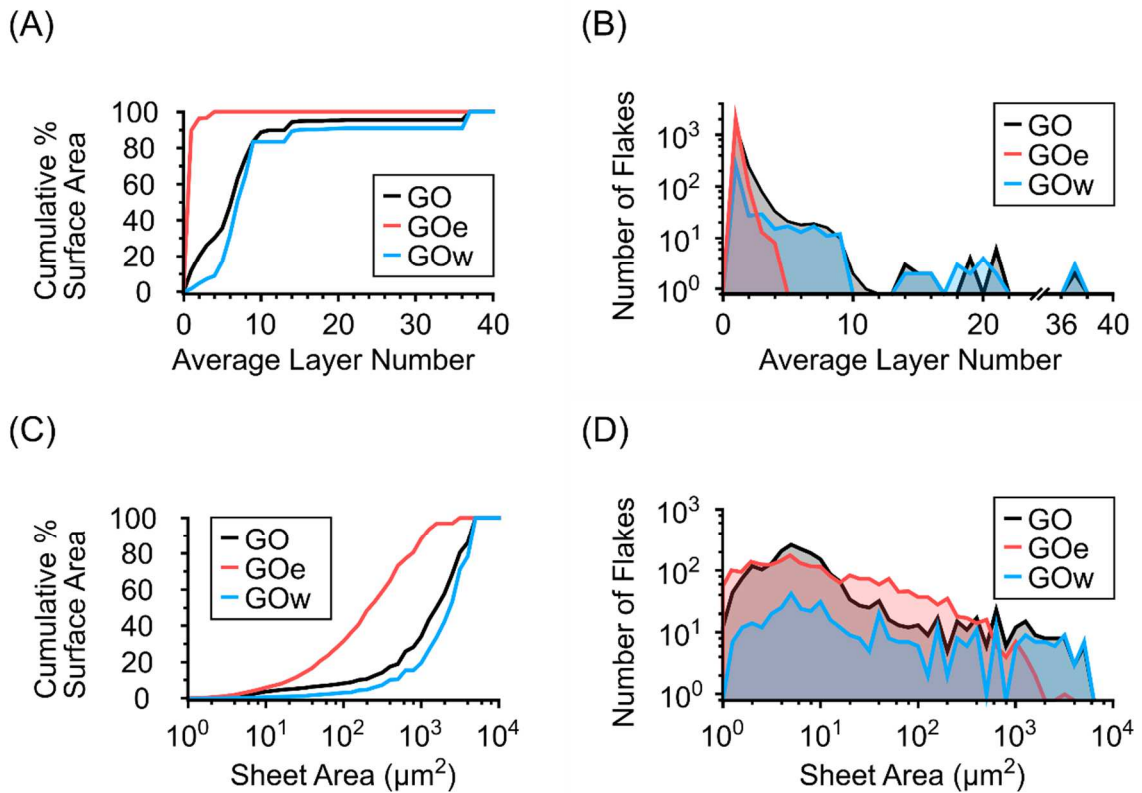
Figure 3.10: Histograms showing cumulative percentage of surface area (A) and number of flakes (B) by average layer number. Cumulative percentage surface area (C) and number of flakes (D) by sheet area (μm^2). Binning by sheet area is logarithmic, with ten bins per decade.

From these plots we can immediately discern that there is significant diversion in the size and thickness distributions of the material after undergoing the emulsion process. In Figure 3.10A, nearly 90% of the material extracted from the GOe fraction by area has an average layer number of one, and no sheets had an average layer number greater than four. The material from the water portion (GOw), by comparison, has only 10% of its sheets with an average layer number of four or less. The original GO shows a layer distribution similar to that of GOw after the four layer mark, but with a larger portion of low-layer material, with 30% of the surface area coming from flakes with an average layer number less than four.

This is also apparent in looking at the number of flakes of each thickness (Figure 3.10B). Here GOe has a large number of flakes of average layer number one, but drops off sharply thereafter, whereas GOw and GO both show a more gradual decline, and closely match after the four layer mark. Comparing Figure 3.10A and B also demonstrates the impact of high average layer number flakes, which are fewer in number but tend to contain a larger portion of the total surface area.

This is further demonstrated in Figure 3.10C, where we see that the GOe sample has a much larger portion of smaller flakes as a percentage of total surface area than either GOw or the original GO. Note that both Figure 3.10C and D use a logarithmic scale for the x-axis, with ten bins per decade equally spaced on a log scale. GOe has about 90% of the total flake surface area come from flakes with areas less than one thousand μm^2, compared with approximately 25% for GO and 15% for GOw.

All samples had the largest number of flakes with areas around fifty μm^2. The GO samples showed a stronger peak in this region compared to GOe and GOw, which were both more generally more evenly distributed across the range of sizes, though all samples dropped off as flake size increased. The largest flakes in the GOe sample were smaller than those in the other two samples, with none more than two thousand μm^2 in size. In contrast, both GOw and GO extended to nearly six thousand μm^2 for the largest flakes in each sample.

3.4. Discussion

From these results we can see that the fractionation method is selective with regards to both lateral sheet size and sheet thickness. Sheets taken from the emulsion portion are smaller and thinner on average, significantly so as compared to the water portion of the emulsion and the original source GO material.

Beyond the strictly morphological differences between the samples we also gain insight into the operating mechanism of the emulsion process. There is a strong correlation between the GO and GOw samples, with corresponding population spikes in layer number (between 12 and 14, 18 and 21, and at 37 layers) and sheet area (e.g. at 400, 1500, and 6000 μm^2). This demonstrates that this kind of material was overrepresented in the initial sample and remains unchanged in the water portion of the emulsion. However, these spikes were not present in the GOe sample. This indicates that the flakes from this portion of the emulsion have changed their relative size and thickness distributions in a way not experienced by those in the water portion.

For further insight, the samples were also analysed using XRD by our collaborators at the University of Connecticut. As typical for samples produced by oxidizing graphite, XRD spectra of the GO fractions showed two peaks (Figure 3.11A). The peak around $2\theta = 26°$ corresponds to a separation of about 0.34 nm, representing the original stacking of graphitic sheets prior to oxidation. The peak at $2\theta = 10°–13.5°$ represents the increase in spacing between the sheets to 0.7–0.9 nm caused by the addition of oxygen functional groups during the reaction. To quantify to what degree the material exhibited the increased spacing due to oxidation, we calculated an XRD r value based on the formula[70] $r = A_{GO}/(A_{GO} + A_G)$, where A_G is the area of the G peak assigned to graphite stacking, and A_{GO} the area of the GO peak assigned to GO stacking. Table 3.1 lists the XRD r values for each of the three samples. There is a clear order in the r value, with GOw > GO > GOe, which is in line with published results using this fractionation method.[70] This ordering is similar to that found for sheet size and average layer thickness using the optical method, with a larger portion of oxidized material corresponding to a greater percentage of large or many layer sheets. This correlation illuminated the underlying mechanism of the fractionation process. The GOe fraction

has undergone a significant degree of exfoliation as compared to the GOw fraction. In hindsight this is not surprising, as the emulsion is stabilized by the spreading (exfoliation) of sheets at the oil/water interface.[10] This means that not only are the less oxidized (less hydrophilic) sheets found at the oil/water interface, but they are exfoliated at the interface as well. Thus, the degree of oxidation, as determined by the value of r, only partially describes the state of the GO. This additional information would have remained unobserved without the rapid morphological characterization made possible by the optical method outlined here.
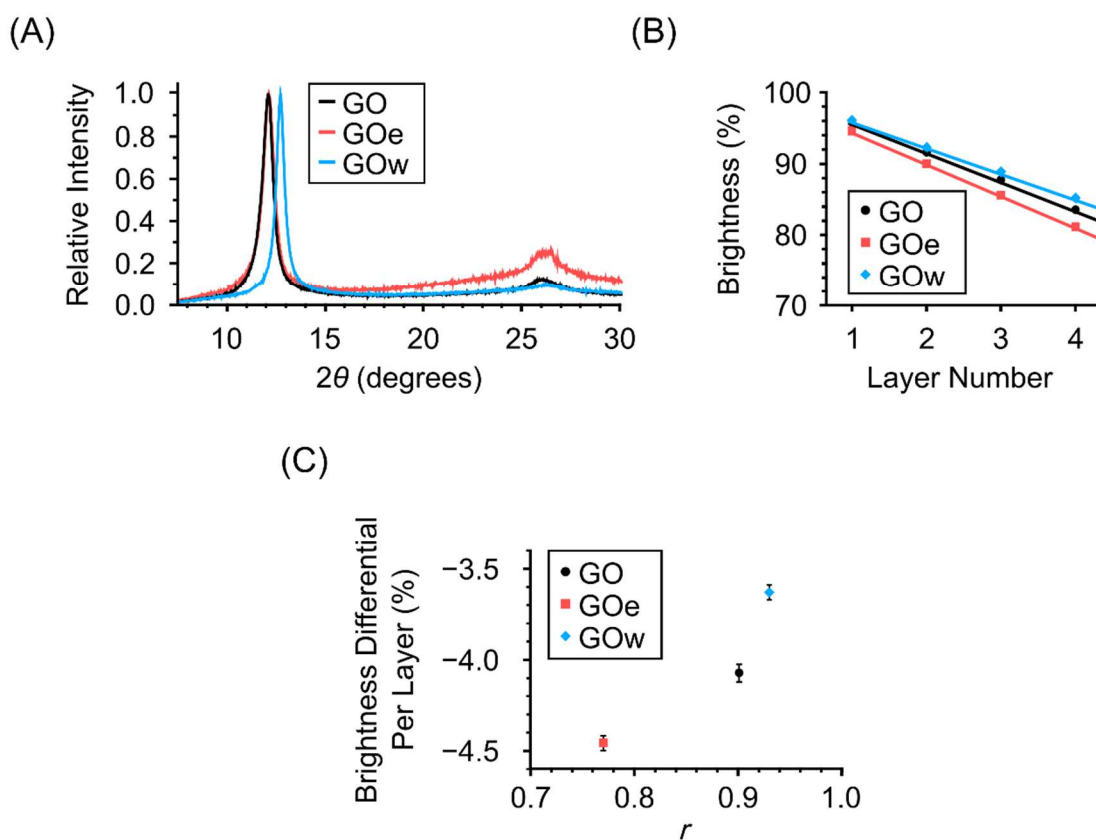
Figure 3.11: (A) XRD spectra of the fractionated samples. (B) Brightness values of the first four layers for each sample with linear trendlines for each. (C) Slopes of the linear trendlines from (B) plotted as a function of the XRD r value.

Sample Name	XRD *r* value
GOw	0.932 ± 0.005
GO	0.898 ± 0.004
GOe	0.768 ± 0.016

Table 0.2: Calculated XRD *r* values for each sample.

It is interesting to compare this correlation between larger sheet dimensions and higher oxidation levels with the work of Dimiev and Tour, who showed that the oxidation of graphite into graphite oxide during the Hummers method is controlled by the diffusion rate of the oxidizing agent.[100] This could possibly lead one to expect that larger sheets would be less oxidized than smaller ones. At first glance, our results appear to contradict this expectation, although we do not believe this is the case. Rather, the more hydrophobic, nearly un-oxidized graphite in the GO sample went to the oil/water interface, which has been shown to drive exfoliation.[70] The more hydrophilic, highly oxidized material, in contrast, remained in the aqueous phase and thus did not exfoliate and so remained larger and more stacked on average. This was seen in the difference in the distribution of sheets with an average layer number less than four in Figure 3.10A.

It has been shown that oxidation of graphene changes its optical properties,[101,102] including changes in the optical contrast between individual sheets and the substrate.[95] Consequently, we were interested whether different degrees of oxidation found in the different kinds of material (GOw, GO, GOe) would lead to a noticeable difference in the brightness-vs-thickness curves for different materials. Therefore, a linear fit was applied to the brightness values for the first four layers for each sample (Figure 3.11B). The brightness change per layer was determined from the slope of this fit for each material and showed a surprisingly strong and significant change as a function of the *r* value (Figure 3.11C). The difference in slope between the three materials was large

compared to the corresponding error of the fit (shown as error bar). The slope of GO, (−4.08 ± 0.04)%, was greater compared to GOe, (−4.46 ± 0.03)%, and less than GOw, (−3.63 ± 0.04)%. As the change in brightness for a given nanosheet layer number is dependent on the dielectric constant of the material,[93] our simple method provides surprisingly powerful way to assess optical properties of a population; in principle, one could calculate the optical constants of the material using this method.

3.5. Conclusion

With the development of this technique, we were able to offer a new tool to the scientific community, one that allows for the rapid, simultaneous characterization of the thickness and lateral area of thousands of nanosheets. Using only low-magnification optical microscopy, commercially available substrates, and free, open source software, we were able to provide information on samples that would have previously required the use of expensive, specialized equipment to obtain, and could do so in one hundredth of the time. Beyond this, the method gives a method for simultaneously assessing the oxidation state and optical constants of a material with no additional processing.

Through the application of the technique to our emulsion-fractionated GO samples, we were able to precisely determine the morphological differences between them. This illuminated the nature of the process and demonstrated that the sheets are indeed being exfoliated at the interface as previously suspected. Without our technique, this information would not have been available, and our understanding of the behavior of nanosheets at the oil/water interface limited.

Further work with these systems must involve characterization of other samples, both different nanosheet materials (graphene, hBN, TMDs, etc.), varying combinations of

liquids in the emulsions, and further exploration of the effects of repeated bouts of fractionation. The optical characterization technique is also useful for work outside of the emulsion process, as the substrates used here are also commonly used with other techniques, such as growing nanosheets through chemical vapor deposition. This process could allow automated in-situ tracking of sheet growth or changes in optical constants from a variety of causes, e.g. mechanical strain due to lattice mismatches or defects.

Chapter 4

Graphene Oxide Functionalized Probe

4.1. Introduction and Theory

In this chapter we directly investigate the behavior of 2D material at a liquid-liquid interface using AFM. Here, we used a colloidal probe and performed force spectroscopy measurements on bubbles of heptane pinned to a substrate in water (Figure 4.). We performed these measurements first with a bare silica probe, a second time after coating the probe with graphene oxide, and then a third time after the coating was reduced with UV, a process which produces a coating similar to graphene. These measurements provide both general insight into the behavior of 2D materials at this interface and specific insight into scaling the previously discussed processing technique for producing these materials up to a large scale while maintaining low cost. The custom graphene coated probe we developed also provides a new scientific tool to study the interactions between graphene and other materials. As graphene is notoriously difficult to isolate in large quantities for industrial use, this probe will provide

new insights into tailoring the surface interactions of this 2D material so that it can be utilized more widely.
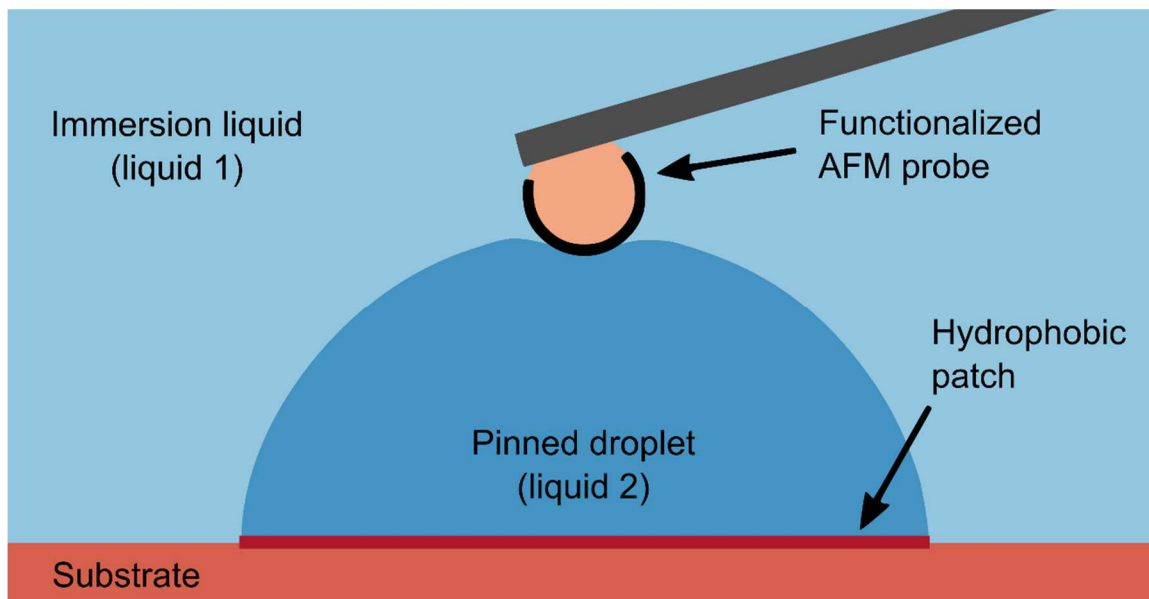
Figure 4.1: Diagram of the force spectroscopy experiments performed at the liquid-liquid interface. To perform the experiment, an AFM colloidal probe functionalized with GO or reduced GO is submerged in an immersion liquid (liquid 1) in an AFM liquid cell. Also submerged is an immiscible droplet of liquid 2, pinned to the surface of a patterned hydrophobic/hydrophilic substrate (dark red/light red). The functionalized AFM probe is approached toward the pinned droplet until it makes contact with the apex of the droplet. Then force curves are performed. Care is taken to prevent the probe puncturing the pinned droplet.

To understand the behavior seen in these experiments, we must first examine the factors that govern the behavior of a particle at an interface. Here we start by examining the interactions of two particles in contact and proceed in complexity from there, following the work of Israelachvili.[79]

In general, we can describe the interaction between two particles in contact as being proportional to some inherent property possessed by each particle, e.g. the mass m in a gravitational context or the dipole moment μ in dipole-dipole interactions. For two

objects A and B, we can write this value as *A* and *B* and therefore write the binding

energies, *W*, of these two objects in contact as

$$W_{AA} = -A^2, \ W_{BB} = -B^2, \ \text{or} \ W_{AB} = -AB \tag{4.13}$$

for two particles A in contact, two particles B in contact, or one of each type of particle,

respectively.
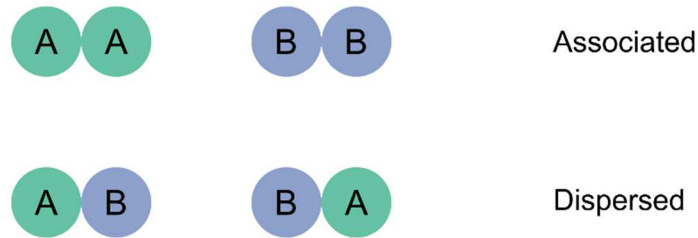
Figure 4.2: The potential configurations of two unlike particles A and B coming into contact in a mixture. The particles may remain in contact only with others of the same kind, and are called *associated* (top) or may freely contact with the other kind, and are called *dispersed* (bottom).

For a mixture of an equal number of particles A and B we can then consider the

energetic cost associated with particles attaching only to those of the same kind

("associated") or freely attaching to any particle, A or B ("dispersed") (Figure 4.2). This

can be written

$$\Delta W = W_{ass} - W_{disp} \tag{4.14a}$$

$$\Delta W = -A^2 - B^2 + 2AB \tag{4.(4.14b)}$$

$$\Delta W = -(A - B)^2 \tag{4.(4.14c)}$$

from which we see, as (*A* − *B*)² must always be positive, that $W_{disp} > W_{ass}$ and

association is generally energetically preferrable to dispersion.
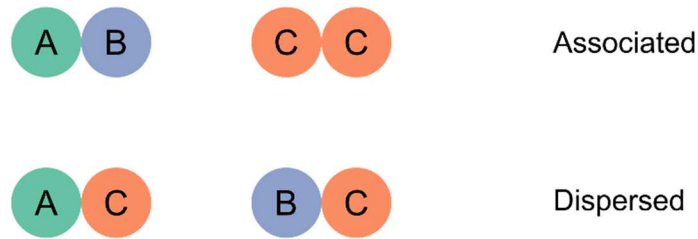
Figure 4.3: The potential configurations of two unlike particles A and B coming into contact in a solvent C. The particles may remain in contact only with other particles and are called *associated* (top) or may freely contact with the solvent and are called *dispersed* (bottom).

We can now introduce the effects of a medium to the relations between these particles, rather than interactions in a vacuum. Consider two dissimilar particles A and B coming together in a solvent C. Here we have again a choice between association and dispersion: either A and B may associate with one another, with C left to interact with itself, or A and B disperse and prefer to interact with C (Figure 4.3). The energetic cost here can be written as

$$\Delta W = W_{ass} - W_{disp} \tag{4.15a}$$

$$\Delta W = -AB - C^2 + AC + BC \tag{4.(4.15b)}$$

$$\Delta W = -(A - C)(B - C). \tag{4.(4.15c)}$$

This is distinct from the previous result in that it is possible for the energy of the system to be positive or negative, depending on whether the value for C is intermediate between A and B or not. If it is intermediate, then the result is positive, and the particles will repel one another, which was not possible previously.
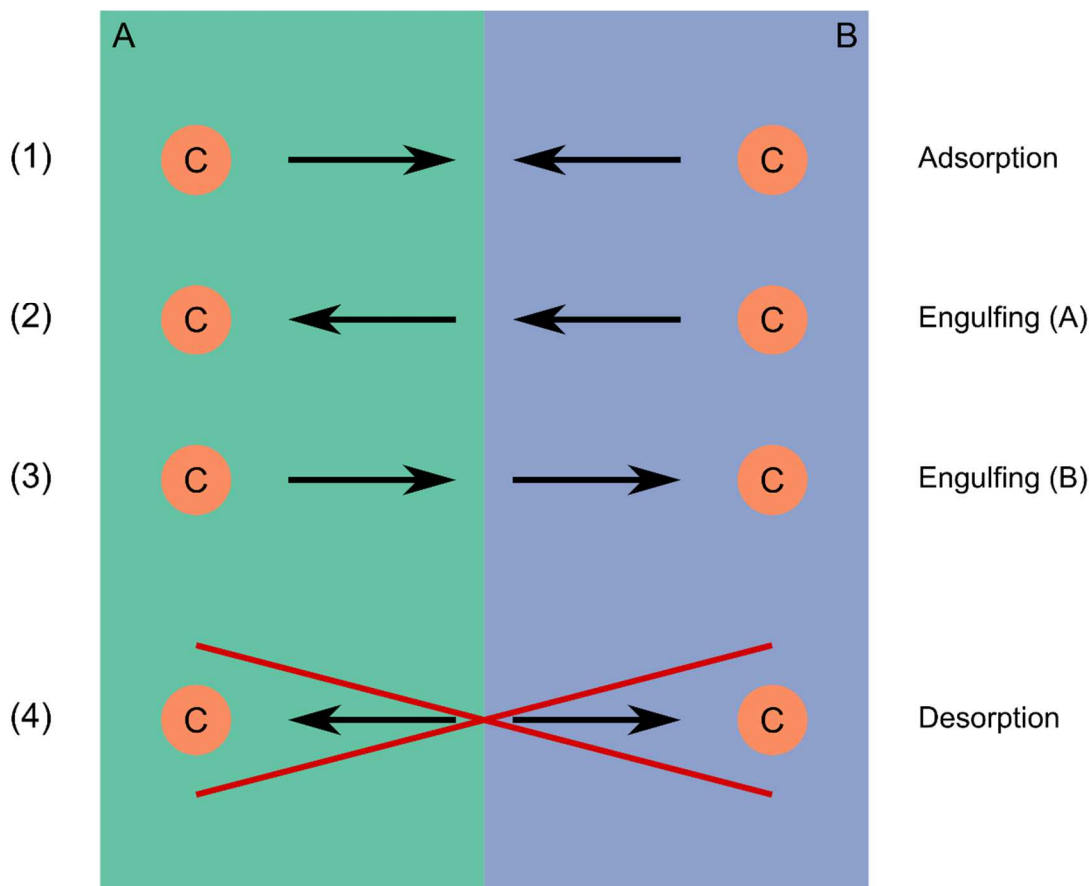
Figure 4.4: The potential behaviors of a particle near the interface of two immiscible liquids include (1) Adsorption of the particle to the interface between the liquids, (2) & (3) Engulfing of the particle as it moves from one liquid into the other, and (4) Desorption of the particle as it leaves the interface and moves into one of the two liquids. This last option is impossible as it would require the particle to be closer in surface energy to each of the solvents than the other, which it cannot be.

We can now examine the behavior of a particle near an interface between two immiscible liquids. For a particle C that lies near the interface between two liquids A and B, there are, effectively, two options for its behavior (Figure 4.4). One, the particle may be attracted to the interface, regardless of the side on which it exists ("Adsorption") (Figure 4.4 option 1). Or, two, the particle may be repelled on one side and attracted on the other side of the interface ("Engulfing") (Figure 4.4 options 2 and 3). While there would appear to be a third option, where the particle is repelled from

both sides of the interface ("Desorption") (Figure 4.4 option 4), this does not, in practice, happen, as will be explained shortly. Using (4.15c, we can write the energy of the system on each side of the interface:

$$\overrightarrow{\Delta W} = -(C-A)(B-A) \tag{4.16a}$$

$$\overleftarrow{\Delta W} = -(C-B)(A-B) \tag{4.(4.16b)}$$

We can then write the change in energy as the particle crosses the interface from right to left as:

$$\underset{tot}{\overleftarrow{\Delta W}} = \overleftarrow{\Delta W} - \overrightarrow{\Delta W} \tag{4.17a}$$

$$\underset{tot}{\overleftarrow{\Delta W}} = -(C-B)(A-B) + (C-A)(B-A) \tag{4.(4.17b)}$$

$$\underset{tot}{\overleftarrow{\Delta W}} = (A-C)^2 - (B-C)^2. \tag{4.(4.17c)}$$

$$\underset{tot}{\overleftarrow{\Delta W}} = \Delta W_{BC} - \Delta W_{AC}. \tag{4.(4.17d)}$$

From this, it becomes clear that if the surface energy of the particle is between that of both liquids (A<C<B or A>C>B), the particle will be adsorbed to the interface as the change in energy will be zero. Otherwise (A>B>C or A<C<B), the particle will be engulfed by the liquid which has a surface energy most different from that of the particle. As these are the only possible orderings, it is not possible for desorption to occur.

Additionally, we can make use of the relation between ΔW and the surface energy of an interface γ, as seen in Equation 1.1, to relate this interaction to the surface energy of the components of the system:

$$\overleftarrow{\underset{tot}{\Delta W}} \propto \gamma_{BC} - \gamma_{AC}. \tag{4.18}$$

From this, we can see that the interactions of a particle at an interface is driven by the relative values of the surface energies of the components, denoting them as of primary importance.

In addition to interactions at the interface we must also be cognizant of the fact that these force spectroscopy experiments are being performed on a deformable surface: a bubble. As such, the contact area between the probe and bubble surface change as a function of applied force. As the probe pushes into the bubble, the bubble will deform around the probe, leading to greater contact area. This complicates the standard methods for processing force curve data, which assume that the sample is rigid and non-deformable. Having the deformable surface makes determination of the initial contact point difficult. One such example is when a cantilever is undeflected but is already embedded in a deformable surface. In this instance, the standard indication that the probe has just reached the point of contact instead is given at a point well below the surface level. Accordingly, the precise tip-to-sample distance is not always known in these experiments. Additionally, the standard method for determining the optical lever sensitivity, i.e. the conversion between deflection as given in the direct output from the photodetector, in volts or amps, to that in standard units of distance, relies on the portion of the curve that occurs after contact, known as the constant compliance region. Here, it can be assumed that, since the surface does not deform, for each nanometer the piezo is extended the cantilever must deflect in the opposite direction. However, this assumption does not hold true for a deformable surface like a bubble. It is instead required to take separate calibration curves on a hard portion of the surrounding substrate and use the optical lever sensitivity from these to convert to

distance for the curves taken on the deformable surface. This provides a suitable method for determining the forces involved in these interactions and was the method of choice for this work. An iterative deconvolution method for extracting the interaction energy of such a system from a force curve on a deformable surface was given by Dagastine et al. in 2004.[103] This method, while an appealing avenue for future investigations into the system at hand, is beyond both the current preliminary stage of these experiments and the scope of this work.

4.2. Development and Method

The initial process in performing these experiments was developing each necessary component. We started by using a GO coated probe which was previously developed by a previous student in our lab, Laura Dickinson,[104] and used for measurements in air. This probe consists of a colloidal silica sphere that is functionalized with an amine layer to generate a positive surface charge and then immersed in a GO-in-water suspension. The negatively charged GO flakes experience a long-range attraction to the surface of the probe and then remain there stably after drying due to powerful, short-range van der Waals interactions. Before the probe could be used in our experiments, we needed to verify the stability of the GO coating, as it was initially deposited in an aqueous environment similar to the one our tests required. This verification came from a series of Raman spectra we took of the probe both before and after taking curves at our water-heptane interface. These confirmed the presence of graphene oxide, showing the signature D and G peaks at 1350 cm^{-1} and 1600 cm^{-1}, respectively, as seen in Figure 4.5.
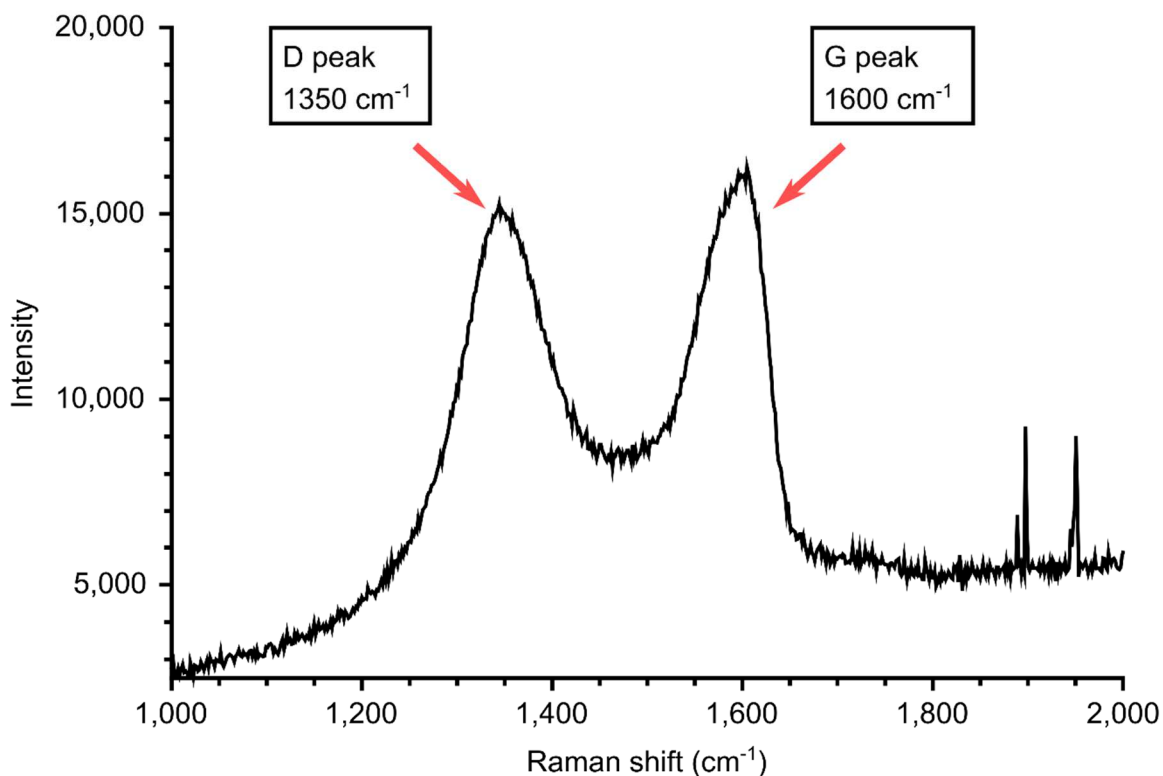
Figure 4.5: Raman spectra of the surface of the GO coated probe after performing force spectroscopy experiments in the AFM liquid cell. The curves prove that GO is present on the probe and, therefore, that the GO coating remains robustly attached to the probe surface even after submerging the probe in liquid and performing multiple force spectroscopy curves at the liquid-liquid interface.

Next, we needed to develop a graphene coated probe. For this, we decided to use the previously described GO coated probe and reduce the GO coating. Reduction here refers to a process that will remove many of the oxide groups from the GO, leaving the carbon–carbon bonds intact. This reduction step allows us to maintain the same cantilever (and spring constant), allowing for direct comparison between measurements despite having a different coating. Several mechanisms for reducing GO exist; the most common involve chemical treatments or heating.[105] Chemical treatments utilize strong reduction agents such as hydrazine[106–109] or metal hydrides.[110]

Thermal treatments can involve either rapid heating (up to 2000 °C/min)[111,112] or slower annealing in vacuum or inert atmospheres.[106,113] However, both of these methods would involve substantial risk of damage to the probe and cantilever. Instead, we reduced the coating by exposing it to high-intensity UV light, a process referred to as photo-reduction or flash redution.[114] This method works well for extremely thin samples (<1 μm), like our coating, but does not scale well to larger quantities. The viability of this method using our equipment was demonstrated on GO films that had been deposited onto glass slides and examined for the characteristic color change (from brown to black) seen in reduced GO. After these initial tests, placing the probes under UV for sixty seconds proved sufficient to completely change the interaction between probe and interface from the unreduced version of the probe, as will be seen shortly.
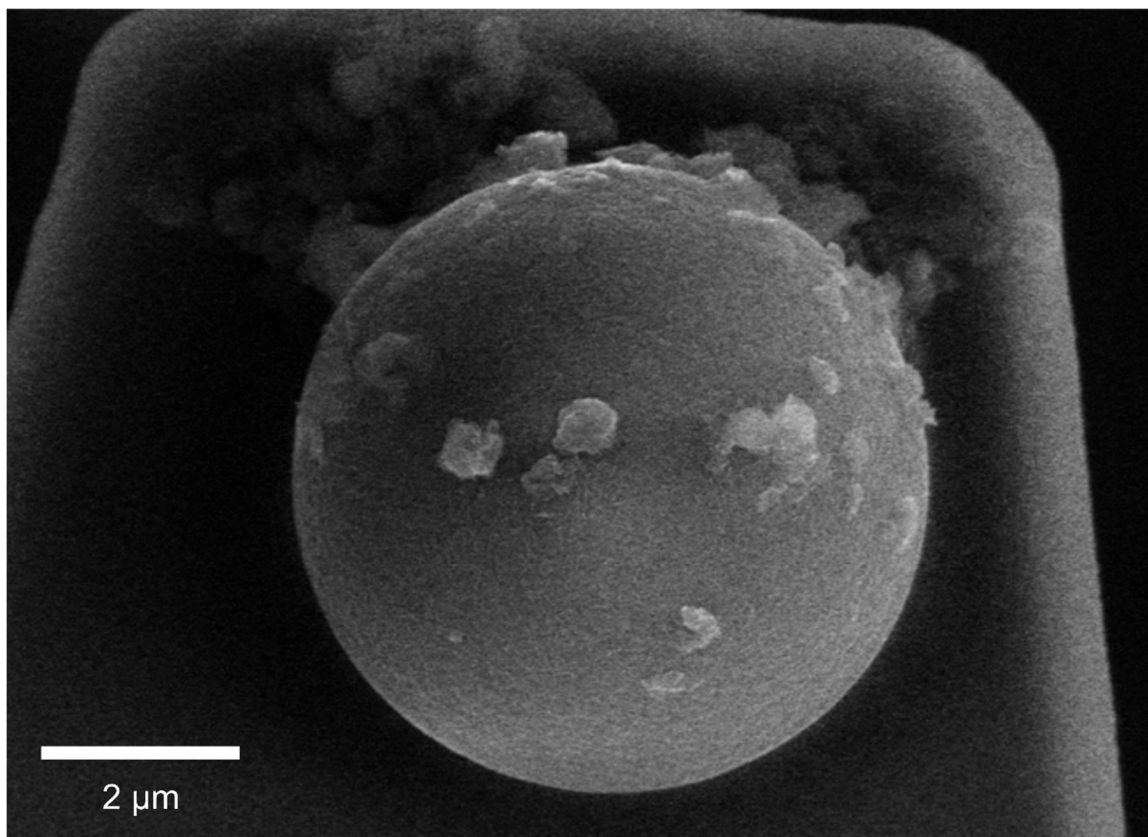
Figure 4.6: SEM image of an AFM colloidal probe after using a coating technique that involved forcing the probe through a graphene coated water bubble in heptane. The intention with this technique was that the graphene flakes would transfer from the heptane-water interface to the surface of the probe as the probe punctured the bubble. However, instead of forming a smooth coating, the graphene flakes restacked into the aggregate material shown on the surface of the colloidal probe. The flakes also tended to come off the probe when reintroduced to the heptane-water interface, possibly due to their small size.

We also tried directly coating the probe in graphene flakes by pushing a colloidal probe through a graphene stabilized bubble of water in heptane. This process did attach some aggregated layers of graphene, as seen in the SEM image in Figure 4.6, but the coating was not stable when re-introduced to the water/heptane interface used for testing and sloughed off. Ultimately, UV reduction proved the most effective method for producing a robust graphene-type coating for these experiments.

Finally, we needed a method for producing consistent, stable bubbles to provide our liquid/liquid interface. To this end, we developed a hydrophilic silicon substrate with a pattern of silanized, hydrophobic patches that allowed us to create a hexagonal grid of heptane bubbles under water. The starting point for this substrate is an ultra-clean silica wafer that had been cleaned via sonication in water with a surfactant, followed by additional sonication in picopure water, then followed by 30 minutes under high intensity UV and an additional 30 minutes in an ozone-rich environment. The first two steps remove any potential gross contaminants and the third removes any trace organic material left on the surface of the silicon. This leaves an extremely hydrophilic surface on which we create our pattern. The pattern itself is composed of a series of hexagonal silanized hydrophobic regions. We create these by placing a hexagonal TEM grid on top of the substrate (Figure 4.7A) and then depositing a molecularly thin layer of the silane using vapor deposition (Figure 4.7B). The grid functions as a mask, leaving the portions of the silicon underneath it unexposed to the silane, and therefore still hydrophilic. The grid is then removed (Figure 4.7C) via immersion in water with significant care taken to ensure that it does not slide over the newly formed regions, scratching or destroying them. This process results in a hydrophilic image of the grid on the newly-hydrophobic substrate (Figure 4.7D). The size and shape of the patches can be varied through the choice of the grid used as the template, for this work copper grids from Electron Microscopy Sciences with 200 μm spacing were used.
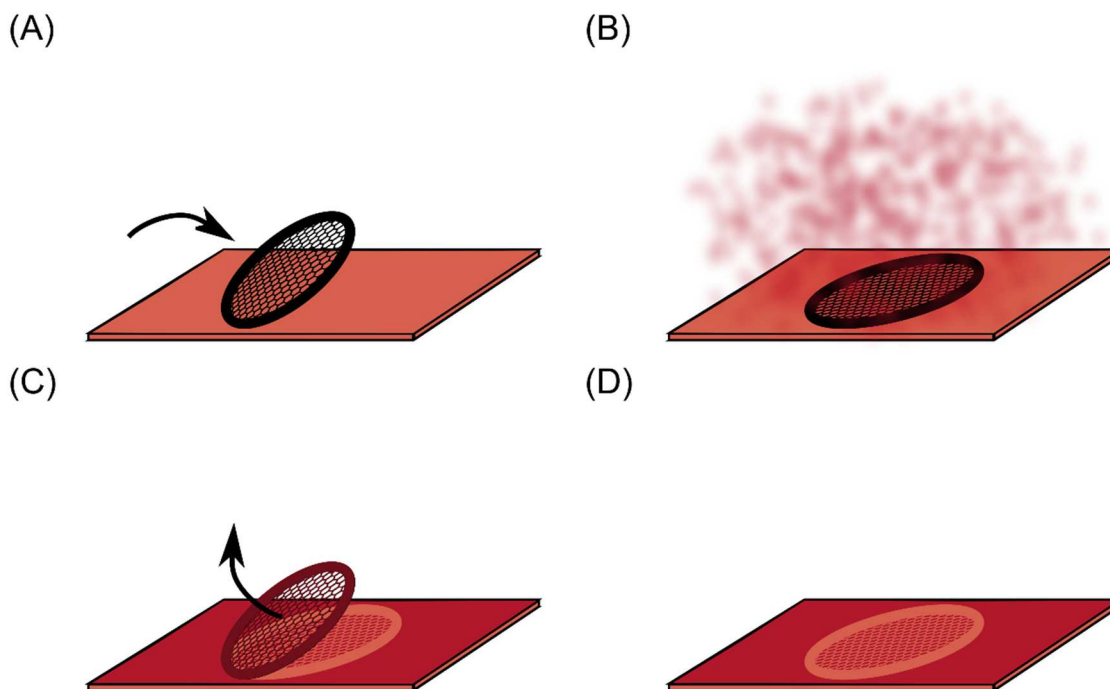
Figure 4.7: Diagram of the creation of the patterned hydrophilic/hydrophobic substrate. The process starts with a clean, hydrophilic silicon surface to which a hexagonal TEM grid was applied (A). The combined grid/silicon system was exposed to hydrophobic silane molecules via vapor deposition (B). After application, the TEM grid was carefully removed (C). Since the grid acted like a mask, shielding the area underneath from exposure to the silane molecule, a hydrophilic (light red)/hydrophobic (dark red) pattern is left on the surface (D).

After the pattern is in place, bubbles can be generated on the substrate by washing it with the chosen solvent (heptane in these experiments) immediately before pushing it into the filled liquid cell. While the pattern is not perfect, as the grid does not lay completely flat upon the substrate, regions are present where suitable grids of bubbles will be formed (Figure 4.8).
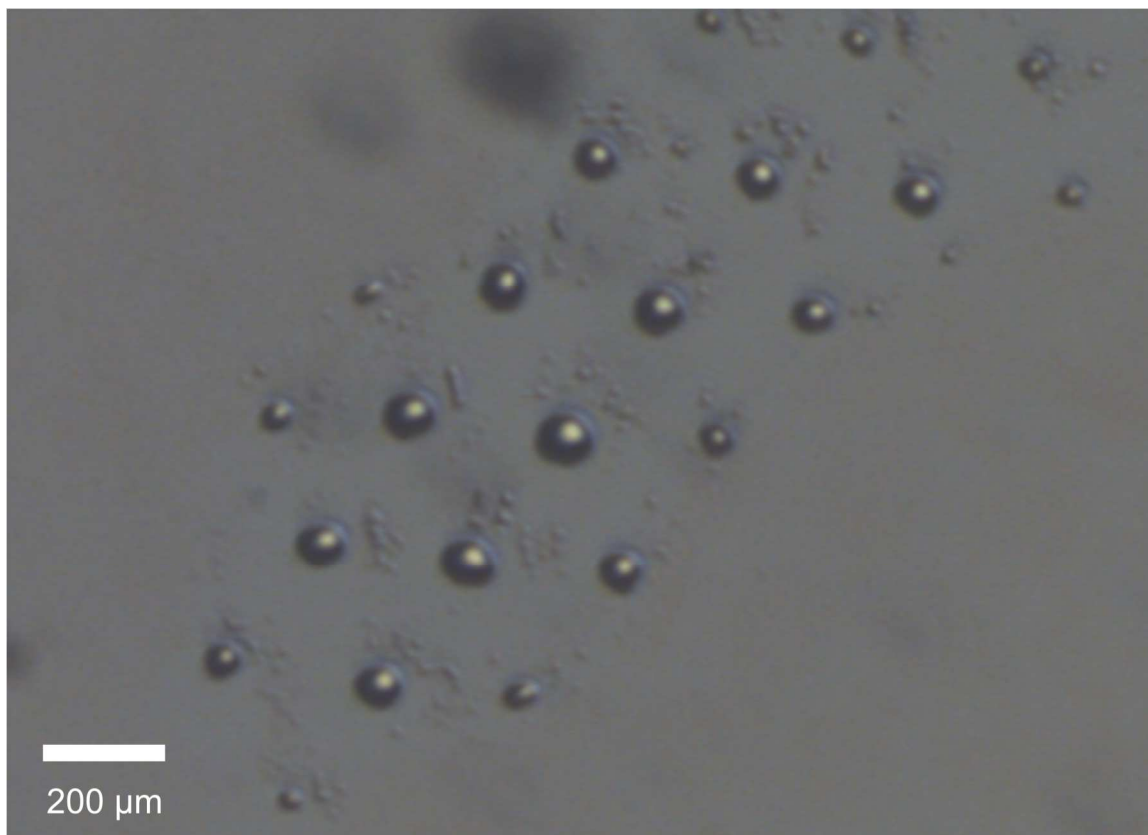
Figure 4.8: This optical image shows heptane bubbles attached to the patterned hydrophilic/hydrophobic substrate in water. The bubbles follow the hexagonal pattern of the TEM grid used to pattern the surface.

4.3. Bare Probe Results

The initial rounds of measurements were carried out with a bare silica sphere probe on a bubble of heptane in water to provide a set control data before introducing the probe coatings. Of these preliminary experiments, the curve below in Figure 4.9 is representative of the behavior of the interactions. During the approach portion of this sample curve (blue) we observe a sudden snap on of 5 nN at 1 μm piezo extension from zero. This snap on upon approach occurred frequently in these curves, but with variation in magnitude of force. As we retracted the probe from the bubble surface in this curve (red), we observed a 7 nN adhesion with a gradual pull-off that rises above

neutral then releases with a spike. We attribute this spike to the bubble budding off as it finally releases from the probe. This "spike" is common to all the measurements for this experiment where the end range of the release of the probe is visible in the curve. In some measurements this region is not visible. In these cases, the bubble did not release from the probe until after the piezo was fully retracted, when data collection had already stopped.
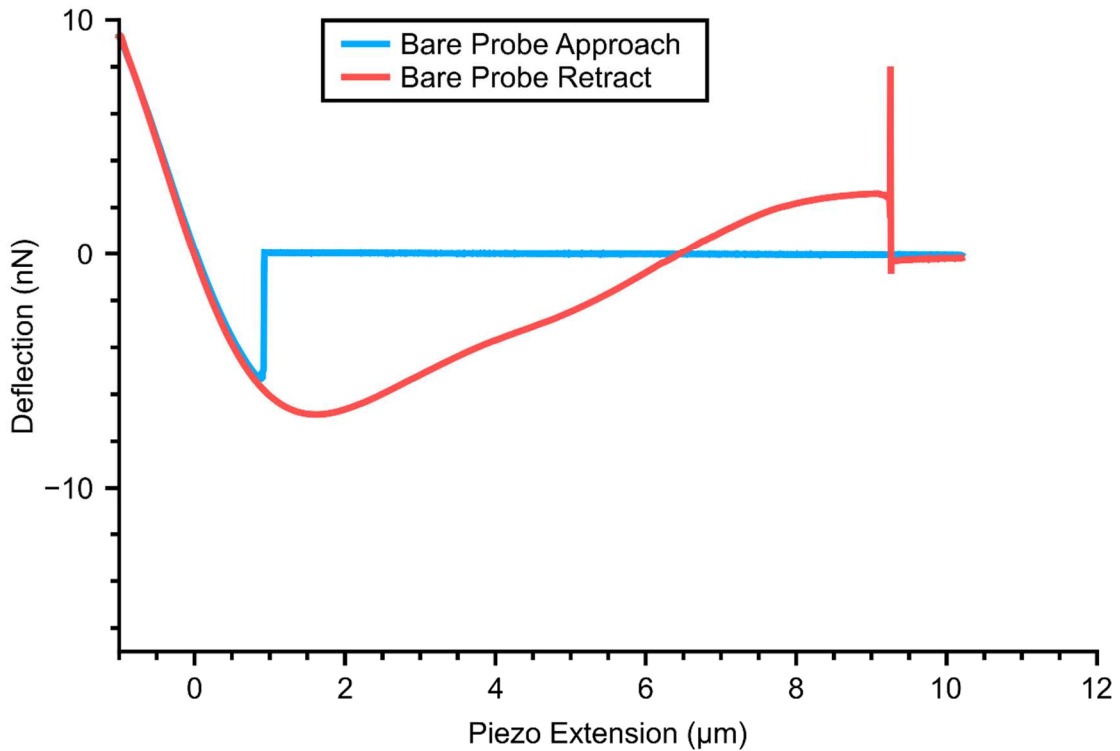
Figure 4.9: Bare silica probe on heptane bubble in water representative force spectroscopy curve. The blue curve indicates the path of approach of the probe to the bubble surface and is marked by a sudden snap on (probe suddenly deflects downward). The red curve indicates the retraction path of the probe away from the bubble surface. It shows a force of adhesion here that is larger compared to the snap on and it exhibits a sudden spike where the bubble finally releases the probe, causing the probe to rebound.

4.4. Graphene Oxide Coating Results

After performing experimental control measurements with the bare probe, we coated the same probe in GO and began to take measurements between the GO coated probe and a heptane bubble in water. As the representative curve below in Figure 4.10 indicates, these measurements did not indicate a snap on until 20 nm from the surface of the bubble (blue), indicating that there was no long-range attraction between probe and bubble surface. The retract portion of the curve shows a comparatively much larger 15 nN adhesion in addition to a gradual pull-off that rises above neutral.
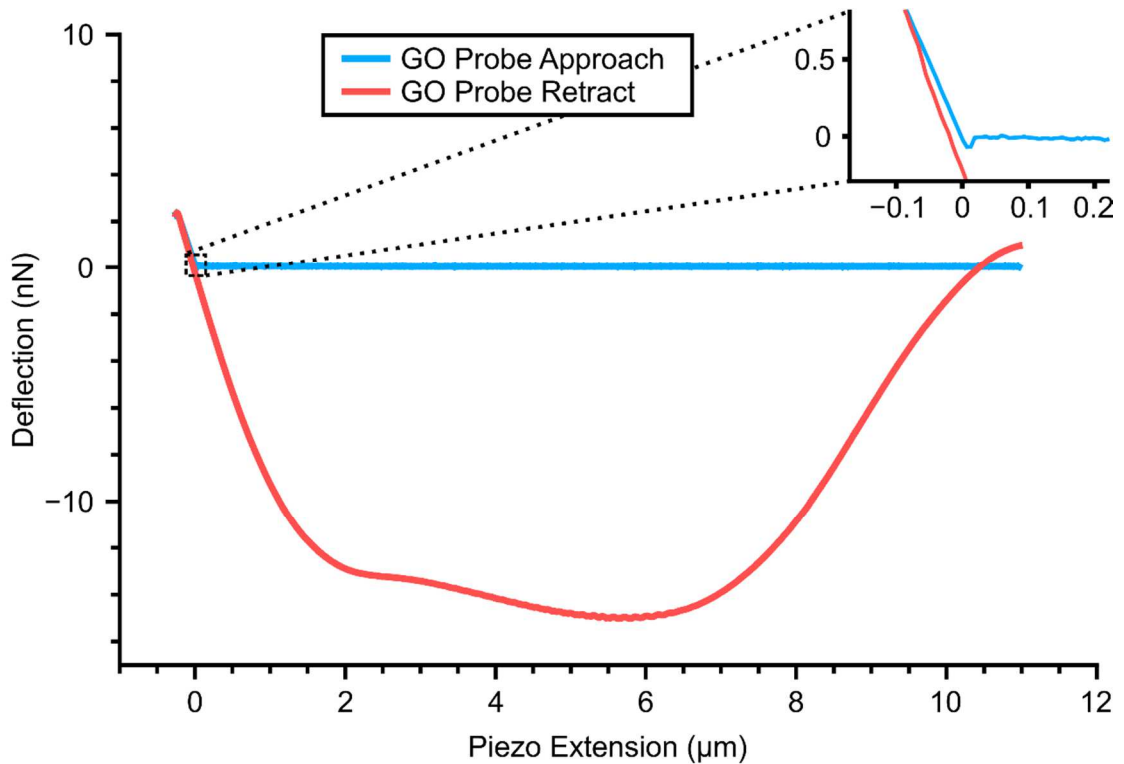
Figure 4.10: GO probe on heptane bubble in water representative force spectroscopy curves. The blue curve indicates the path of approach of the probe to the bubble surface and is marked by a snap on (probe suddenly deflects downward) that is very small and occurs at very short range compared to the bare silica sphere probe. This small snap on is indicated in the inset image of the zoomed in graph. The red curve indicates the path of retract of the probe away from the bubble surface. It shows a larger adhesive force than that seen in the adhesion of the bare silica probe.

4.5. Reduced Graphene Oxide Coating Results

After completing the GO coated probe measurements, we reduced the GO on the surface of the same probe. Using the same probe throughout all three experiments (bare, GO, and reduced GO) allows for direct comparison among the measurements because the probe had the exact same radius of curvature and its cantilever had the same stiffness. Using this reduced GO coated probe we performed measurements on a heptane bubble in water. As the representative curve below in Figure 4.11 demonstrates, we observed a large snap on force (here 12 nN at 2 µm). As we retracted the probe, we observed adhesion (14.5 nN in this example) and a gradual pull-off that rises above neutral.
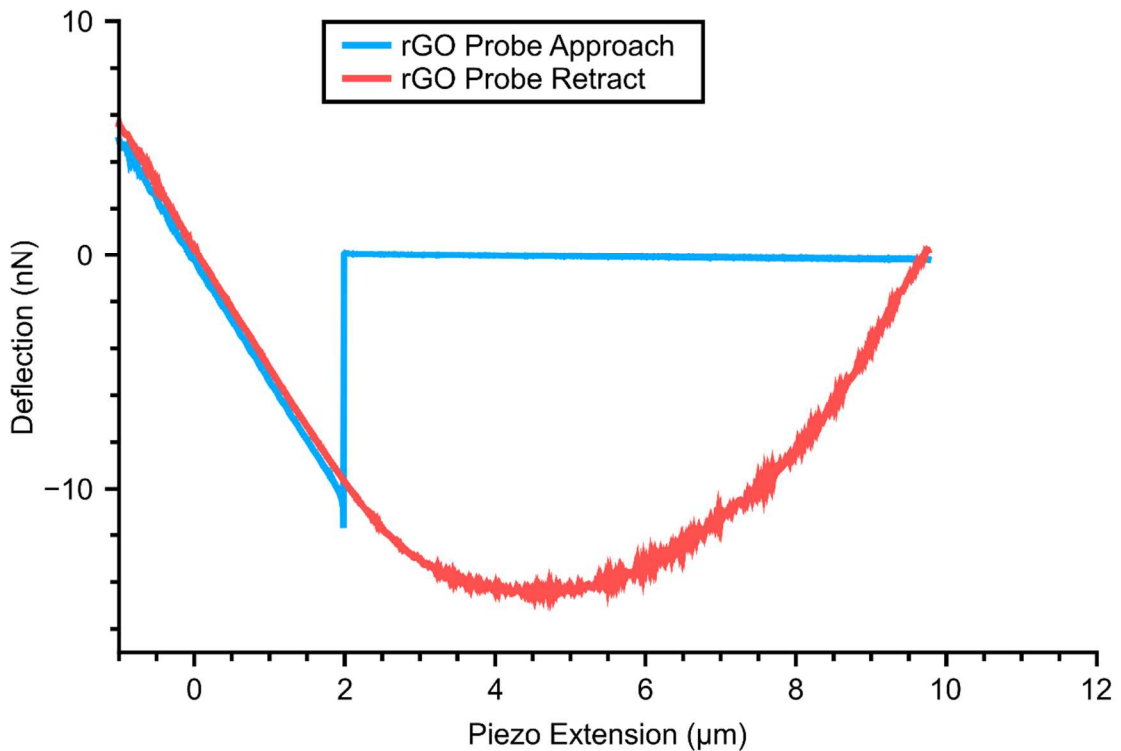
Figure 4.11: Reduced GO probe on heptane bubble in water representative force spectroscopy curves. The blue curve indicates the path of approach of the probe to the bubble surface and is marked by a sudden snap on (probe suddenly deflects downward). This snap on is larger and occurs at a greater distance than the one seen in both the bare silica probe and GO probe.

The red curve indicates the path of retract of the probe away from the bubble surface. It shows a similar adhesion force magnitude to that seen with the GO probe.

4.6. Discussion

For the bare probe experiment, we observe electrostatic long-range attraction. We attribute this sudden snap on to electrostatic forces because van der Waals forces are not expected to be present at this magnitude of force so far from the surface of a material. However, we would typically expect electrostatic forces in liquid to exhibit a more gradual exponential distance dependent trend (proportional to r^2), rather than a more sudden snap on, which is typical of van der Waals forces (proportional to r^6). Further analysis of the samples does not yield a solution to this perplexing trend. Why does the silica of the bare probe exhibit such an attraction for a heptane bubble? If it were in air, we might assume that the high surface energy of silica could result in a buildup of electrostatic charges on the surface. However, in water (a polar liquid) these excess charges should disperse.

The adhesion of the probe to the liquid-liquid interface in this experiment shows that the strong attraction observed at a distance is comparable when the probe is in contact. Both the magnitude of the force in the snap on and pull off are similar. Additionally, the strong adhesion is shown in the "spike" which occurs as the bubble deforms upward with the retracting probe before suddenly releasing it, so the probe recoils in an oscillatory behavior. Another explanation for this spike and the probe's behavior is that, after coming into contact with the heptane bubble, the heptane wets the surface of the probe, partially "bleeding" the bubble as the heptane moves along the surface of the probe (and potentially the cantilever). Since both water and heptane appear clear in the optical microscope of the AFM, and the amounts lost would be at most a few

picoliters, a small amount of heptane lost this way would not be readily apparent. However, if that excess heptane released from the surface of the probe during retraction and floated to the surface, its movement might cause the spike in the force curves.

In contrast to the bare probe, the GO probe shows no long-range (micron-scale) attraction to a heptane bubble, only short-range (nanometer-scale) van der Waals attraction. GO suspends in water due to the functional groups on its surface, which neither the silica nor RGO coating will do. This leads the GO probe not to be attracted to the heptane bubble, but to instead prefer the surrounding water molecules.

In terms of the retract curves, the GO probe shows strong adhesion, typically stronger than the bare probe. This shows that the GO probe has a preference for the interface as opposed to either the water or heptane.

In its approach curves, the rGO probe showed stronger long-range attraction than any of the other probe types. Similar to the bare probe, this attraction was also a sudden snap on at a distance that would typically be associated with electrostatic interactions. This result is intriguing because rGO is hydrophobic, does not suspend in water, and should have a slight preference for the heptane side of the interface. It is important to note that although hydrophobic surfaces can obtain excess electrostatic charges, this excess charge should dissipate in water. Therefore, it cannot drive this interaction. The exact mechanism behind this long-range attraction requires further study, but this experimental technique is capable of pursuing such a line of inquiry in the future.

In its retract curves, the rGO probe showed a strong adhesion which again indicates a preference for the interface over the two liquids. The magnitude of this adhesion was

closer to that of the GO coated probe than the bare probe, showing a similar interaction between the two coatings.

4.7. Conclusion

In these experiments, we explored the interaction between two varieties of 2D materials, GO and reduced GO, with a liquid-liquid interface using force spectroscopy with a functionalized probe. The results demonstrate significant differences both between the different probes and as compared to a control probe consisting only of silica. Both functionalized probes demonstrated strong adhesion to the interface, but the GO probe did not show any long-range attraction despite this being quite strong for the reduced GO probe. This demonstrates the feasibility of measuring these interactions using our system and provides a roadmap for better understanding the emulsion system and 2D surfactant behavior.

Next steps for these experiments should include deeper investigation of the impact of the reduction process. By varying the length of the exposure to the UV lamp and tracking the resulting surface changes via Raman spectroscopy and imaging techniques, either SEM or AFM, it will be possible to better understand the source of the long-range interaction between the probe and interface. Raman spectroscopy will provide quantitative data on the portion of oxide groups remaining on the coating, while SEM and AFM imaging would show any significant changes in topography such as jutting points which are known to have stronger van der Waals interactions than flat surfaces. Additional materials could also be used to functionalize the probes. We remain hopeful with regards to the viability of the coating method demonstrated in Figure 4.6. Obtaining samples with multi-micron sheet size (rather than the sub-micron available for use here) could improve adhesion between the material and the probe

surface, limiting material loss at the interface and potentially allowing for coatings with any of the 2D materials. Investigating different liquids would also be of great help in improving the large-scale efficiency of the emulsion process.

Chapter 5

Oil Functionalized Probe

5.1. Introduction

Interfacial interactions in oil/water systems are not restricted to GO, graphene, hBN, and TMDs. Of global importance, petroleum exploration and recovery also hinge on such interactions. Within the depths of an oil reservoir, oil adheres to mineral surfaces,[115–117] many coated in microscopic clay platelets, comingled with salt brine. The surface of these 2D platelets is also an interface between these two immiscible liquids. Here, rather than optimizing for attraction to the interface, finding methods to ensure complete water wetting of these platelets is of primary importance. This is especially important as oil recovery is immensely inefficient, leaving behind up to 70% of the oil behind. Multiple factors impact this percentage, including the composition of the injection liquids used to force the oil out of the reservoir[118–120] and the varying components of the mineral surfaces and the oil itself.[116,121–126] This search is further hindered by the high temperatures and pressures that exist in these reservoirs as these

variables can significantly impact the surface chemistry and interactions between components.[127–130]
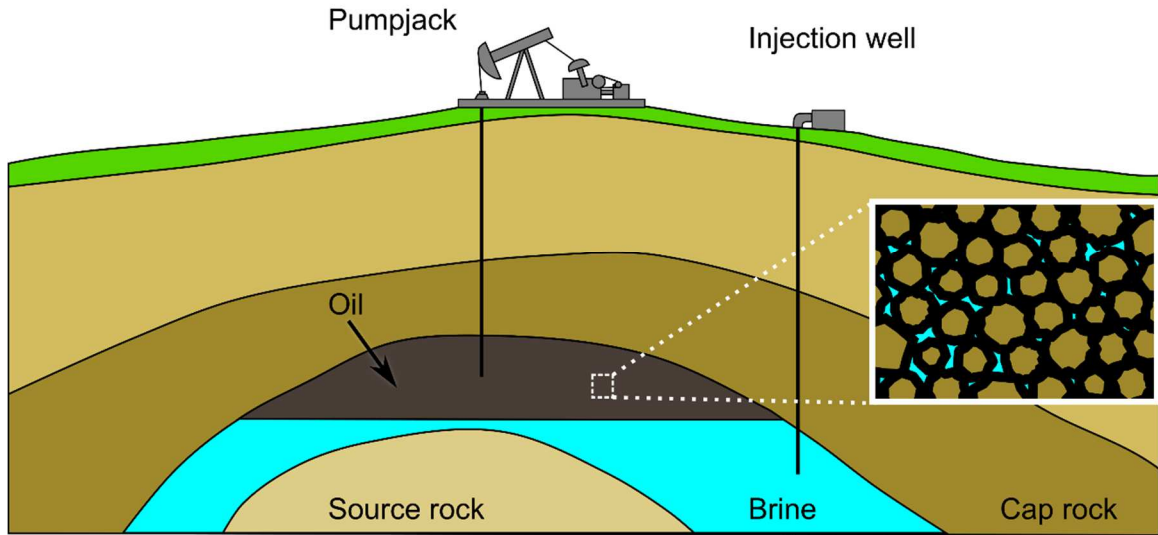
Figure 5.1: Diagram of an anticlinal oil reservoir showing, left to right and top to bottom: pumpjack for extracting liquid from the reservoir; injection well for adding liquid to the reservoir system; oil trapped at top of reservoir; source rock from which oil and water originate; brine trapped within reservoir; and cap rock, higher density rock which keeps the contents of the reservoir contained. Inset shows structure of oil region with crude oil coated aggregate sand, rock, and clay commingled with brine.

Oil deposits originate from organic matter deposited in aquatic sediment, such as that found in deep marine basins, continental shelves, or anoxic lakes.[131–133] This matter is decomposed by bacteria into methane. As the sediment gradually moves deeper into the crust heat and pressure convert the organic matter into kerogen, an insoluble organic matter. Further heat and pressure convert the kerogen into petroleum and bitumen. This process will continue, eventually reducing these complex compounds into simpler, lighter gases, although complete reduction will require significant time, up to hundreds of millions of years. These substances, both liquid and gas, migrate

upwards through the source rock and may potentially be trapped in porous reservoir rock beneath impermeable cap rock (Figure 5.). Not all petroleum produced in this fashion ends up trapped in reservoirs and can easily be lost if no cap rock is present. These systems are incredibly complex, as the components present and their interactions vary greatly depending on the original source of the organic material, the type of sediment deposit, the depths the sediment reached, the age of the hydrocarbons, and the mineral makeup of the reservoir rock.

Our focus is on retaining as much of the complexity of the original reservoir system as possible, including elevated temperature, elevated pressure, crude oil composition, brine composition, and a 2D mineral substrate. The traditional method for testing these systems is core flooding, which involves taking a cylindrical sample of rock ("core") and submerging it in oil until it is saturated and then forcing a brine solution through it, examining the quantity of oil recovered.[117,134–143] Traditionally, these tests are often performed at ambient temperature and pressure, although some high pressure high temperature variations exist.[144–150] In all cases, however, the tests are macroscopic and average over all mineral species within a sample. Tortuosity effects from the core's structure can also not be disentangled from the results. These factors limit the ability of experiments to show direct causal links behind improvements in extraction and provide guidance as to the most promising directions for further study. By utilizing force spectroscopy, with its small probe size, it becomes possible to instead investigate these interactions at the scale of individual mineral grains. This allows for examination of interactions of the oil with each mineral species present in a reservoir and can eventually generate a broad understanding of this system. This would provide an *ab initio* basis for customizing extraction approaches to the specific composition of any given reservoir. Previously, a crude-oil functionalized probe had been developed in our

lab for such experiments,[151] but all tests were carried out at ambient temperature and pressure. Here we describe our work investigating this system using a new high pressure high temperature (HPHT) AFM, a hybridized version of high pressure[81,83,152] AFMs and high temperature[82] AFMs, which could only achieve one condition or the other. By creating an improved version of the customized crude-oil functionalized probe able to withstand high temperatures and pressures, we were able to expand these experiments into a new parameter space, demonstrating for the first time the possibility of carrying out force spectroscopy in this pressure/temperature regime.

5.2. Development and Method

Expanding the capacity of the existing probe to maintain functionality at high temperature and pressure required substantial testing and modification. The previous version consisted of a 7 μm silica sphere which was attached to a bare cantilever and then coated in crude oil. This probe was then dried at 50 °C before use. This version was capable of performing tests at ambient temperature and pressure, but when exposed to higher temperatures the oil coating was not stable enough to stay on the probe. By silanizing the sphere before coating, we increased the hydrophobicity of the surface to reduce wetting by the brine and improved coating retention. We also dried the probe at a higher temperature, 150 °C, driving off even more of the volatile components of the oil while still retaining the asphaltenes, considered the dominant component in the interaction.[153–155] This created a more robust coating, less likely to deform at high temperature. The probes were also dried under 30 inHg vacuum instead of ambient pressure. This change limits the amount of oxidation the oil undergoes during drying, as these reactions are more likely to occur at the increased temperature and could change the surface interactions.
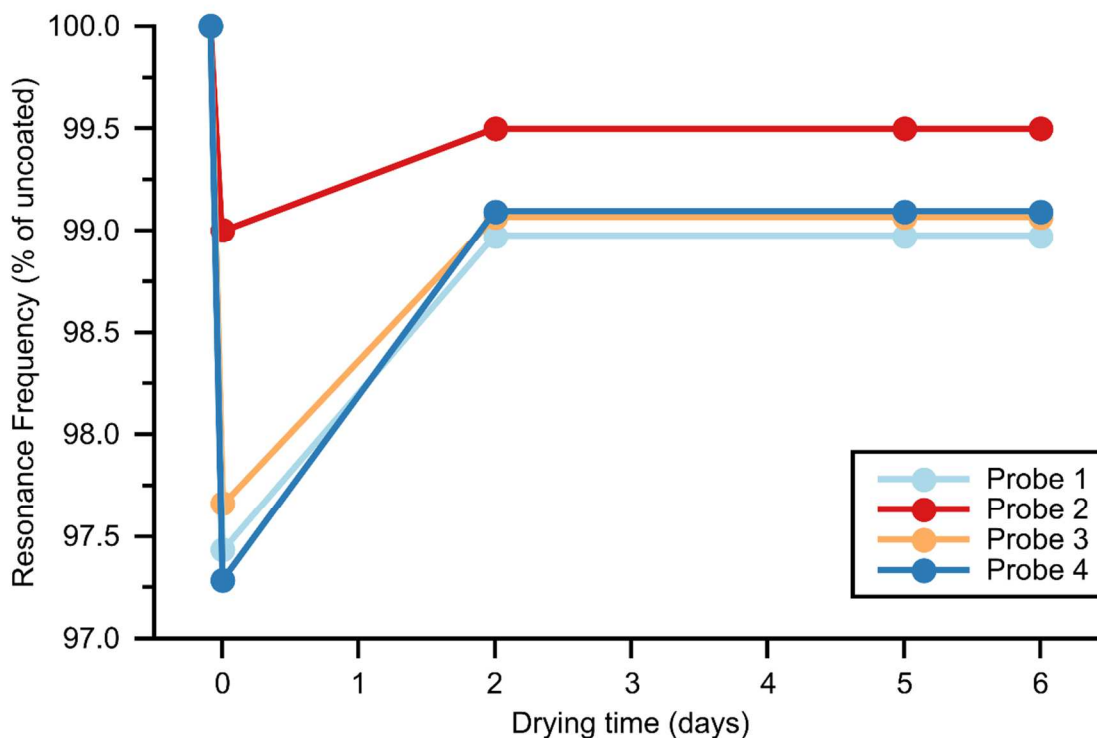
Figure 5.2: Change in resonance frequency of newly oil coated probes during the drying process. Frequency is shown as percentage of the resonance frequency of the probe before coating, typically around 20 kHz. The first point on the left indicates this starting frequency, with the following, lowest point taken immediately after coating with crude oil.

We tracked the progress of the drying process by measuring the shifts in the resonance frequency of the drying probes (Figure 5.2). Previously, this process had been tracked by examining the interference patterns in the oil coating using an optical microscope and waiting for them to stabilize. This required an oil coating that extended significantly down the cantilever and the patterns were difficult to track quantitatively. Our new approach is simpler, can be used with less oil, and provides an explicit measure for tracking the drying process. It was demonstrated experimentally by Cleveland, et al.[156] that the resonance frequency of an AFM cantilever changes with the addition or subtraction of mass from it. Therefore, by tracking changes in this frequency, we can

determine the reduction in the added oil weight during the dry process, as the lighter, more volatile compounds evaporate. Frequency sweeps are taken before coating to establish a baseline value, immediately after coating, which has the lowest frequency due to the added mass, and then every few days thereafter, where the frequency increases slightly from the lowest point as the volatile components of the oil are driven off. The probe is considered "dry" when the frequency is stable over successive trials. This method also gives comparative data on the amount of oil present on each probe. As probe 2 in Figure 5.2 shows a smaller decrease in resonance frequency compared to the other probes, we know that it has been coated with less oil. This allows for the possibility of tracking this oil layer thickness and comparing it to adhesion results in follow-up experiments.

In addition to the question of oil coating stability, the cantilever itself also required a change when used at higher temperatures. Prior tests had used a cantilever with a 70 nm thick gold coating on the back side. This enhances reflectivity, and therefore the intensity of the reflected laser beam, providing a clearer signal. However, at high temperatures, a bimetal effect resulting from the unequal expansion coefficients of the silicon nitride cantilever and the gold coating causes the cantilever to bend out of alignment and push the reflected laser spot outside the range of the photodetector used to track the deflection of the cantilever. We changed to cantilevers that were coated on both sides with gold to prevent this bending. The changed surface still maintained sufficient bonding with the marine epoxy used to attach the sphere.
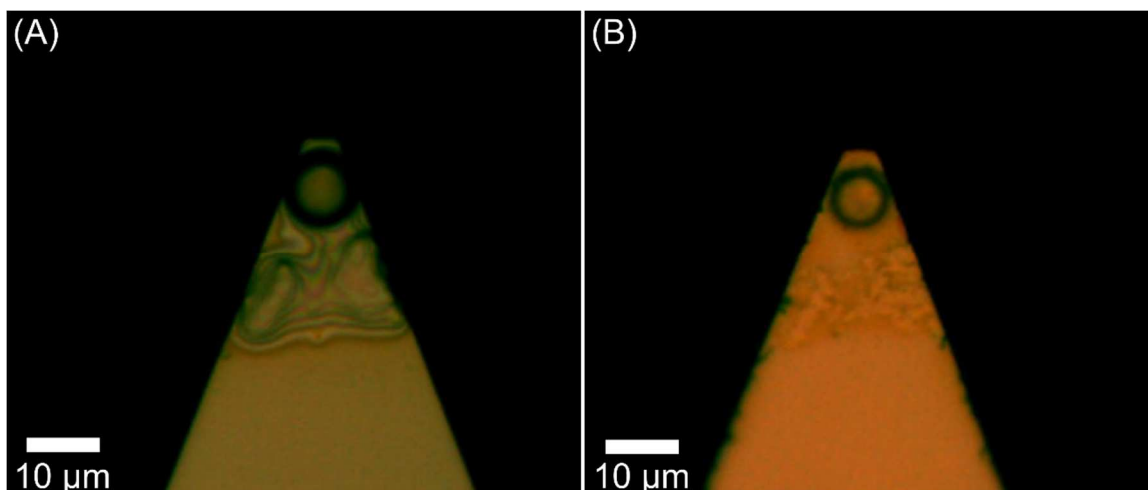
Figure 5.3: Optical image of colloidal probe attached with silicone epoxy before (A) and after (B) pyrolyzation – 3 hours in a tube furnace at 500 °C.

Several methods were also attempted to provide a more robust and inert attachment method for the spheres. The most promising of these was attaching the spheres with a silicone-based epoxy and then pyrolyzing the tips in a tube furnace for 3 hours at 500 °C. This also required the double-coated cantilevers, as the single-sided coated cantilevers would bend to the point of breaking in the furnace. This converts the epoxy into silica, which would be completely inert and of the same heat-resistant material as the sphere itself, preventing any potential contamination of the experiment. While this method did generate attached spheres, they were only capable of surviving a few force curves at ambient conditions before the attachment failed. The survival rate for merely moving the probes before or after use was also substantially lower than standard, as the spheres would sometimes fall off just from this action. This prevented the use of this method of attachment in the final version of the probe, though it might be possible to improve it to the point of usefulness with additional work at a later date.

The cumulative results of the improvements to the oil coating and cantilever are shown in Figure 5.4, which has images of probes made using the original process (A and B)

and the improved process (C and D) that have been immersed in near-boiling synthetic seawater for two hours. The oil coating, the original extent of which has been outlined in red in both images, decreased dramatically during immersion for the first probe, but is unchanged for the second.
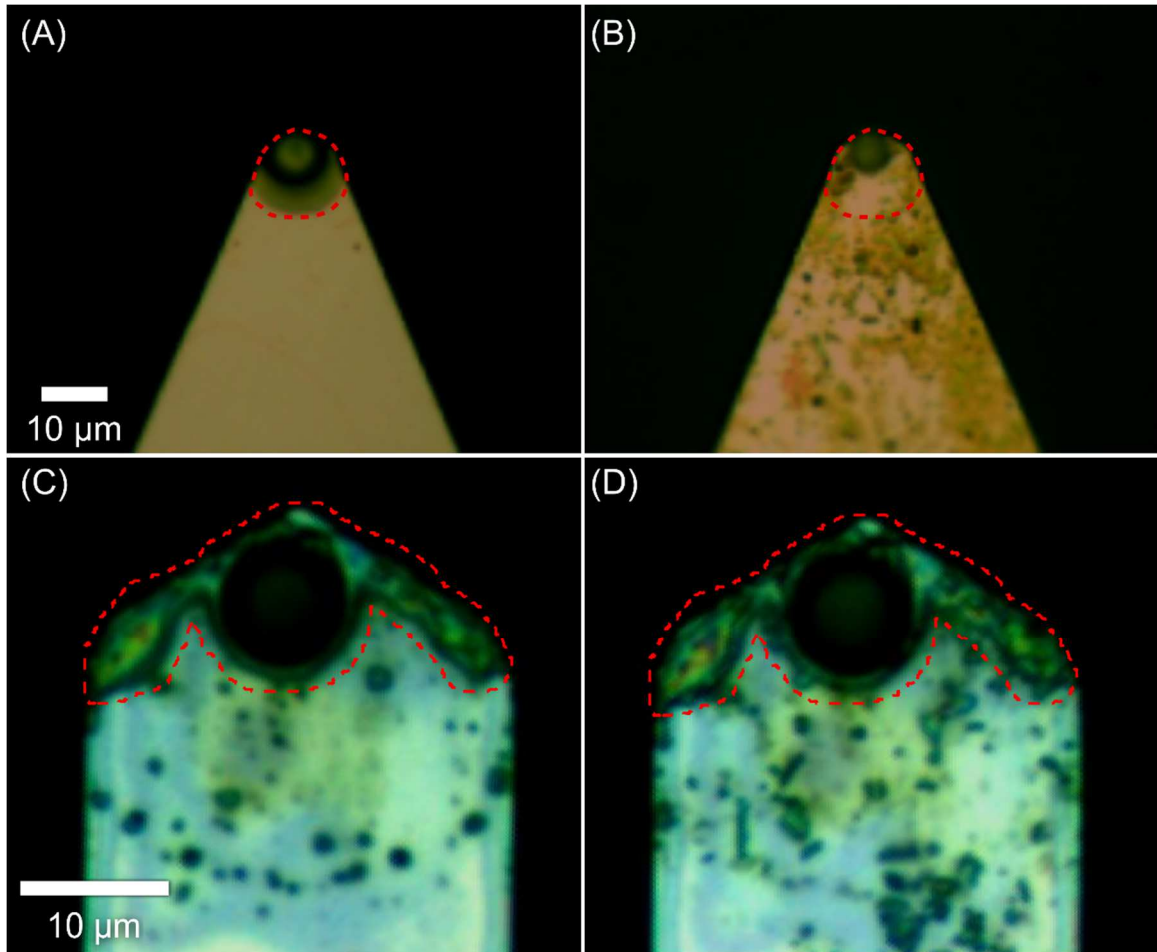
Figure 5.4: Optical images of oil coated probes before (A and C) and after (B and D) immersion in boiling synthetic seawater for two hours. The first probe (A and B) was not silanized before being coated with oil and was dried at 50 °C under ambient pressure. The second probe (C and D) was silanized before coating and was dried at 150 °C under vacuum.

5.3. Testing Results

Initial tests with the new probes showed that their capabilities matched those of previous probes at room temperature. Preliminary measurements taken on the NT-MDT Ntegra AFM with probes using the new manufacturing process were consistent with the work using the previous version of the probe. A series of one hundred curves taken on mica in a salt brine at room temperature and atmospheric pressure showed almost no deviation, with mean adhesion of 4.0 nN and a standard deviation of 0.3 nN (Figure 5.5). No signs of sphere removal or oil layer damage were seen; these would have been visible as a sudden deviation from or gradual shift away from, respectively, the standard curve seen in the overlaid series.
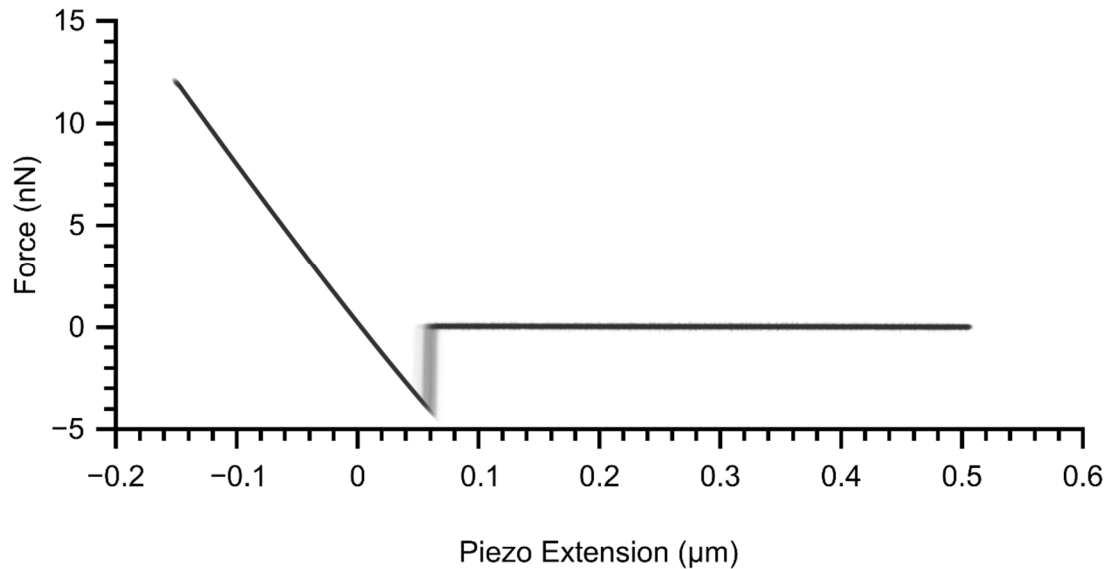
Figure 5.5: One hundred force-distance curves from the preliminary experiments using the new probe manufacturing process with the NT-MDT Ntegra AFM at room temperature and atmospheric pressure. Lines connecting the points in each curve are overlaid on top of one another and set to 5% opacity. The thicker gray line joining the two darker segments is an artifact of the overlay process and does not represent actual points of data, merely the line connecting the points in each curve, which jumps from the lowest point on each curve to the

beginning of the horizontal zero deflection region. The mean adhesion for this set was 4.0 nN, with a standard deviation of 0.3 nN.

After these promising initial results work next shifted to the newly-constructed high pressure, high temperature AFM. However, issues became apparent when force curves were first taken with the system heated to 100 °C. The temperature differential between the top of the liquid cell and the surrounding air caused convection currents to form, randomly changing the length of the optical path of the laser on its way to the photodetector. This shows as low frequency distortions in any force curve data, as seen in Figure 5.6A. The magnitude of these fluctuations is larger than the size of any features related to adhesion or repulsion. As the project was on a fixed schedule and could not be delayed to produce a more permanent solution, a fan was used to blow air through the optical path. This introduces a consistent, high-frequency noise with a lower amplitude than that of the shifts from the convection currents (Figure 5.6B). The consistency and lower amplitude made noise reduction techniques effective and allowed us to acquire useful information about the system within these constraints.

(A)   (B)
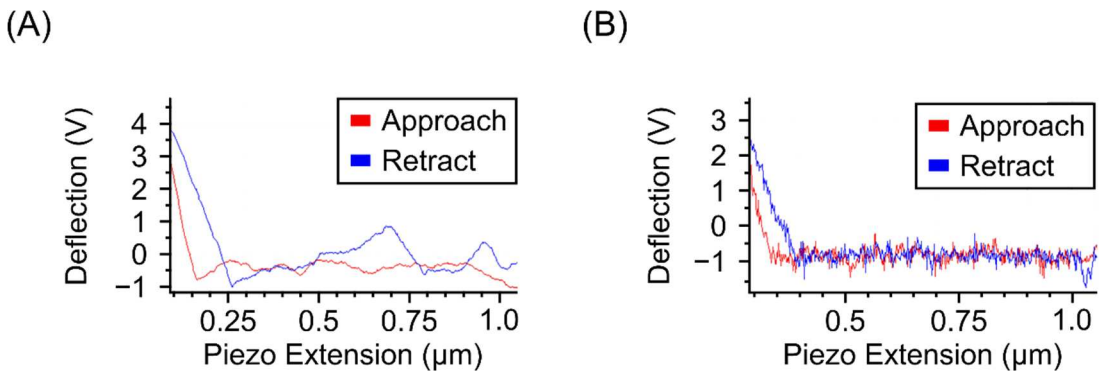
Figure 5.6: Force-distance curves on mica with a sharp silicon cantilever taken at 100 °C without (A) and with (B) a fan blowing air through the optical path of the laser.

Sample force curve data is shown in Figure 5.7, with data taken at 25 °C and 100 °C in (A) and (B), respectively. The maximum adhesive force is each plot is found at the lowest point on the line, indicated by a red ring. This corresponds to the largest amount of upward force applied by the cantilever before the probe broke contact with the sample surface. The 25 °C curve features low noise and a clear minimum value of 11.6 nN. The 100 °C curve has a large amount of noise in the original data (gray points) but after taking a 100-point average around each point a maximum adhesive force of 37.1 nN was measured. While the noise did impose of lower limit of 10 nN to the adhesive force that could be measured, clear trends were still evident in the measured data as functions of both temperature and pressure.

(A)

(B)
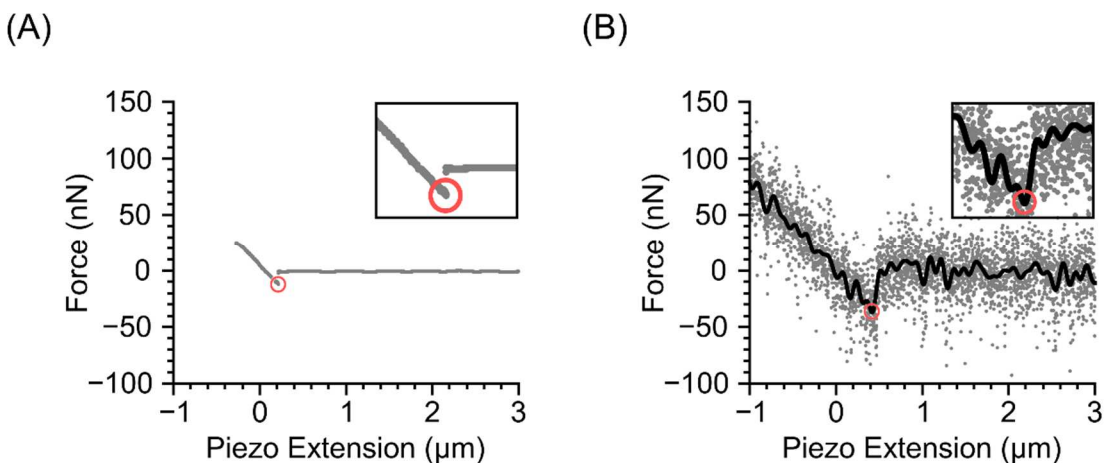
Figure 5.7: Retract portion of force curves taken at 25 °C (A) and 100 °C (B) with a colloidal probe on mica. The red ring in each plot indicates the maximum adhesive force, with inset showing additional detail. Gray points are measured data, with the black line in (B) showing a 100-point average. The maximum adhesion is 11.6 nN in (A) and 37.1 nN in (B)

Adhesive force measurements as a function of pressure are shown in Figure 5.8, with measurements taken at 25 °C in blue (A) and those at 100 °C in red (B). Each data point, represented as hollow circle, is the maximum adhesive force measured in a single force curve. Although all points were taken at either 0.7 MPa or 10 MPa, they

have been given a slight random horizontal offset to improve visibility. The black

horizontal bar in (A) gives the median value for each set, with the boxes above and

below this bar indicating the extent of the second and third quadrants. The median

value for the 25 °C measurements was 10.02 nN for 0.7 MPa and 4.53 nN for 10 MPa.

This is a statistically significant decline in adhesive force with increased pressure, with

a Wilcoxon rank sum test p-value of 3.03×10^{-17} and a common-language effect size of

0.738 (a 73.8% chance that a random point from the 0.7 MPa measurements will be

higher than a random point from the 10 MPa measurements).

(A)   (B)
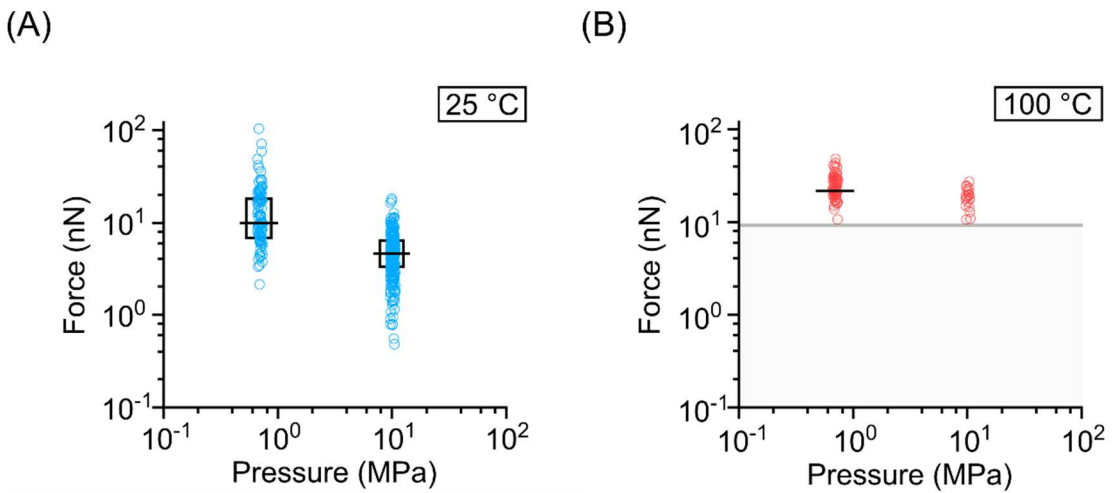
Figure 5.8: Maximum adhesive force as a function of pressure at 25 °C (A) and 100 °C (B).
The horizontal bar in (A) shows the median value for each set (10.02 nN and 4.53 nN for
measurements at 0.7 MPa and 10 MPa, respectively) and boxes indicate second and third
quadrants. Horizontal black bar in (B) shows median value of 21.09 nN for 0.7 MPa
measurements. Gray box indicates noise-induced threshold from fan-induced noise in signal.
Points have been set to 5% opacity and given a slight, random horizontal offset to increase
visibility.

The measurements taken at 100 °C represented a larger challenge to examine. Due

to the 10 nN lower limit imposed on the measurements by the fan-induced noise

(indicated by the gray hatched box in Figure 5.8B), the maximum adhesive force was

not measurable in all curves. From the curves taken at 0.7 MPa, 71% of (66 of 93) showed measurable adhesion, with the remaining curves showing adhesion below the noise threshold. The median adhesion force for the entire set was 21.09 nN, indicated by the horizontal black bar. It was possible to determine this because any non-measurable adhesion values must be below 10 nN and therefore below the median as they represent less than half of the total number of measurements. Only 19% of the measurements taken at 100 °C were above the noise threshold, and we were correspondingly unable to determine the median value for the set. However, as this median value must be below the noise threshold of 10nN, it still represents an overall decrease in adhesive force from the values found in the 25 °C set.

We next examined the results as a function of temperature. In the measurements taken at 0.7 MPa, those at 25 °C had a median value of 10.02 nN while those at 100 °C had a median value that increased by more than a factor of two, to 21.09 nN. Due to the noise threshold, comparing measurements taken at 10 MPa presented another challenge as the values were comparatively lower than those at 0.7 MPa. Here we examined the portion of the curves that exceeded 10 nN, with 6% of the curves taken at 25 °C and 10 MPa exceeding this value as compared to the 19% of those taken at 100 °C and 10 MPa. As we cannot verify the shape of the distribution for the adhesion values for the set taken at 100 °C and 10 MPa we cannot definitively conclude that the adhesion increased with temperature, but the results are strongly suggestive.

5.4. Discussion

Our results show that adhesion decreases with an increase in pressure at both temperatures tested. This could result from an increase in dissolved CO_2 at higher pressure, leading to the formation of carbonic acid and a corresponding decrease in

pH. The isoelectric point of mica is reported as being 5[157] or below,[158] and that of crude oil in the range between 3 and 7,[159–162] depending on source. Passing these points would modify the surface charge and impact oil-mica interactions, especially those portions of the probe to the sides of the direct oil-mica contact region, which would still be in range of longer range, repulsive electrostatic forces, but outside that of the shorter range, strongly attractive van der Waals interactions. The increase in pressure could also impact the stiffness of the oil layer, decreasing deformation during contact and limiting the contact area available for van der Waals interactions.

Our results also demonstrate that adhesion increases with temperature at both pressures tested. This could also stem from changes in electrostatic interactions. Double layer theory predicts that increased thermal motion would diminish the screening effect of any ions in solution. The moderate change in temperature used in these experiments would result in an approximate 10% change in the Debye length, due to the square root dependence on temperature.[79] Another possibility is a change in surface charge due to shifts in the protonation constants of the mica with temperature, an effect which has been shown to occur in other silicates.[163] The stiffness of the oil layer may be also decrease with increased temperature, increasing the size of the contact area and the effective area for van der Waals interactions.

5.5. Conclusion

Combining the capabilities of a crude oil functionalized probe with a HPHT AFM made it possible for us to measure the forces that govern a petroleum reservoir in a previously unexplored way. We have shown that increasing the pressure of the testing environment decreases the adhesion between probe and substrate for both temperatures tested. Additionally, we showed that adhesion increases with

temperature for the two temperatures tested. To further explore these results, future tests should involve different crude oils and substrates, such as quartz. Additionally, the aqueous solution may be changed to modify the salinity, utilize other liquid additives (e.g. surfactants), manipulate the CO_2 levels or other dissolved gases, and modify the pH levels. To identify inflection points and/or sudden shifts in the behavior of the forces, the experiments should be repeated by gradually changing the temperature and pressure throughout the experiment. This gradual methodology would be further enhanced by automated testing, which would allow a greater level of precision. To probe the changing influences of the competing electrostatic and van der Waals forces, changing the sphere size on the probe would modify the radius of curvature, allowing different portions of the sphere to be in different regions of influence of these distance dependent forces. Ultimately, using live crude oil for probe creation, dried under inert gas to reduce oxidation, and live formation or injection liquids in the experiments would give the best representation of what is actually occurring in the depths of a petroleum reservoir.

Chapter 6

Conclusions and Future Work

In our efforts to expand the understanding of, and eventual larger use of, 2D materials, we have demonstrated several important advancements in this work. We detailed a new characterization technique for these materials, based on optical microscopy, and established its utility by using it to uncover new insights into a new emulsion-based exfoliation technique. We also showed direct measurements of the interactions between 2D materials and an oil–water interface, shedding yet more light on the nature of this exfoliation process. Additionally, we demonstrated a method for examining interactions between an oil-functionalized probe and a 2D mica substrate at high pressure and high temperature using force spectroscopy. Each of these represent significant advancements, with a variety of current and future applications.

In Chapter 3, we described our new method for optical characterization of 2D materials. Our method uniquely combines low-magnification optical microscopy with techniques inspired by scanning probe microscopy image processing. This provides rapid, low-cost size and thickness characterization of populations of nanosheet materials. It also

offers a simple means of tracking the oxidation state and optical constants of GO without additional processing. We then used this technique to examine the material produced via the emulsion-based exfoliation method. By examining material selected from a liquid–liquid interface, material not moved to the interface but in proximity, and untouched material, we showed that the material is exfoliating itself at this interface, not merely sorting existing flakes. This shed new light on the behavior of the system at the morphological level, which had been previously inaccessible.

In Chapter 4, we directly measured interactions between 2D materials and a liquid–liquid interface using force spectroscopy. This required three separate developments: taking a customized GO-functionalized probe that had previously been used only in air and taking it into an aqueous environment, finding a method for reducing the GO on that probe to a graphene-like state without damaging the probe, and creating a micropatterned hydrophilic/hydrophobic substrate to generate stable and consistent bubbles of heptane in water. Our results show that these 2D materials show significant, measurable attraction to and adhesion with this liquid–liquid interface. And that the response is species-dependent, with graphene showing a significant long-range attraction and strong adhesion while GO, which readily suspends in water, showed only short-range attraction but still maintains strong adhesion. This demonstrates the viability of this method in determining the underlying mechanisms of this 2D surfactant-like behavior.

Finally, in Chapter 5, we measured the interactions between an oil-coated probe and a mineral substrate at high pressures and temperatures using force spectroscopy. These measurements are the first of their kind in this temperature and pressure regime. Achieving these results required extensive modifications to the oil-coated probe, including increasing the drying temperature to increase robustness of the

coating, drying under vacuum to reduce oxidation, rendering the probe hydrophobic before coating to limit loss of the coating due to wetting, and the use of special double-coated cantilevers to prevent bending due to a bi-metal effect at high temperatures. Our results demonstrate that not only is it possible to perform this technique in such extreme environments, the impacts of both variables are significant. We saw adhesion increase by a factor of two when bringing the temperature from 25 °C to 100 °C and decrease by a factor of two when the pressure was brought from 1 atm to 100 atm. This demonstrates the importance of accounting for these environmental changes.

Each avenue explored here provides its own additional routes for future work. The optical characterization technique from Chapter 3 can be readily applied to other materials and other systems. In particular, it holds potential promise for tracking growth of materials in CVD chambers. Here the contrast changes could eventually be used not only to detect differences between different layers of the same material, but also in combinations of materials, aiding the creation of layered systems which have a bright future in this field. General automation of the process would also be beneficial. The layer numbers of different sheets could be determined more precisely by correlating across multiple colors of light, using different wavelengths in accordance with the layer number region they work best in. It is also possible to shift all the processing into a single program (or extension for ImageJ) and reduce the time required before results are available even further, perhaps even reaching real-time.

The results of the emulsion process, as examined by the optical characterization technique, also provide additional avenues for exploration. An obvious first step would be to vary the source material. Either different forms of GO (either non-Hummers production techniques or varying the source graphite would work) or other 2D materials completely would be instructive. Additionally, repeating the emulsion process with the

material acquired after the first step (e.g. creating an emulsion using only material pulled from the interface), would contribute to a far more complete road map of the effects of the process.

The liquid-liquid interfacial measurements from Chapter 4 are open to significant expansion. First, additional trials are needed for further clarification of the intriguing long-range behavior described here. Varying the degree of reduction of the GO coating could help with this, as would reversing the substrate system. By creating hydrophilic patches on a hydrophobic background, consistent water bubbles could be placed under heptane, allowing testing to take place from the other side of the interface. This would provide insight into both sides of the potential well experienced by the material. Exploring other liquids, whether different alkanes, other solvents, or polymer systems, would also prove beneficial. Pursuing additional probe functionalization techniques would allow the examination of other 2D materials as well. Here, using the emulsion technique with material that naturally contains a significant proportion of sheets with diameter greater than ten microns offers a promising route to producing these additional coatings.

The experiments with force spectroscopy at high pressure and high temperature from Chapter 5 also provide a number of options for future work. After refining the detection system, further exploring the new parameter space demonstrated here is the next course of action. This would be greatly aided by automating the pressure and temperature manipulation of the system, allowing for simplified iterative testing. Modifying the liquid environment is another step, whether with liquid additives such as surfactants, various dissolved gases, or pH adjustments. "Live" or unoxidized crude oil or formation liquid (the native non-oil liquid inside the reservoir) could also be used to more closely replicate the environment, as well as use of different mineral species.

These experiments would also lend themselves well to exploration of similar systems, examining lubrication in combustion engines or mechanical systems, or catalytic cracking as used in the petroleum industry. Another, less-obvious route, would be to examine biological specimens found at deep-sea vents. The high temperatures and pressures found here lead to strange life forms that could be mined for potential biomimetic applications.

With this work, we have not only expanded the understanding of these specific, important systems, but also provided tools and methods that will be useful beyond the experiments described here. There is, as ever, much that remains to be explored in our world. We hope that the information contained here may help those explorers yet to come.

Appendix A

InvertMountain ImageJ Macro

Information

An ImageJ macro that finds local brightness maxima within an image, determines the maximal area around each maximum in which the brightness decreases, then inverts the brightness in those regions about a pre-determined inflection point.

Adapted from the Supplementary Information from "High-throughput optical thickness and size characterization of 2D materials" by Dickinson, et al. published in Nanoscale in 2018 with permission from The Royal Society.

Tested with ImageJ v1.50b

Instructions for Use

First, install the macro through use of the `Plugins>Macros>Install...` menu option. Second, select the image to be processed. The macro will act on the current selection within the image, or the entire image if no selection is made. Third, execute the macro through the

`Plugins>Macros>Invert Mountain Tool` menu option. This will generate a window with several parameters available for modification:

`Inflection Point:` The brightness value that the inversion occurs about. Correlates with the value at which the brightness-vs-layer number relationship inverts.

`Maxima Noise Tolerance:` Minimum amount by which the brightness of a maximum must exceed the surrounding area. Must be >= 0.

`Exclude Edge Maxima:` If `true`, a peak is only accepted if it is separated by two qualified valleys. If `false`, a peak is also accepted if separated by one qualified valley and by a border.

`Flood Noise Tolerance:` Maximum value by which the brightness of neighboring pixels may exceed the brightness of the pixel being examined. Prevents noise in the image from prematurely terminating the mountain.

`Sanity Threshold:` Pixels above this brightness value are automatically included in the mask. Prevents exclusion of "obviously inverted" points due to greater noise than expected. For analysis of layered materials, this should be above substrate value by a brightness corresponding to at least one layer.

`Fill Holes:` If `true`, areas fully enclosed within a region that has been identified as part of a mountain will be added to the region before inversion occurs.

Finally, after adjusting all parameters to the desired values, press the `OK` button, and the macro will act on the image.

Code

Code also available at GitHub: (https://github.com/schniepp-lab/invert-mountain)

```
//      MIT License
//      Copyright (c) 2017 William W. Dickinson
//
//   Invert Mountain tool
//      An ImageJ macro that finds local brightness maxima within an image,
//      determines the maximal area around each in which brightness decreases,
//      then inverts the brightness in those regions about a pre-determined
//      inflection point.
//
//      Tested with ImageJ 1.50b
//
//      ===========
//
//      Instructions
//      -----------
//      First, install the macro through use of the Plugins>Macros>Install... menu
//      option.
//
//      Second, select the image to be processed. The macro will act on the current
//      selection within the image, or the entire image if no selection is made.
//
//      Third, execute the macro through the Plugins>Macros>Invert Mountain Tool
//      menu option. This will generate a window with several parameters available
//      for modification (see below for descriptions).
//
//      Finally, after adjusting all parameters to the desired values, press the OK
//      button, and the macro will act on the image.
//
//      ===========
//
//      Parameters
//      -----------
//
//      Inflection Point:
//      The brightness value that the inversion occurs about. Correlates with the
//      value at which the brightness-vs-layer number relationship inverts.
//
//      Maxima Noise Tolerance:
//      Minimum amount by which the brightness of a maxima must exceed the
//      surrounding area. Must be >= 0.
//
//      Exclude Edge Maxima:
//      If 'true', a peak is only accepted if it is separated by two qualified
//      valleys. If 'false', a peak is also accepted if separated by one qualified
//      valley and by a border.
//
//      Flood Noise Tolerance:
//      Maximum value by which the brightness of neighboring pixels may exceed the
//      brightness of the pixel being examined. Prevents noise in the image from
//      prematurely terminating the mountain.
//
//      Sanity Threshold:
//      Pixels above this brightness value are automatically included in the mask.
//      Prevents exclusion of "obviously inverted" points due to greater noise
//      than expected. For analysis of layered materials, this should be above
//      substrate value by a brightness corresponding to at least one layer.
//
//      Fill Holes:
//      If 'true', areas fully enclosed within a region that has been identified as
//      part of a mountain will be added to the region before inversion occurs.
//
//      ===========
```

```
var stack = newArray(100000);    //    Array of pixels to be evaluated
var stackSize;                    //     Current pixel in the stack being looked at
var mask;              //    Array showing which pixels are within a mountain
var width;             //    Pixel width of the image
var height;            //    Pixel height of image

macro "Invert Mountain Tool" {
        Dialog.create("Invert Mountains");
        Dialog.addNumber("Inflection Point:", 70.0);
        Dialog.addNumber("Maxima Noise Tolerance:", 10);
        Dialog.addCheckbox("Exclude Edge Maxima", true);
        Dialog.addNumber("Flood Noise Tolerance:", 0.0);
        Dialog.addNumber("Sanity Threshold:", 110.0);
        Dialog.addCheckbox("Fill Holes", true);
        Dialog.show();

        inflectionPoint = Dialog.getNumber();
        maximaTolerance = Dialog.getNumber();
        exclude = Dialog.getCheckbox();
        floodTolerance = Dialog.getNumber();
        sanityThreshold = Dialog.getNumber();
        fillHoles = Dialog.getCheckbox();
        options = "";
        if (exclude) options = options + " exclude";

        currentImage = getImageID;
        width = getWidth;
        height = getHeight;
        mask = newArray(width * height);
        Array.fill(mask, 0);

        run("Find Maxima...", "noise="+ maximaTolerance +" output=List"+options);

        setBatchMode(true);
        roiManager("reset");

        stackSize = 0;
        for(j=0; j < nResults; j++) {
            x = getResult("X", j);
                y = getResult("Y", j);
                push(x,y);
        }

        findMountains(floodTolerance, sanityThreshold);

        newImage("MountainAreas", "8-bit", width, height, 1);
        selectImage("MountainAreas");

        for(i=0; i<width; i++){
                for(j=0; j<height; j++){
                        if (mask[i+j*width]==1){
                                setPixel(i,j,1);
                        }
                }
        }

        run("Make Binary");
        if (fillHoles)
                run("Fill Holes");
        run("Create Selection");
        roiManager("add");
        selectImage(currentImage);
        roiManager("select", 0);

        invertMountains(inflectionPoint);

        if (isOpen("Results")) {
                selectWindow("Results");
                run("Close");
        }

}
```

```
//    Determines the extent of the region around each of a list of pixels where
//    brightness decreases from that pixel. It checks each pixel to the left,
//    sequentially, for lower brightness than its neighbor and adds them to the
//    mask if this is true. It then checks those to the right, repeating the
//    process. It then checks pixels above, below, and diagonally adjacent to
//    each of the pixels on the line and adds them to the list of pixels to be
//    examined in this fashion.
//
//    Parameters:
//    ------------
//
//    floodTolerance:
//    Amount of variation above the threshold value allowed before determining
//    that an inflection point has been reached.
//
//    sanityThreshold:
//    Any pixel above this brightness value is always included in the mask.
//    Prevents exclusion of "obviously inverted" points due to greater noise
//    than expected. Should be at least 1 layer step above substrate value.

function findMountains(floodTolerance, sanityThreshold) {
        autoUpdate(false);
        numScanned = 0;
        while(true) {
                coordinates = pop();
                if (coordinates ==-1) return;
                numScanned++;
                x = coordinates&0xffff;
                y = coordinates>>16;
                x1 = x;
                x2 = x;

                mask[x+y*width] = true;

                limit = getPixel(x,y) + floodTolerance;

                // prevent tolerance from creeping upward during scan-line changes
                if (inMask(x,y-1))
                        limit = minOf(limit, getPixel(x,y-1) + floodTolerance);
                if (inMask(x+1,y-1))
                        limit = minOf(limit, getPixel(x+1,y-1) + floodTolerance);
                if (inMask(x-1,y-1))
                        limit = minOf(limit, getPixel(x-1,y-1) + floodTolerance);
                if (inMask(x,y+1))
                        limit = minOf(limit, getPixel(x,y+1) + floodTolerance);
                if (inMask(x+1,y+1))
                        limit = minOf(limit, getPixel(x+1,y+1) + floodTolerance);
                if (inMask(x-1,y+1))
                        limit = minOf(limit, getPixel(x-1,y+1) + floodTolerance);

                // Checks pixels to left of the this one
                i = x-1;
                while (!inMask(i,y) && (getPixel(i,y)<=limit ||
getPixel(i,y)>sanityThreshold) && i>1) {
                        mask[i+y*width] = true;
                        x1 = i;
                        i--;
                        limit = minOf(getPixel(i,y) + floodTolerance, limit);
                }

                //Checks pixels to the right of this one
                limit = getPixel(x,y) + floodTolerance;
                i = x+1;
                while(!inMask(i,y) && (getPixel(i,y)<=limit ||
getPixel(i,y)>sanityThreshold) && i<(width-1)) {
                        mask[i+y*width] = true;
                        x2 = i;
                        i++;
                        limit = minOf(getPixel(i,y) + floodTolerance, limit);
                }
```

```
                // find pixels above this line
                if (y>1){
                    for (i=x1; i<=x2; i++) {
                        limit = getPixel(i,y) + floodTolerance;
                        if (!inMask(i,y-1) && getPixel(i,y-1)<=limit) {
                            push(i, y-1);}
                        if (i>1 && !inMask(i+1,y-1) && getPixel(i+1,y-1)<=limit)
{
                            push(i+1, y-1);}
                        if (i<(width-1) && !inMask(i-1,y-1) && getPixel(i-1,y-
1)<=limit) {
                            push(i-1, y-1);}
                    }
                }

                // find pixels below this line
                if (y<(height-1)){
                    for (i=x1; i<=x2; i++) {
                        limit = getPixel(i,y) + floodTolerance;
                        if (!inMask(i,y+1) && getPixel(i,y+1)<=limit) {
                            push(i, y+1);}
                        if (i>1 && !inMask(i+1,y+1) && getPixel(i+1,y+1)<=limit)
{
                            push(i+1, y+1);}
                        if (i<(width-1) && !inMask(i-1,y+1) && getPixel(i-
1,y+1)<=limit) {
                            push(i-1, y+1);}
                    }
                }
        }
}

//      Adds pixel to stack
function push(x, y) {
        if (x>0 && x<(width-1) && y>0 && y<(height-1)){
                stackSize++;
                stack[stackSize-1] = x + y<<16;
        }
}

//      Removes pixel from stack
function pop() {
        if (stackSize==0)
                return -1;
        else {
                value = stack[stackSize-1];
                stackSize--;
                return value;
        }
}

//      Checks if a pixel is in the mask. Returns false if outside the image border
function inMask(x,y) {
        if (x>0 && x<width && y>0 && y<height)
                value = mask[x+y*width];
        else
                value = false;
        return value;
}

//      Inverts selected region about the given inflection point. The "Invert" tool
//      will not make values below 0, instead shifting them higher until the lowest
//      is above 0. The offset value determined below accounts for this and permits
//      negative brightness values.
function invertMountains(inflectionPoint) {
        getStatistics(area, mean, min, max, std, hist1);

        run("Invert");
        getStatistics(area, mean, min2, max2, std, hist1);

        offset = (min - min2) + (2*inflectionPoint - (max+min));
```

```
        run("Add...", "value="+offset);
}
```

References

1. Butler, S. Z. *et al.* Progress, Challenges, and Opportunities in Two-Dimensional Materials Beyond Graphene. *ACS Nano* **7**, 2898–2926 (2013).
2. Sengupta, R., Bhattacharya, M., Bandyopadhyay, S. & Bhowmick, A. K. A review on the mechanical and electrical properties of graphite and modified graphite reinforced polymer composites. *Progress in Polymer Science* **36**, 638–670 (2011).
3. Young, R. J., Kinloch, I. A., Gong, L. & Novoselov, K. S. The mechanics of graphene nanocomposites: A review. *Composites Science and Technology* **72**, 1459–1476 (2012).
4. Eda, G. & Chhowalla, M. Chemically Derived Graphene Oxide: Towards Large-Area Thin-Film Electronics and Optoelectronics. *Adv. Mater.* **22**, 2392–2415 (2010).
5. Eda, G. *et al.* Blue Photoluminescence from Chemically Derived Graphene Oxide. *Adv. Mater.* **22**, 505–509 (2010).
6. Luo, Z., Lu, Y., Somers, L. A. & Johnson, A. T. C. High Yield Preparation of Macroscopic Graphene Oxide Membranes. *J. Am. Chem. Soc.* **131**, 898–899 (2009).
7. Su, C.-Y. *et al.* Electrical and Spectroscopic Characterizations of Ultra-Large Reduced Graphene Oxide Monolayers. *Chemistry of Materials* **21**, 5674–5680 (2009).
8. Wilson, N. R. *et al.* Graphene Oxide: Structural Analysis and Application as a Highly Transparent Support for Electron Microscopy. *ACS Nano* **3**, 2547–2556 (2009).
9. Zhao, J., Pei, S., Ren, W., Gao, L. & Cheng, H.-M. Efficient Preparation of Large-Area Graphene Oxide Sheets for Transparent Conductive Films. *ACS Nano* **4**, 5245–5252 (2010).
10. Woltornist, S. J., Oyer, A. J., Carrillo, J.-M. Y., Dobrynin, A. V. & Adamson, D. H. Conductive Thin Films of Pristine Graphene by Solvent Interface Trapping. *ACS Nano* **7**, 7062–7066 (2013).
11. Zisman, W. A. Relation of the Equilibrium Contact Angle to Liquid and Solid Constitution. *Advances in Chemistry* 1–51 (1964).doi:10.1021/ba-1964-0043.ch001
12. Owens, D. K. & Wendt, R. C. Estimation of the surface free energy of polymers. *Journal of Applied Polymer Science* **13**, 1741–1747 (1969).
13. Fowkes, F. M. ATTRACTIVE FORCES AT INTERFACES. *Industrial & Engineering Chemistry* **56**, 40–52 (1964).
14. Wu, S. Interfacial and Surface Tensions of Polymers. *Journal of Macromolecular Science, Part C: Polymer Reviews* **10**, 1–73 (1974).
15. Schultz, J. & Nardin, M. Determination of the Surface Energy of Solids by the Two-Liquid-Phase Method. *Modern Approaches to Wettability* 73–100 (1992).doi:10.1007/978-1-4899-1176-6_4
16. Oss, C. J. van, Chaudhury, M. K. & Good, R. J. Monopolar surfaces. *Advances in Colloid*

and Interface Science **28**, 35–64 (1987).

17. Oss, C. J. V., Good, R. J. & Chaudhury, M. K. Additive and nonadditive surface tension components and the interpretation of contact angles. *Langmuir* **4**, 884–891 (1988).

18. Menzel, R., Bismarck, A. & Shaffer, M. S. P. Deconvolution of the structural and chemical surface properties of carbon nanotubes by inverse gas chromatography. *Carbon* **50**, 3416–3421 (2012).

19. Menzel, R., Lee, A., Bismarck, A. & Shaffer, M. S. P. Inverse Gas Chromatography of As-Received and Modified Carbon Nanotubes. *Langmuir* **25**, 8340–8348 (2009).

20. Gerencsér, F., Rieder, N., Varga, C., Hancsók, J. & Dallos, A. Surface Energy Heterogeneity Profiles of Carbon Nanotubes with a Copolymer-Modified Surface Using Surface Energy Mapping by Inverse Gas Chromatography. *Hungarian Journal of Industry and Chemistry* **45**, 61–66 (2017).

21. Zsirka, B. *et al.* Structural and energetical characterization of exfoliated kaolinite surfaces. *Applied Clay Science* **124-125**, 54–61 (2016).

22. Hadjittofis, E., Zhang, G. G. Z. & Heng, J. Y. Y. Influence of sample preparation on IGC measurements: the cases of silanised glass wool and packing structure. *RSC Advances* **7**, 12194–12200 (2017).

23. Israelachvili, J. N. & Adams, G. E. Direct measurement of long range forces between two mica surfaces in aqueous KNO3 solutions. *Nature* **262**, 774–776 (1976).

24. Israelachvili, J. *et al.* Recent advances in the surface forces apparatus (SFA) technique. *Reports on Progress in Physics* **73**, 036601 (2010).

25. Tabor, D. & Winterton, R. H. S. The Direct Measurement of Normal and Retarded van der Waals Forces. *Proceedings of the Royal Society A: Mathematical, Physical and Engineering Sciences* **312**, 435–450 (1969).

26. Leckband, D. E. *et al.* Force Probe Measurements of Antibody–Antigen Interactions. *Methods* **20**, 329–340 (2000).

27. Restagno, F., Crassous, J., Charlaix, É., Cottin-Bizonne, C. & Monchanin, M. A new surface forces apparatus for nanorheology. *Review of Scientific Instruments* **73**, 2292–2297 (2002).

28. SurForce LLC. at <https://surforcellc.com/>

29. Ashton, M., Paul, J., Sinnott, S. B. & Hennig, R. G. Topology-Scaling Identification of Layered Solids and Stable Exfoliated 2D Materials. *Physical Review Letters* **118**, (2017).

30. Novoselov, K. S. *et al.* Two-dimensional atomic crystals. *Proceedings of the National Academy of Sciences* **102**, 10451–10453 (2005).

31. Lee, C., Wei, X., Kysar, J. W. & Hone, J. Measurement of the Elastic Properties and Intrinsic Strength of Monolayer Graphene. *Science* **321**, 385–388 (2008).

32. Akinwande, D. *et al.* A review on mechanics and mechanical properties of 2D materials—Graphene and beyond. *Extreme Mechanics Letters* **13**, 42–77 (2017).

33. Chen, S. *et al.* Raman Measurements of Thermal Transport in Suspended Monolayer Graphene of Variable Sizes in Vacuum and Gaseous Environments. *ACS Nano* **5**, 321–328 (2010).

34. Pop, E., Varshney, V. & Roy, A. K. Thermal properties of graphene: Fundamentals and applications. *MRS Bulletin* **37**, 1273–1281 (2012).

35. Chen, J.-H., Jang, C., Xiao, S., Ishigami, M. & Fuhrer, M. S. Intrinsic and extrinsic performance limits of graphene devices on SiO2. *Nature Nanotechnology* **3**, 206–209 (2008).

36. Bonaccorso, F., Sun, Z., Hasan, T. & Ferrari, A. C. Graphene photonics and optoelectronics. *Nature Photonics* **4**, 611–622 (2010).

37. Dreyer, D. R., Park, S., Bielawski, C. W. & Ruoff, R. S. The chemistry of graphene oxide. *Chem. Soc. Rev.* **39**, 228–240 (2010).

38. He, H., Riedl, T., Lerf, A. & Klinowski, J. Solid-State NMR Studies of the Structure of

Graphite Oxide. *The Journal of Physical Chemistry* **100**, 19954–19958 (1996).

39. Brodie, B. C. On the Atomic Weight of Graphite. *Philosophical Transactions of the Royal Society of London Series I* **149**, 249–259 (1859).

40. Hummers, W. S. & Offeman, R. E. Preparation of Graphitic Oxide. *J. Am. Chem. Soc.* **80**, 1339–1339 (1958).

41. Joshi, R. *et al.* Precise and ultrafast molecular sieving through graphene oxide membranes. *Science* **343**, 752–754 (2014).

42. Su, Y. *et al.* Impermeable barrier films and protective coatings based on reduced graphene oxide. *Nature Communications* **5**, (2014).

43. Zheng, X. *et al.* Highly efficient and ultra-broadband graphene oxide ultrathin lenses with three-dimensional subwavelength focusing. *Nature Communications* **6**, (2015).

44. Lindsay, L. & Broido, D. A. Enhanced thermal conductivity and isotope effect in single-layer hexagonal boron nitride. *Physical Review B* **84**, (2011).

45. Cassabois, G., Valvin, P. & Gil, B. Hexagonal boron nitride is an indirect bandgap semiconductor. *Nature Photonics* **10**, 262–266 (2016).

46. Pakdel, A., Zhi, C., Bando, Y. & Golberg, D. Low-dimensional boron nitride nanomaterials. *Materials Today* **15**, 256–265 (2012).

47. Lin, Y. & Connell, J. W. Advances in 2D boron nitride nanostructures: nanosheets, nanoribbons, nanomeshes, and hybrids with graphene. *Nanoscale* **4**, 6908 (2012).

48. Watanabe, K., Taniguchi, T. & Kanda, H. Direct-bandgap properties and evidence for ultraviolet lasing of hexagonal boron nitride single crystal. *Nature Materials* **3**, 404–409 (2004).

49. Zhang, K., Feng, Y., Wang, F., Yang, Z. & Wang, J. Two dimensional hexagonal boron nitride (2D-hBN): synthesis, properties and applications. *Journal of Materials Chemistry C* **5**, 11992–12022 (2017).

50. Dickinson, R. G. & Pauling, L. THE CRYSTAL STRUCTURE OF MOLYBDENITE. *Journal of the American Chemical Society* **45**, 1466–1471 (1923).

51. Cherkashinin, G. *et al.* The stability of the SEI layer, surface composition and the oxidation state of transition metals at the electrolyte–cathode interface impacted by the electrochemical cycling: X-ray photoelectron spectroscopy investigation. *Physical Chemistry Chemical Physics* **14**, 12321 (2012).

52. Manzeli, S., Ovchinnikov, D., Pasquier, D., Yazyev, O. V. & Kis, A. 2D transition metal dichalcogenides. *Nature Reviews Materials* **2**, 17033 (2017).

53. Dai, J., Wang, G., Ma, L. & Wu, C. Study on the surface energies and dispersibility of graphene oxide and its derivatives. *Journal of Materials Science* **50**, 3895–3907 (2015).

54. Wang, S., Zhang, Y., Abidi, N. & Cabrales, L. Wettability and Surface Free Energy of Graphene Films. *Langmuir* **25**, 11078–11081 (2009).

55. Li, Z. *et al.* Effect of airborne contaminants on the wettability of supported graphene and graphite. *Nature Materials* **12**, 925–931 (2013).

56. Engers, C. D. van *et al.* Direct Measurement of the Surface Energy of Graphene. *Nano Letters* **17**, 3815–3821 (2017).

57. Wang, J. *et al.* Atomic intercalation to measure adhesion of graphene on graphite. *Nature Communications* **7**, 13263 (2016).

58. Li, P., You, Z. & Cui, T. Adhesion energy of few layer graphene characterized by atomic force microscope. *Sensors and Actuators A: Physical* **217**, 56–61 (2014).

59. Huang, Y. *et al.* Reliable Exfoliation of Large-Area High-Quality Flakes of Graphene and Other Two-Dimensional Materials. *ACS Nano* **9**, 10612–10620 (2015).

60. Hernandez, Y. *et al.* High-yield production of graphene by liquid-phase exfoliation of graphite. *Nature Nanotechnology* **3**, 563–568 (2008).

61. Nuvoli, D. *et al.* High concentration few-layer graphene sheets obtained by liquid phase exfoliation of graphite in ionic liquid. *J. Mater. Chem.* **21**, 3428–3431 (2011).

62. Fernández-Merino, M. J. *et al.* Investigating the influence of surfactants on the stabilization of aqueous reduced graphene oxide dispersions and the characteristics of their composite films. *Carbon* **50**, 3184–3194 (2012).
63. Lee, J. H. *et al.* One-Step Exfoliation Synthesis of Easily Soluble Graphite and Transparent Conducting Graphene Sheets. *Advanced Materials* **21**, 4383–4387 (2009).
64. Green, A. A. & Hersam, M. C. Emerging Methods for Producing Monodisperse Graphene Dispersions. *The Journal of Physical Chemistry Letters* **1**, 544–549 (2009).
65. Coleman, J. N. Liquid Exfoliation of Defect-Free Graphene. *Accounts of Chemical Research* **46**, 14–22 (2012).
66. Muñoz, R. & Gómez-Aleixandre, C. Review of CVD Synthesis of Graphene. *Chemical Vapor Deposition* **19**, 297–322 (2013).
67. Berger, C. *et al.* Electronic Confinement and Coherence in Patterned Epitaxial Graphene. *Science* **312**, 1191–1196 (2006).
68. Dikin, D. A. *et al.* Preparation and characterization of graphene oxide paper. *Nature* **448**, 457–460 (2007).
69. Tung, V. C., Allen, M. J., Yang, Y. & Kaner, R. B. High-throughput solution processing of large-scale graphene. *Nature Nanotechnology* **4**, 25–29 (2008).
70. Kumar, H. V., Woltornist, S. J. & Adamson, D. H. Fractionation and characterization of graphene oxide by oxidation extent through emulsion stabilization. *Carbon* **98**, 491–495 (2016).
71. Woltornist, S. J. *et al.* Preparation of conductive graphene/graphite infused fabrics using an interface trapping method. *Carbon* **81**, 38–42 (2015).
72. Woltornist, S. J., Carrillo, J.-M. Y., Xu, T. O., Dobrynin, A. V. & Adamson, D. H. Polymer/Pristine Graphene Based Composites: From Emulsions to Strong, Electrically Conducting Foams. *Macromolecules* **48**, 687–693 (2015).
73. Woltornist, S. J. *et al.* Controlled 3D Assembly of Graphene Sheets to Build Conductive, Chemically Selective and Shape-Responsive Materials. *Advanced Materials* **29**, 1604947 (2017).
74. Woltornist, S. J. & Adamson, D. H. Properties of Pristine Graphene Composites Arising from the Mechanism of Graphene-Stabilized Emulsion Formation. *Industrial & Engineering Chemistry Research* **55**, 6777–6782 (2016).
75. Eaton, P. & West, P. *Atomic Force Microscopy*. (Oxford University Press: 2010).
76. Giessibl, F. J. High-speed force sensor for force microscopy and profilometry utilizing a quartz tuning fork. *Applied Physics Letters* **73**, 3956–3958 (1998).
77. Butt, H.-J., Cappella, B. & Kappl, M. Force measurements with the atomic force microscope: Technique, interpretation and applications. *Surface Science Reports* **59**, 1–152 (2005).
78. Cappella, B. & Dietler, G. . Force-distance curves by atomic force microscopy. *Surface Science Reports* **34**, 1–104 (1999).
79. Israelachvili, J. N. *Intermolecular and Surface Forces*. (Academic Press: 1992).
80. Casimir, H. On the Attraction Between Two Perfectly Conducting Plates. *Proc. K. Ned. Akad. Wet.* **51**, 793 (1948).
81. Higgins, S. R., Eggleston, C. M., Knauss, K. G. & Boro, C. O. A hydrothermal atomic force microscope for imaging in aqueous solution up to 150 textdegreeC. *Review of Scientific Instruments* **69**, 2994 (1998).
82. Lea, A. S., Higgins, S. R., Knauss, K. G. & Rosso, K. M. A high-pressure atomic force microscope for imaging in supercritical carbon dioxide. *Review of Scientific Instruments* **82**, 043709 (2011).
83. Bracco, J. N., Gooijer, Y. & Higgins, S. R. Hydrothermal atomic force microscopy observations of barite step growth rates as a function of the aqueous barium-to-sulfate ratio. *Geochimica et Cosmochimica Acta* **183**, 1–13 (2016).

84. Schneider, C. A., Rasband, W. S. & Eliceiri, K. W. NIH Image to ImageJ: 25 years of image analysis. *Nature Methods* **9**, 671–675 (2012).

85. Necas, D. & Klapetek, P. Gwyddion: an open-source software for SPM data analysis. *Open Physics* **10**, 181–188 (2012).

86. Sader, J. E. *et al.* Spring constant calibration of atomic force microscope cantilevers of arbitrary shape. *Review of Scientific Instruments* **83**, 103705 (2012).

87. Dickinson, W. W., Kumar, H. V., Adamson, D. H. & Schniepp, H. C. High-throughput optical thickness and size characterization of 2D materials. *Nanoscale* **10**, 14441–14447 (2018).

88. Gonçalves, G. *et al.* Breakdown into nanoscale of graphene oxide: Confined hot spot atomic reduction and fragmentation. *Scientific Reports* **4**, 6735 (2014).

89. Treossi, E. *et al.* High-Contrast Visualization of Graphene Oxide on Dye-Sensitized Glass, Quartz, and Silicon by Fluorescence Quenching. *J. Am. Chem. Soc.* **131**, 15576–15577 (2009).

90. Liscio, A. *et al.* Evolution of the size and shape of 2D nanosheets during ultrasonic fragmentation. *2D Materials* **4**, 025017 (2017).

91. Li, H. *et al.* Rapid and Reliable Thickness Identification of Two-Dimensional Nanosheets Using Optical Microscopy. *ACS Nano* **7**, 10344–10353 (2013).

92. Kudin, K. N. *et al.* Raman Spectra of Graphite Oxide and Functionalized Graphene Sheets. *Nano Letters* **8**, 36–41 (2008).

93. Roddaro, S., Pingue, P., Piazza, V., Pellegrini, V. & Beltram, F. The Optical Visibility of Graphene: Interference Colors of Ultrathin Graphite on SiO 2. *Nano Letters* **7**, 2707–2710 (2007).

94. Blake, P. *et al.* Making graphene visible. *Applied Physics Letters* **91**, 063124 (2007).

95. Perrozzi, F. *et al.* Use of Optical Contrast To Estimate the Degree of Reduction of Graphene Oxide. *The Journal of Physical Chemistry C* **117**, 620–625 (2012).

96. Gorbachev, R. V. *et al.* Hunting for Monolayer Boron Nitride: Optical and Raman Signatures. *Small* **7**, 465–468 (2011).

97. Late, D. J., Liu, B., Matte, H., Rao, C. & Dravid, V. P. Rapid Characterization of Ultrathin Layers of Chalcogenides on SiO2/Si Substrates. *Advanced Functional Materials* **22**, 1894–1905 (2012).

98. Li, H. *et al.* Optical Identification of Single- and Few-Layer MoS2 Sheets. *Small* **8**, 682–686 (2012).

99. Jung, I. *et al.* Simple Approach for High-Contrast Optical Imaging and Characterization of Graphene-Based Sheets. *Nano Lett.* **7**, 3569–3575 (2007).

100. Dimiev, A. M. & Tour, J. M. Mechanism of Graphene Oxide Formation. *ACS Nano* **8**, 3060–3068 (2014).

101. Kumar, S. *et al.* Femtosecond carrier dynamics and saturable absorption in graphene suspensions. *Applied Physics Letters* **95**, 191911 (2009).

102. Loh, K. P., Bao, Q., Eda, G. & Chhowalla, M. Graphene oxide as a chemically tunable platform for optical applications. *Nature Chemistry* **2**, 1015–1024 (2010).

103. Dagastine, R. R., Prieve, D. C. & White, L. R. Forces between a rigid probe particle and a liquid interface. *Journal of Colloid and Interface Science* **269**, 84–96 (2004).

104. Dickinson, L. R. Characterization of Interfacial Interactions by Functionalized AFM Probes. (2016).

105. Pei, S. & Cheng, H.-M. The reduction of graphene oxide. *Carbon* **50**, 3210–3228 (2012).

106. Yang, D. *et al.* Chemical analysis of graphene oxide films after heat and chemical treatments by X-ray photoelectron and Micro-Raman spectroscopy. *Carbon* **47**, 145–152 (2009).

107. Stankovich, S. *et al.* Synthesis of graphene-based nanosheets via chemical reduction of exfoliated graphite oxide. *Carbon* **45**, 1558–1565 (2007).

108. Gómez-Navarro, C. *et al.* Electronic Transport Properties of Individual Chemically Reduced Graphene Oxide Sheets. *Nano Letters* **7**, 3499–3503 (2007).

109. Mattevi, C. *et al.* Evolution of Electrical, Chemical, and Structural Properties of Transparent and Conducting Chemically Derived Graphene Thin Films. *Advanced Functional Materials* **19**, 2577–2583 (2009).

110. Shin, H.-J. *et al.* Efficient Reduction of Graphite Oxide by Sodium Borohydride and Its Effect on Electrical Conductance. *Advanced Functional Materials* **19**, 1987–1992 (2009).

111. Schniepp, H. C. *et al.* Functionalized Single Graphene Sheets Derived from Splitting Graphite Oxide. *The Journal of Physical Chemistry B* **110**, 8535–8539 (2006).

112. McAllister, M. J. *et al.* Single Sheet Functionalized Graphene by Oxidation and Thermal Expansion of Graphite. *Chemistry of Materials* **19**, 4396–4404 (2007).

113. Becerril, H. A. *et al.* Evaluation of Solution-Processed Reduced Graphene Oxide Films as Transparent Conductors. *ACS Nano* **2**, 463–470 (2008).

114. Cote, L. J., Cruz-Silva, R. & Huang, J. Flash Reduction and Patterning of Graphite Oxide and Its Polymer Composite. *Journal of the American Chemical Society* **131**, 11027–11032 (2009).

115. Agbalaka, C. C., Dandekar, A. Y., Patil, S. L., Khataniar, S. & Hemsath, J. The Effect Of Wettability On Oil Recovery: A Review. *SPE Asia Pacific Oil and Gas Conference and Exhibition* (2008).doi:10.2118/114496-MS

116. Hyne, N. J. *Nontechnical Guide to Petroleum Geology, Exploration, Drilling, and Production*. (PennWell Books: 2001).

117. Sharma, M. M. & Filoco, P. R. Effect of Brine Salinity and Crude-Oil Properties on Oil Recovery and Residual Saturations. *SPE Journal* **5**, 293–300 (2000).

118. Dake, L. *Fundamentals of reservoir engineering*. (1978).

119. Huang, J. S. & Varadaraj, R. Colloid and interface science in the oil industry. *Current Opinion in Colloid & Interface Science* **1**, 535–539 (1996).

120. Lager, A., Webb, K. & Black, C. Impact of brine chemistry on oil recovery. *IOR 2007-14th European Symposium on Improved Oil Recovery* (2007).

121. Cuiec, L. E. Restoration of the Natural State of Core Samples. *Fall Meeting of the Society of Petroleum Engineers of AIME* (1975).doi:10.2118/5634-MS

122. Skrettingland, K., Holt, T., Tweheyo, M. T. & Skjevrak, I. Snorre Low-Salinity-Water Injection–Coreflooding Experiments and Single-Well Field Pilot. *SPE Reservoir Evaluation & Engineering* **14**, 182–192 (2011).

123. Suijkerbuijk, B. *et al.* The development of a workflow to improve predictive capability of low salinity response. *IPTC 2013: International Petroleum Technology Conference* (2013).

124. Tissot, B. & Welte, D. *Petroleum formation and occurrence*. (Springer-Verlag, New York, NY: 1984).

125. Zhang, Y. & Morrow, N. R. Comparison of Secondary and Tertiary Recovery With Change in Injection Brine Composition for Crude-Oil/Sandstone Combinations. *SPE/DOE Symposium on Improved Oil Recovery* (2006).doi:10.2118/99757-MS

126. Zhu, Y., Weng, H., Chen, Z. & Chen, Q. Compositional modification of crude oil during oil recovery. *Journal of Petroleum Science and Engineering* **38**, 1–11 (2003).

127. Austad, T., Rezaeidoust, A. & Puntervold, T. Chemical Mechanism of Low Salinity Water Flooding in Sandstone Reservoirs. *SPE Improved Oil Recovery Symposium* (2010).doi:10.2118/129767-MS

128. Firoozabadi, A., Ramey Jr, H. J. & others Surface tension of water-hydrocarbon systems at reservoir conditions. *Journal of Canadian Petroleum Technology* **27**, (1988).

129. Strand, S., Høgnesen, E. J. & Austad, T. Wettability alteration of carbonates—Effects of potential determining ions (Ca2mathplus and SO42-) and temperature. *Colloids and Surfaces A: Physicochemical and Engineering Aspects* **275**, 1–10 (2006).

130. Webb, K., Lager, A. & Black, C. Comparison of high/low salinity water/oil relative

permeability. *International symposium of the society of core analysts, Abu Dhabi, UAE* **29**, (2008).

131. Druetta, P., Tesi, P., Persis, C. D. & Picchioni, F. Methods in Oil Recovery Processes and Reservoir Simulation. *Advances in Chemical Engineering and Science* **06**, 39–435 (2016).

132. McCarthy, K. *et al.* Basic petroleum geochemistry for source rock evaluation. *Oilfield Review* **23**, 32–43 (2011).

133. Al-Hajeri, M. M. *et al.* Basin and petroleum system modeling. *Oilfield Review* **21**, 14–29 (2009).

134. Aksulu, H., Håmsø, D., Strand, S., Puntervold, T. & Austad, T. Evaluation of Low-Salinity Enhanced Oil Recovery Effects in Sandstone: Effects of the Temperature and pH Gradient. *Energy & Fuels* **26**, 3497–3503 (2012).

135. Anderson, W. Wettability Literature Survey- Part 2: Wettability Measurement. *Journal of Petroleum Technology* **38**, 1246–1262 (1986).

136. Austad, T., Shariatpanahi, S. F., Strand, S., Black, C. J. J. & Webb, K. J. Conditions for a Low-Salinity Enhanced Oil Recovery (EOR) Effect in Carbonate Oil Reservoirs. *Energy & Fuels* **26**, 569–575 (2012).

137. Buckley, J. S. Effective wettability of minerals exposed to crude oil. *Current Opinion in Colloid & Interface Science* **6**, 191–196 (2001).

138. Hadia, N. J., Hansen, T., Tweheyo, M. T. & Torsæter, O. Influence of Crude Oil Components on Recovery by High and Low Salinity Waterflooding. *Energy & Fuels* **26**, 4328–4335 (2012).

139. Kumar, M., Fogden, A., Morrow, N. R., Buckley, J. S. & others Mechanisms of improved oil recovery from sandstone by low salinity flooding. *Petrophysics* **52**, 428–436 (2011).

140. Lager, A., Webb, K., Black, C., Singleton, M. & Sorbie, K. Low salinity oil recovery. *An Experimental Investigation, presented at the Society of Core Analysts. SCA, Trondheim, Norway* (2006).

141. Tang, G.-Q. & Morrow, N. R. Influence of brine composition and fines migration on crude oil/brine/rock interactions and oil recovery. *Journal of Petroleum Science and Engineering* **24**, 99–111 (1999).

142. Yildiz, H. O. & Morrow, N. R. Effect of brine composition on recovery of Moutray crude oil by waterflooding. *Journal of Petroleum Science and Engineering* **14**, 159–168 (1996).

143. Zhou, X., Morrow, N. R. & Ma, S. Interrelationship of Wettability, Initial Water Saturation, Aging Time, and Oil Recovery by Spontaneous Imbibition and Waterflooding. *SPE Journal* **5**, 199–207 (2000).

144. Maini, B. B., Okazawa, T. & others Effects of temperature on heavy oil-water relative permeability of sand. *Journal of Canadian Petroleum Technology* **26**, (1987).

145. Naylor, P., Mogford, D. & Smith, R. Development of In-Situ Measurements to Determine Reservoir Condition Critical Gas Saturations During Depressurization. *PETROPHYSICS-HOUSTON-* **42**, 323–333 (2001).

146. Soraya, B., Malick, C., Philippe, C., Bertin, H. J. & Hamon, G. Oil Recovery by Low-Salinity Brine Injection: Laboratory Results on Outcrop and Reservoir Cores. *SPE Annual Technical Conference and Exhibition* (2009).doi:10.2118/124277-MS

147. Strand, S., Puntervold, T. & Austad, T. Effect of Temperature on Enhanced Oil Recovery from Mixed-Wet Chalk Cores by Spontaneous Imbibition and Forced Displacement Using Seawater. *Energy & Fuels* **22**, 3222–3225 (2008).

148. Tang, G. Q. & Morrow, N. R. Salinity, Temperature, Oil Composition, and Oil Recovery by Waterflooding. *SPE Reservoir Engineering* **12**, 269–276 (1997).

149. Webb, K. J., Black, C. J. J., Tjetland, G. & others A laboratory study investigating methods for improving oil recovery in carbonates. *International Petroleum Technology Conference* (2005).

150. Weinbrandt, R., Ramey Jr, H., Casse, F. & others The effect of temperature on relative

and absolute permeability of sandstones. *Society of Petroleum Engineers Journal* **15**, 376–384 (1975).

151. Dickinson, L. R., Suijkerbuijk, B. M. J. M., Berg, S., Marcelis, F. H. M. & Schniepp, H. C. Atomic Force Spectroscopy Using Colloidal Tips Functionalized with Dried Crude Oil: A Versatile Tool to Investigate Oil–Mineral Interactions. *Energy & Fuels* **30**, 9193–9202 (2016).

152. Aldushin, K., Jordan, G., Rammensee, W., Schmahl, W. W. & Becker, H.-W. Apophyllite (001) surface alteration in aqueous solutions studied by HAFM. *Geochimica et Cosmochimica Acta* **68**, 217–226 (2004).

153. Buckley, J. S. *et al.* Asphaltene precipitation and solvent properties of crude oils. *Petroleum Science and Technology* **16**, 251–285 (1998).

154. Buckley, J. S. & Liu, Y. Some mechanisms of crude oil/brine/solid interactions. *Journal of Petroleum Science and Engineering* **20**, 155–160 (1998).

155. Buckley, J. S. & Wang, J. Crude oil and asphaltene characterization for prediction of wetting alteration. *Journal of Petroleum Science and Engineering* **33**, 195–202 (2002).

156. Cleveland, J. P., Manne, S., Bocek, D. & Hansma, P. K. A nondestructive method for determining the spring constant of cantilevers for scanning force microscopy. *Review of Scientific Instruments* **64**, 403–405 (1993).

157. Au, P.-I., Siow, S.-Y., Avadiar, L., Lee, E.-M. & Leong, Y.-K. Muscovite mica and koalin slurries: Yield stress–volume fraction and deflocculation point zeta potential comparison. *Powder Technology* **262**, 124–130 (2014).

158. Nishimura, S., Tateyama, H., Tsunematsu, K. & Jinnai, K. Zeta potential measurement of muscovite mica basal plane-aqueous solution interface by means of plane interface technique. *Journal of Colloid and Interface Science* **152**, 359–367 (1992).

159. Buckley, J. S., Takamura, K. & Morrow, N. R. Influence of Electrical Surface Charges on the Wetting Properties of Crude Oils. *SPE Reservoir Engineering* **4**, 332–340 (1989).

160. Buckley, J. S. Chemistry of the crude oil/brine interface. *Proc. 3 rd International Symposium on Evaluation of Reservoir Wettability and Its Effect on Oil Recovery* 33–38 (1994).

161. Buckley, J. S. & Lord, D. L. Wettability and morphology of mica surfaces after exposure to crude oil. *Journal of Petroleum Science and Engineering* **39**, 261–273 (2003).

162. Drummond, C. & Israelachvili, J. Fundamental studies of crude oil–surface water interactions and its relationship to reservoir wettability. *Journal of Petroleum Science and Engineering* **45**, 61–81 (2004).

163. Casey, W. H. & Sposito, G. On the temperature dependence of mineral dissolution rates. *Geochimica et Cosmochimica Acta* **56**, 3825–3830 (1992).